Royal Military Academy
Polytechnic Faculty
Brussels, Belgium

Université Libre de Bruxelles
Ecole Polytechnique de Bruxelles
Brussels, Belgium

Optimum reference signal reconstruction for DVB-T passive radars

Osama Mahfoudia

Supervisors: Prof. Xavier Neyt & Prof. François Horlin

Thesis submitted in fulfillment of the requirement for the degree of
Doctor in Engineering Sciences (RMA)
Doctor in Engineering Sciences and Technology (ULB)

September 2017

Abstract

Passive coherent location (PCL) radars employ illuminators of opportunity to detect and track targets. This silent operating mode provides many advantages such as low cost and interception immunity. Many radiation sources have been exploited as illumination sources such as broadcasting and telecommunication transmitters. The classical architecture of the bistatic PCL radars involves two receiving channels: a reference channel and a surveillance channel. The reference channel captures the direct-path signal from the transmitter, and the surveillance signal collects the possible target echoes.

The two major challenges for the PCL radars are the reference signal noise and the surveillance signal static clutter. A noisy reference signal degrades the detection probability by increasing the noise-floor level of the detection filter output. And the static clutter presence in the surveillance signal reduces the detector dynamic range and buries low magnitude echoes.

In this thesis, we consider a PCL radar based on the digital video broadcasting-terrestrial (DVB-T) signals, and we propose a set of improved methods to deal with the reference signal noise and the static clutter in the surveillance signal. The DVB-T signals constitute an excellent candidate as an illumination source for PCL radars; they are characterized by a wide bandwidth and a high radiated power. In addition, they provide the possibility of reconstructing the reference signal to enhance its quality, and they allow a straightforward static clutter suppression in the frequency domain. This thesis proposes an optimum method for the reference signal reconstruction and an improved method for the static clutter suppression.

The optimum reference signal reconstruction minimizes the mean square error between the reconstructed signal and the exact one. And the improved static clutter suppression method exploits the possibility of estimating the propagation channel. These two methods extend the feasibility of a single receiver PCL radar, where the reference signal is extracted from the direct-path signal present in the surveillance signal.

Acknowledgements

First, I would like to express my gratitude to my supervisors, Professor Xavier Neyt and Professor François Horlin for their guidance and motivation during the time of this thesis.

My thanks also go to the Algerian Army Command for allowing and supporting this work, and for the confidence they have placed in me.

I cannot forget to thank all the CISS department members for their hospitality and cooperation.

Finally, I would like to thank my family and my friends for their support during these four years.

Publications

The following publications were produced during this work:

- O. Mahfoudia and X. Neyt. A DVB-T based passive radar using one USRP board. In URSI Benelux Forum, (Louvain-la-Neuve, Belgium), 2014.
- O. Mahfoudia and X. Neyt. Analysis of Direct Signal Recovery Scheme for DVB-T Based Passive Radars. In 36th WIC Symposium on Information Theory in the Benelux, (Brussels, Belgium), 2015.
- O. Mahfoudia and X. Neyt. Strong direct-path interference removal for DVB-T based passive radars. In URSI Benelux Forum, (Enschede, Netherlands), 2015.
- O. Mahfoudia, F. Horlin, and X. Neyt. Target detection for DVB-T based passive radars using pilot subcarrier signal. In 37th WIC Symposium on Information Theory in the Benelux, (Louvain-la-Neuve, Belgium), 2016.
- O. Mahfoudia, F. Horlin, and X. Neyt. An Improved Channel Estimation Scheme for DVB-T Passive Radars. In URSI Benelux Forum, (Brussels, Belgium), 2017.
- O. Mahfoudia, F. Horlin, and X. Neyt. Optimum reference signal reconstruction for DVB-T based passive radars. In IEEE Radar Conference (RadarConf), (Seatle, WA, USA), 2017.
- E. Cristofani, O. Mahfoudia, M. Becquaert, X. Neyt, F. Horlin, N. Deligiannis, J. Stiens, and M. Vandewal. Compressive Sensing and DVB-T-Based Passive Coherent Location. In URSI Benelux Forum, (Brussels, Belgium), 2017.
- O. Mahfoudia, F. Horlin, and X. Neyt. On the static clutter suppression for DVB-T based passive radars. In 32nd URSI General Assembly and Scientific Symposium, (Montreal, Canada), 2017.
- O. Mahfoudia, F. Horlin, and X. Neyt. On the feasibility of DVB-T based passive radar with a single receiver channel. In International Conference on Radar Systems (Radar 2017), (Belfast, UK), 2017.

Contents

List of Figures

List of Tables

Abbreviations

ACI Adjacent Channel Interference
ADC Analog-to-Digital Converter
ADS-B Automatic Dependent Surveillance-Broadcast
ADSL Asymmetric Digital Subscriber Line
AM Amplitude Modulation
BPSK Binary Phase Shift Keying
BRU Brussels Zaventem airport
CC Cross-Correlation
CDF Cumulative Distribution Function
CFO Carrier Frequency Offset
CIR Channel Impulse Response
CNR Clutter-to-Noise Ratio
CP Cyclic Prefix
CPI Coherent Processing Interval
CW Continuous Wave
DAB Digital Audio Broadcasting
DFT Discrete Fourier Transform
DNR Direct-path-to-Noise Ratio
DP Direct-Path
DVB-C Digital Video Broadcasting-Cable
DVB-T Digital Video Broadcasting-Terrestrial
ECA Extensive Cancellation Algorithm
ECA-B Extensive Cancellation Algorithm by Batches
ECA-C Extensive Cancellation Algorithm by Carriers

FFT	Fast Fourier Transform
FIR	Finite Impulse Response
FM	Frequency Modulation
GI	Guard Interval
GNSS	Global Navigation Satellite System
GPS	Global Positioning System
GSM	Global System for Mobile communication
IDFT	Inverse Discrete Fourier Transform
IO	Illuminator of Opportunity
ISI	Inter-Symbol Interference
LMS	Least Mean Squares
LOS	Line-Of-Sight
LS	Least Squares
MC	Monte-Carlo
MF	Matched Filter
ML	Maximum Likelihood
MMSE	Minimum Mean Square Error
MSE	Mean Square Error
NMSE	Normalized Mean Square Error
OFDM	Orthogonal Frequency-Division Multiplexing
PAPR	Peak-to-Average Power Ratio
PCL	Passive Coherent Location
PDF	Probability Density Function
PPM	Pulse Position Modulation
PRBS	Pseudo Random Binary Sequence
PSK	Phase Shift Keying
QAM	Quadrature Amplitude Modulation
QPSK	Quadrature Phase-Shift Keying
RCS	Radar Cross-Section
RDD	Range-Doppler Diagram
RLS	Recursive Least Square
SCS	Static Clutter Suppression

SDR	Software Defined Radio
SER	Symbol Error Rate
SFN	Single Frequency Networks
SNR	Signal-to-Noise Ratio
SVD	Singular-Value Decomposition
TPS	Transmission Parameter Signaling
UHF	Ultra High Frequency
USRP	Universal Software Radio Peripheral
VHF	Very High Frequency
ZP	Zero Padding

Symbols

α_m	Gain of the m^{th} target echo
β	Bistatic angle
Γ	Frequency-domain correlation for synchronization
γ	Time-domain correlation for synchronization
ΔF	Subcarrier spacing
δ	Angle of the target velocity vector
ζ	Detection threshold
η	Spectral efficiency
θ_R	Receiver look angle
θ_T	Transmitter look angle
θ	Fine time delay
κ	Time delay
κ_l	Delay of the l^{th} multipath component
κ_m	Delay of the m^{th} target echo
λ	Signal wavelength
μ_0	Mean of $\bar{T}$ under H_0
μ_1	Mean of $\bar{T}$ under H_1
ν	Frequency shift
ξ	Gain of the DP in the reference signal
σ_b	Target bistatic radar cross-section
σ_0^2	Variance of $\bar{T}$ under H_0
σ_1^2	Variance of $\bar{T}$ under H_1
σ_d^2	Variance of the data signal
σ_p^2	Variance of the pilot signal

σ_s^2	Variance of the transmitted signal
σ_v^2	Variance of the reference signal noise
σ_w^2	Variance of the surveillance signal noise
υ	Magnitude of the target velocity vector
ϕ	Carrier frequency offset
Ψ_{AF}	Ambiguity function
Ψ_{CC}	Cross-correlation result
Ω_{CP}	Continual subcarrier indices
Ω_{P}	Pilot subcarrier indices
A_R	Radial component of target acceleration
B	Receiver effective bandwidth
$\mathbf{c}$	Coded symbols $(K \times 1)$
$\mathbf{c}_d$	Coded data symbols $(K_d \times 1)$
$\mathbf{c}_p$	Coded pilot symbols $(K_p \times 1)$
$\tilde{\mathbf{c}}$	Detected coded symbols $(K \times 1)$
$\tilde{\mathbf{c}}_d$	Detected coded data symbols $(K_d \times 1)$
$\hat{\mathbf{c}}$	Optimally filtered symbols $(K \times 1)$
c_k	Coded symbol of the k^{th} subcarrier
D	Baseline
$d(n)$	Pilot signal samples
$\tilde{d}(n)$	Reconstructed data signal
E_b/N_0	Energy per bit to noise power spectral density ratio
f_B	Bistatic Doppler shift
$f_d(m)$	Doppler shift of the m^{th} target echo
f_k	Frequency of the k^{th} subcarrier
f_T	Carrier frequency
G_p	Coherent processing gain
G_R	Receiver antenna gain
G_T	Transmitter antenna gain
g_d	Optimum filter weight for data symbols
g_p	Optimum filter weight for pilot symbols

$\mathbf{H}$	Frequency-domain Propagation channel
$\hat{\mathbf{H}}$	Estimate of the frequency-domain Propagation channel
H_0	Null hypothesis
H_1	Alternative hypothesis
$\hat{\mathbf{H}}_{\mathbf{p},\mathbf{LS}}$	LS estimate of $\mathbf{H}$ at pilot subcarriers
$\hat{\mathbf{H}}_{\mathbf{p},\mathbf{MMSE}}$	MMSE estimate of $\mathbf{H}$ at pilot subcarriers
h_l	Gain of the l^{th} multipath component
i	DVB-T symbol index
K	Subcarrier number
K_d	Number of data subcarriers
K_p	Number of pilot subcarriers
K_{TPS}	Number of TPS subcarriers
k	Subcarrier index
k_B	Boltzmann's constant
L	Number of multipath components
L_s	System losses
M	Number of the moving targets
N	Number of samples in the CPI
N_{FFT}	FFT-block size
N_G	Number of time samples in the guard interval
N_U	Number of time samples in the useful part
$\mathrm{P_D}$	Detection probability
$\mathrm{P_e}$	Symbol error rate
$\mathrm{P_{FA}}$	False-alarm probability
P_T	Transmitted power
$p(n)$	Pilot signal samples
q	Semimajor of the isorange ellipsoid
$\mathbf{R}_{\mathbf{H_p}}$	Correlation matrix of $\mathbf{H_p}$
R_b	Bistatic range
R_R	Target-receiver distance
R_T	Transmitter-target distance
$\mathrm{R_x}$	Receiver location

$s(n)$	Transmitted signal samples
$\mathrm{SNR_r}$	reference signal SNR
$\mathrm{SNR_s(m)}$	SNR of the m^{th} target echo
$\hat{s}(n)$	Reconstructed signal
T	Test statistic
$\bar{T}$	Averaged test statistic
T_n	Receiver noise temperature
T_{CPI}	Length of the coherent processing interval
T_G	Guard interval duration
T_{max}	Maximum CPI length
T_s	Duration of one DVB-T symbol
T_U	Useful part duration of one DVB-T symbol
$\mathrm{T_x}$	Transmitter location
$v(n)$	Reference signal noise (time domain)
$\mathbf{V}$	FFT of $v(n)$
$w(n)$	Surveillance signal noise (time domain)
$\mathbf{W}$	FFT of $w(n)$
$\tilde{\mathbf{X}}$	Frequency-domain symbols of the synchronized signal
$\check{\mathbf{X}}$	Equalized symbols
$\mathbf{X}_{\mathrm{filtered}}$	Frequency-domain filtered symbols
$\tilde{\mathbf{X}}_{\mathbf{p}}$	Pilot symbols of $\tilde{\mathbf{X}}$
$\mathbf{x}_{\mathrm{r}}$	Reference signal array ($N \times 1$)
$\mathbf{x}_{\mathrm{s}}$	Surveillance signal array ($N \times 1$)
$x_{filtered}(n)$	Time-domain filtered signal
$x_r(n)$	Reference signal samples
$x_s(n)$	Surveillance signal samples

Chapter 1

General introduction

1.1 Overview

Radar is an acronym of Radio Detection and Ranging; it employs radio waves to determine the target characteristics such as position, speed, and acceleration [2]. Active radars transmit radio waves, and receive the echoes reflected by the objects. In contrast, passive coherent location (PCL) radars exploit the radiations of other sources to detect targets; these sources are called illuminators of opportunity [1, 3].

The illuminators of opportunity can be another radar or a commercial broadcasting source. Telecommunication and broadcasting signals have been widely employed as illumination sources such as frequency modulation (FM) radio [4–6], global system for mobile communications (GSM) [7, 8], digital audio broadcasting (DAB) [9, 10], and digital video broadcasting-terrestrial (DVB-T) [11, 12]. The choice of the illumination sources is related to many parameters such as the radiated power, the signal bandwidth, and the signal ambiguity function [1, 3, 13].

PCL radars can be bistatic or multistatic. The general architecture of the bistatic PCL radars includes two reception channels: a reference channel and a surveillance channel [12]. The antenna of the reference channel is directed towards the illuminator of opportunity location to acquire the direct-path signal. And the surveillance channel antenna is steered to the surveillance area to receive the target echoes. The detection is typically performed by cross-correlating the reference signal and the surveillance signal accounting for different time-delay and frequency-shift values [12]. This approach is an imitation of the matched filter detection, with the exception that the matched filter employs the exact signal waveform and not its noisy copy (the reference signal) [14].

The use of illuminators of opportunity offers important advantages for PCL radars. The absence of the transmitter part significantly reduces the system cost, and leads to a silent operating mode which gives an interception immunity for the passive systems [1, 15]. In addition, the most common illuminators of opportunity (such as FM and TV broadcasters) present a downward-looking radiation pattern, which enables the detection of low-flying targets (the scenario considered in this thesis) [16, 17]. Further, the exploited VHF/UHF signals are less sensitive to the weather conditions [15, 16].

1.2 Motivations

One of the major issues for PCL radars is the reference signal quality; it impacts the expected detection performance [14, 18–20]. In fact, a reference signal with low quality reduces the detection probability compared to the matched filter case [14]. Another issue is the presence of the static clutter in the surveillance signal. The static clutter results from reflections by the static scatterers in the surveillance area, which may mask the target echoes. Therefore, a static clutter suppression stage is required to enable the target detection; many methods have been employed for this purpose [21–23]. These suppression methods require a reference signal, which implies the degradation of their performance for low quality reference signals.

The DVB-T signals represent an attractive illumination source due to their wide bandwidth, high radiated power, and thumbtack ambiguity function [24, 25]. In addition, the DVB-T based PCL radars can enhance the signal-to-noise ratio of the received reference signal by demodulating it and reconstructing the resulting symbols [26, 27]. In this work, we consider a bistatic PCL radar based on the DVB-T illumination.

The assessment of the reference signal reconstruction strategy, and the evaluation of the resulting improvement related to the detection probability and to the static clutter suppression can be of a great interest for DVB-T based PCL system designers. In addition, exploiting the DVB-T signal structure can further simplify the PCL system architecture and offers efficient methods for the reference signal reconstruction and the static clutter suppression.

1.3 Objectives and contributions

1.3.1 Objectives

The aim of this work is to study the impact of the reference signal quality on the detection probability and on the static clutter suppression efficiency in the DVB-T based PCL radars, and to investigate the possibilities of improving the system performances and reducing its cost by exploiting the DVB-T signal structure. In order to do so, we first consider a noisy reference signal and we evaluate the resulting impact on the detection probability and the static clutter suppression efficiency. Next, we propose methods to enhance the reference signal quality and we assess the related improvement for the PCL system performances. Then, we exploit the DVB-T structure to propose an efficient method for static clutter suppression, and we investigate the feasibility of a single receiver configuration PCL system.

1.3.2 Original contributions

The main original contributions of this work are listed below.

- An analytic modeling of the reference signal reconstruction for the DVB-T based PCL radars.
- Pilot subcarrier based detection and its feasibility.
- An optimum reference signal reconstruction method.
- An assessment of the reference signal quality impact on the efficiency of the static clutter suppression methods.
- Improving the static clutter suppression in the frequency domain.
- An investigation of the feasibility of a single receiver PCL radar employing DVB-T signals.

1.4 Thesis outline

This thesis is organized into seven chapters. In chapter 2, we provide generalities about bistatic PCL radars. Chapter 3 presents the DVB-T signals and their suitability for PCL radar applications, and it introduces the signal synchronization and the channel estimation methods. In chapter 4, we assess the impact of the reference signal noise on the detection performances, we show the improvement due to the conventional signal reconstruction and due to the use of the pilot signal, and we propose an optimum reconstruction method. Chapter 5 addresses the static clutter suppression methods and their efficiency with a noisy reference signal. In chapter 6, we verify the feasibility of a single receiver PCL radar and we present the obtained real-data results. Finally, Chapter 7 presents the conclusions related to the full work, and provides the future works.

Chapter 2

Bistatic passive coherent location radars

2.1 Introduction

Passive coherent location (PCL) radars circumvent the need of signal transmission for operating. This class of radars exploits signals from illuminators of opportunity (IO) which can be another radar or commercial transmitters [28]. A special interest has been accorded to telecommunication and broadcasting signals as IOs such as frequency modulation (FM) radio [4–6], global system for mobile communications (GSM) [7, 8], digital audio broadcasting (DAB) [9, 10], and digital video broadcasting-terrestrial (DVB-T) [11, 12]. Employing IOs exempts the passive radars from transmission, which reduces their cost and enables an easy deployment. In addition, operating in a silent mode immunizes the passive systems against interception and hostile actions [1, 3]. The PCL radars can be bistatic or multistatic; bistatic PCL radars employ one transmitter-receiver pair, and multistatic PCL radars employ a cluster of transmitter-receiver pairs. In this chapter, we provide generalities about the bistatic PCL radars.

Section 2.2 introduces the bistatic radars and provides their advantages an drawbacks. Then, it presents the bistatic radar geometry and the parameters defining the target location. Next, it assesses the range equation for bistatic radars, and it defines the radar operating regions. After that, it defines the bistatic radar Doppler and it evaluates the impact of the target parameters (position and velocity) on the resulting Doppler shift.

Section 2.3 presents generalities about bistatic PCL radars. It introduces the model of the received signals, and it defines the target detection strategy. Afterwards, it presents an overview of the most common illuminators of opportunity and their characteristics.

2.2 Bistatic radars

This section provides generalities about the bistatic radar systems such as their configuration, their geometry, the radar range equation, and the radar Doppler characteristics.

2.2.1 Bistatic radar systems

Figure 2.1 presents the general configuration of bistatic radars. Bistatic radars are defined as radars that employ antennas at different locations for transmission and reception [28–31]. Other definitions precise that the transmitter-receiver distance should be significant and comparable to the target distance [32, 33].

Bistatic radars can employ either a dedicated transmitter or a transmitter of opportunity. The dedicated transmitter is designed for the bistatic detection; in this case, the transmitted signal is fully known at the receiver. The transmitter of opportunity is designed for other purposes such as telecommunications, broadcasting, or monostatic radars, then employed for the bistatic detection. The bistatic radar is called a hitchhiker if the employed transmitter of opportunity is a monostatic radar. For commercial transmitters of opportunity such as telecommunications and broadcasting the bistatic radar is often called a passive coherent location radar (PCL) [30].

Bistatic radars offer many advantages. The receivers are passive and thus undetectable, which makes them less threatened by physical attacks or jamming in military applications. They have counter-stealth capabilities since the efforts made to reduce the monostatic radar cross-section (RCS) will in general not reduce the bistatic RCS. The major drawback of the bistatic radars is the need of a perfect transmitter-receiver synchronization in time, frequency, phase, and other operating parameters. Further, the detection performance depends on the target position in a very complex manner [34, 35].

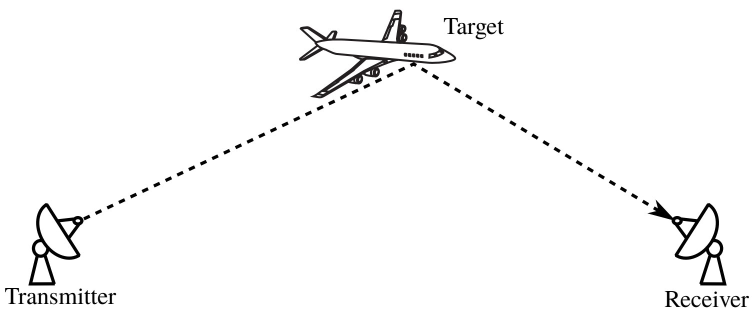

FIGURE 2.1: Bistatic radar configuration.

2.2.2 Bistatic radar geometry

Figure 2.2 presents the geometry of a bistatic radar operating in the plane transmitter-target-receiver [28, 36]. The bistatic triangle is formed by the transmitter (T_x), the target (Tgt), and the receiver (R_x). The plane containing the bistatic triangle is called the bistatic plane. The transmitter-receiver distance D is called the baseline. The angle β between the transmitter and the receiver with the target as a vertex is called the bistatic angle, which is given by

$$\beta = \theta_T - \theta_R, \tag{2.1}$$

where θ_T is the transmitter look angle and θ_R is the receiver look angle. The target velocity vector has an aspect angle δ referenced to the bisector of the bistatic angle.

In bistatic radars, the measured target range is the bistatic range. The bistatic range is the sum, $R_T + R_R$ where R_T is the transmitter-target distance and R_R is the target-receiver distance. In figure 2.3, we present a cut of the isorange ellipsoid, that corresponds to the bistatic plane (transmitter-target-receiver plane). It shows that two targets at different locations can result the same bistatic range if they are on the same bistatic ellipsoid. This ellipsoid has the transmitter and the receiver as focal points and a semimajor q with

$$R_T + R_R = 2q. \tag{2.2}$$

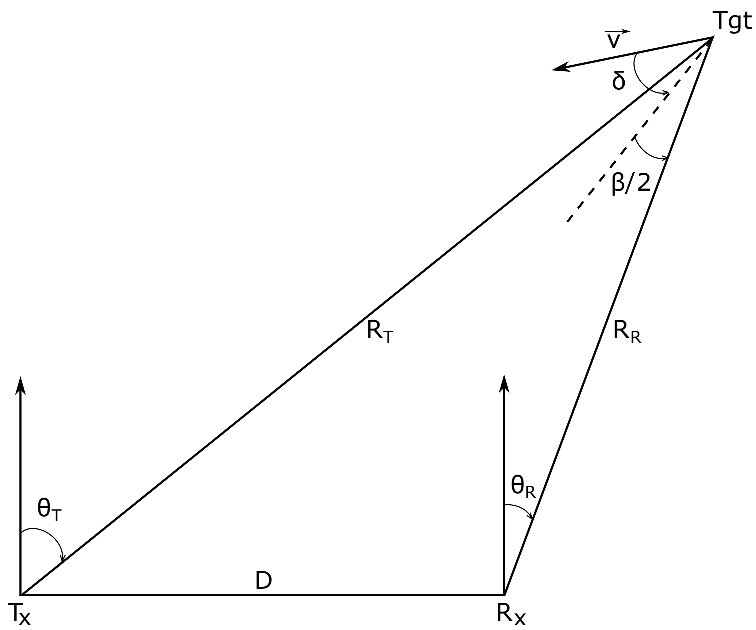

Figure 2.2: Bistatic radar geometry.

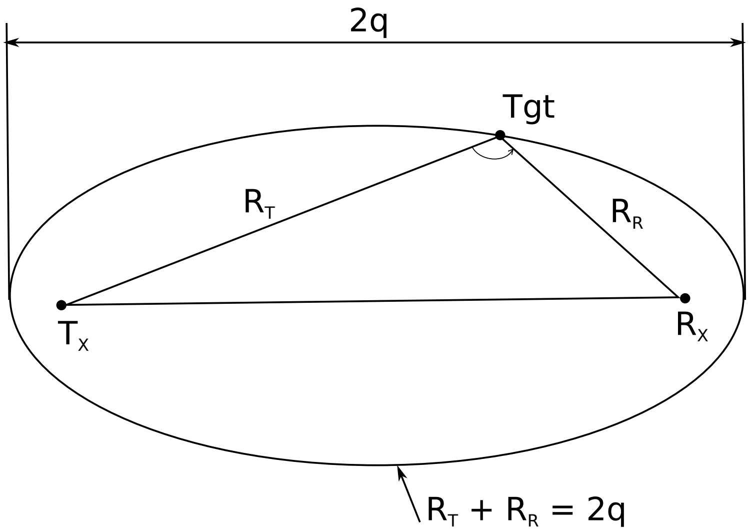

FIGURE 2.3: Bistatic isorange contour.

2.2.3 Bistatic radar range

The derivation of the range equation for bistatic radars is similar to that for monostatic radars [1, 2, 28, 32]. Therefore, the maximum range equation for the bistatic radars can be expressed as

$$(R_R R_T)_{\max} = \left[\frac{P_T G_T \sigma_b G_R \lambda^2 L_s G_p}{(4\pi)^3 \mathrm{SNR}_{\min} k_B T_n B}\right]^{1/2}, \tag{2.3}$$

where

R_T	is the transmitter-to-target range
R_R	is the target-to-receiver range
P_T	is the transmitter power
G_T	is the transmitter antenna gain
σ_b	is the target bistatic radar cross-section
G_R	is the receiver antenna gain
λ	is the signal wavelength
$L_s \leq 1$	are the system losses
G_p	is the coherent processing gain
$\mathrm{SNR}_{\min}$	is the signal-to-noise power ratio required for detection
k_B	is the Boltzmann's constant
T_n	is the receiver noise temperature
B	is the receiver effective bandwidth

The coherent processing gain G_p is given by [1]

$$G_p = T_{\mathrm{CPI}} B, \tag{2.4}$$

where T_{CPI} is the length of the coherent processing interval (CPI). The maximum value of the CPI length is a function of the target dynamic, it is expressed as follows [1]

$$(T_{\text{CPI}})_{max} = \left(\frac{\lambda}{A_R}\right)^{1/2}, \tag{2.5}$$

where A_R is the radial component of target acceleration or simply, the component perpendicular to the isorange contours. If the the CPI length exceeds $(T_{\text{CPI}})_{max}$, range and Doppler walk will result [37].

Obviously, two identical targets at different locations can result in the same SNR. Figure 2.4 shows the ovals of Cassini for a bistatic radar. The ovals of Cassini are contours where the SNR and the product $R_R R_T$ are held constant. As the SNR increases, the size of the ovals is reduced until collapsing around the transmitter and receiver sites. For a certain SNR value, the oval breaks into two parts called a lemniscate, and the point on the baseline is called the cusp [28].

The ovals of Cassini define three operating regions for a bistatic radar: the receiver-centered region, the transmitter-centered region, and the receiver-transmitter-centered region. The receiver-centered region is the small oval around the receiver in figure 2.4; it can be employed for short range ground-based air defense. The transmitter-centered region is presented by the small oval around the transmitter in figure 2.4; it can be used for monitoring the activity around a noncooperative transmitter. The receiver-transmitter-centered region (called also the cosite region) can be any of the ovals of figure 2.4 that surrounds both the transmitter and the receiver; it can be used for medium range air and ground surveillance [28].

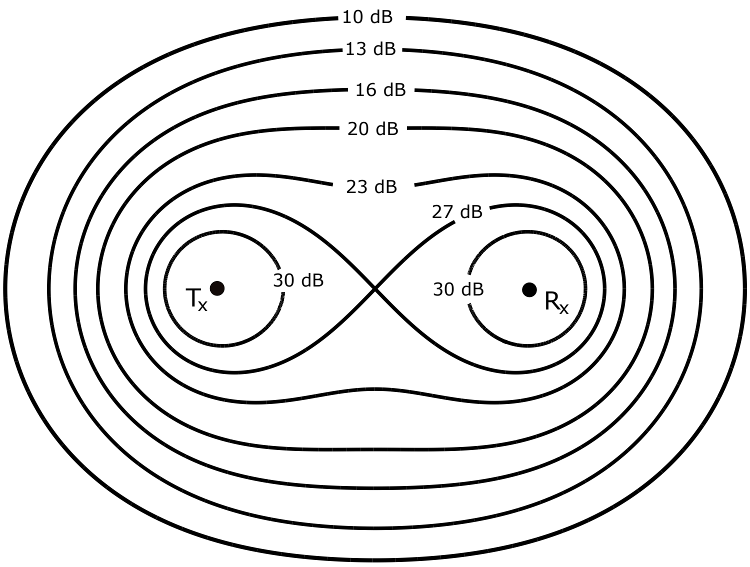

FIGURE 2.4: Contours of constant SNR: ovals of Cassini.

2.2.4 Bistatic radar Doppler

The bistatic Doppler shift is the time rate of change of the total path length of the scattered signal (range rate) normalized by the wavelength [2]. Since the total path length is the sum $(R_T + R_R)$, the bistatic Doppler shift can be expressed as

$$f_B = \frac{1}{\lambda}\left[\frac{\mathrm{d}}{\mathrm{d}t}\left(R_T + R_R\right)\right], \tag{2.6}$$

where λ is the wavelength, R_T is the transmitter-target distance, and R_R is the receiver-target distance. If the transmitter and the receiver are stationary, the expression of the bistatic Doppler shift is given by [28]

$$f_B = \frac{2\upsilon}{\lambda}\cos(\delta)\cos(\beta/2), \tag{2.7}$$

where υ is the magnitude of the target velocity vector and the angles δ (target velocity angle) and β (bistatic angle) are calculated as presented in figure 2.2.

Figure 2.5 presents the bistatic Doppler shift as a function of the bistatic angle β and the target velocity angle δ. The results are obtained considering equation (2.7) with a target velocity magnitude $\upsilon = 100$ m/s and a carrier frequency $f_T = 482$ MHz. For a null value of the bistatic angle ($\beta = 0°$), the monostatic configuration is retrieved and the angle δ represents the angle between the target velocity vector and the monostatic radar-to-target line-of-sight (LOS). For $\beta = 180°$ (the forward-scatter case), the bistatic Doppler shift is null for all target velocity configurations (velocity magnitude and angle). Figure 2.5 shows that:

- for a given target velocity angle δ, the bistatic Doppler shift is always lower than the monostatic case ($\beta = 0°$),
- the bistatic Doppler shift is positive for $-90° < \delta < +90°$,
- for a target velocity vector with an angle $\delta = \pm 90°$, the bistatic Doppler shift is null,
- the bistatic Doppler shift is maximum if the target velocity vector is collinear with the bistatic bisector.

For two collocated targets with echoes frequency-shifted by f_{Tgt1} and f_{Tgt2}, the requirement for the Doppler separation between the two targets is given by

$$|f_{\mathrm{Tgt1}} - f_{\mathrm{Tgt2}}| = \frac{1}{T_{\mathrm{CPI}}}, \tag{2.8}$$

with T_{CPI} is the length of the coherent processing interval. Thus, the required difference between the two target velocity vectors projected onto the bistatic bisector is given by

$$\Delta v = \frac{\lambda}{2T_{\mathrm{CPI}}\cos(\beta/2)}. \tag{2.9}$$

It follows that the Doppler resolution depends on the target position and the CPI length for a given signal.

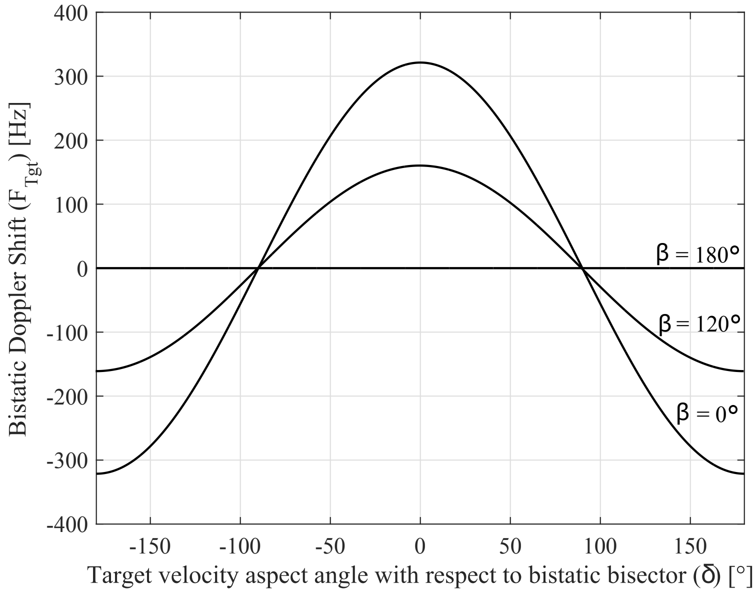

FIGURE 2.5: Bistatic target Doppler for a stationary transmitter, stationary receiver, and a moving target.

2.3 Bistatic PCL radars

This section presents the received signal model for the bistatic PCL radars and defines the detection method employed for this class of radars. In addition, it provides an overview about the possible illumination sources and their characteristics.

2.3.1 Received signal model

As mentioned earlier, PCL radars operate in a silent mode by exploiting illuminators of opportunity. Figure 2.6 depicts the generic geometry of bistatic PCL radars. The receiver architecture consists of two receiving channels: a reference channel to capture the direct-path (DP) signal from the transmitter of opportunity, and a surveillance channel to receive the possible target echoes [38].

The received reference signal, $x_r(n)$, can be expressed as follows [14]

$$x_r(n) = \xi s(n) + v(n), \tag{2.10}$$

where $s(n)$ is the signal transmitted by the illuminator of opportunity with a variance σ_s^2 and ξ is a complex parameter comprising the gain and phase shift for the DP signal. The term $v(n)$ resumes the receiver thermal noise and the multipath contribution, which can be modeled as complex Gaussian noise with zero mean and variance σ_v^2 [14]. The reference antenna is usually highly directive, which allows to neglect the multipath contribution in the reference signal. We define the signal-to-noise ratio of the reference signal as

$$\mathrm{SNR_r} = |\xi|^2 \sigma_s^2 / \sigma_v^2. \tag{2.11}$$

The surveillance signal, $x_s(n)$, is modeled as follows [12]

$$x_s(n) = \sum_{l=0}^{L-1} h_l s(n - \kappa_l) + \sum_{m=0}^{M-1} \alpha_m s(n - \kappa_m) e^{j2\pi f_d(m) n} + w(n), \tag{2.12}$$

where L is the number of the considered multipath components (with time delays κ_l) with complex gains h_l, and M is the number of the moving targets. A target return is a time-delayed (κ_m) and frequency-shifted ($f_d(m)$) attenuated (α_m) copy of the transmitted signal. The quantity $w(n)$ involves the thermal noise of the surveillance channel receiver and the contributing interference sources; it can be considered as complex Gaussian noise with zero mean and variance σ_w^2 [14]. We note the multipath contribution in the surveillance signal as the static clutter, and we define the clutter-to-noise ratio (CNR) as follows

$$\mathrm{CNR} = \sum_{l=0}^{L-1} |h_l|^2 \, \sigma_s^2 / \sigma_w^2, \tag{2.13}$$

and the SNR for each target return as

$$\mathrm{SNR_s(m)} = |\alpha_m|^2 \, \sigma_s^2 / \sigma_w^2. \tag{2.14}$$

We note that the minimum $\mathrm{SNR_s}$ level required for detection (equation 2.3) depends on the quality of the received signals (reference and surveillance signals) [14]. In other words, the detection probability of a target m surely depends on the return power ($\mathrm{SNR_s(m)}$), and in addition, it is a function of the reference signal quality ($\mathrm{SNR_r}$) and the clutter level in the surveillance signal CNR.

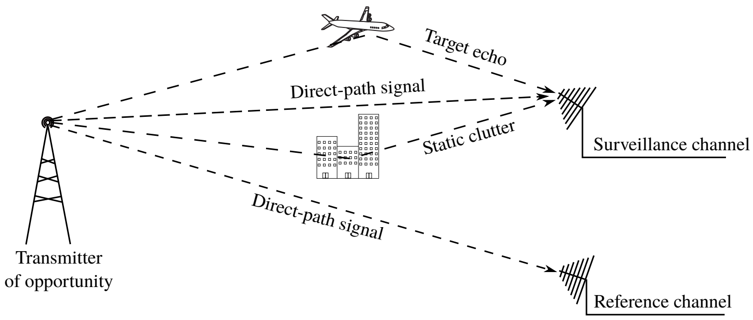

FIGURE 2.6: Received signal model for the bistatic PCL radars.

2.3.2 Cross-correlation detection

The ambiguity function represents the matched filter output [38]. It provides a qualitative assessment of the signal waveform in terms of accuracy, target resolution, and clutter rejection [39]. The ambiguity function of a radar signal for a time delay κ and a Doppler frequency shift ν is given by [40]

$$\Psi_{\mathrm{AF}}(\kappa,\nu) = \left|\sum_{n=0}^{N-1} s(n)s^*(n+\kappa)e^{-j2\pi\nu n}\right|^2, \tag{2.15}$$

where $s(n)$ is the radar signal and N is the number of time samples in the coherent processing interval. The computation of the ambiguity function provides a three-dimensional plot: an axis for the range, the second for the Doppler frequency shift, and the third axis for the output power. This plot is known as the range-Doppler diagram (RDD).

In bistatic PCL radars, the target detection is performed by cross-correlating the surveillance signal and time-delayed and frequency-shifted versions of the reference signal, which is known as the cross-correlation (CC) detection. The CC output is calculated as follows [41]

$$\Psi_{\mathrm{CC}}(\kappa,\nu) = \left|\sum_{n=0}^{N-1} x_s(n)x_r^*(n-\kappa)e^{-j2\pi\nu n}\right|^2. \tag{2.16}$$

The CC detection imitates the matched filter (MF) which maximizes the signal-to-noise ratio of the detector output [31] for a white noise background case. And while the MF employs the exact signal waveform, the CC employs the received reference signal, $x_r(n)$, since the exact signal, $s(n)$, is inaccessible. We note that the detected bistatic range is given by

$$R_b = R_T + R_R - D. \tag{2.17}$$

Figure 2.7 shows a sum of range-Doppler diagrams for simulated data. The diagram presents the path of an aircraft ranging from 1.5 km and 3.5 km. A DVB-T signal is employed as an illuminator of opportunity with a coherent processing interval of $T_{\mathrm{CPI}} = 0.1\ s$. The calculation of the cross-ambiguity function can be cumbersome for large data sets, which may limit real-time processing capabilities [41, 42]. In [38], the principal methods for the cross-ambiguity calculation are studied.

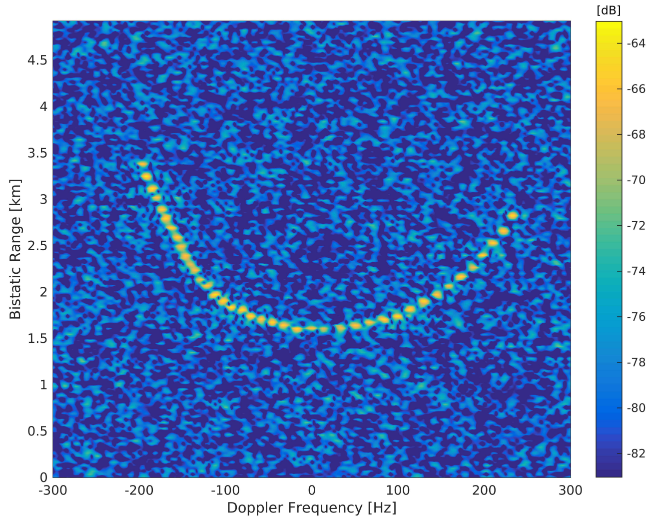

FIGURE 2.7: Simulated range-Doppler diagram.

2.3.3 Review of illumination sources for PCL radars

Several waveforms have been assessed for passive radar usage in [1, 3] such as the analog TV, the FM radio signal, and other digital waveform illumination sources.

The analog TV signals are transmitted in the UHF band with a modulation bandwidth of 5.5 MHz and a radiated power of around 1 MW. The analog TV transmitters have been used as illuminators of opportunity for PCL radars [43, 44] and have achieved a detection range of several hundred kilometers.

FM radio transmitters operate in the VHF band with a bandwidth of 50 kHz and a radiated power of about 250 kW. They are employed for several developed passive radars as illuminators of opportunity [4–6]. The FM based PCL radars are suitable for long-range surveillance since they can detect targets up to 600 km of bistatic range [6].

Another source of illumination is the Global System for Mobile Communication (GSM) base stations [7, 8, 45]. The GSM signals are digitally modulated which yields a noise-like behavior and thus a thumbtack ambiguity function. Two frequencies are employed 900 MHz and 1.8 GHz

Illuminator of opportunity	Frequency	Bandwidth	Power
VHF FM	$\sim$ 100 MHz	50 kHz	250 kW
UHF TV	$\sim$ 550 MHz	5.5 MHz	1 MW
DAB	$\sim$ 220 MHz	220 kHz	10 kW
DVB-T	$\sim$ 750 MHz	7.61 MHz	10 kW
GSM	900 MHz, 1.8 GHz	200 kHz	100 W

Table 2.1: Signal parameters for common illuminators of opportunity [1].

with a bandwidth of 200 kHz. The low radiated power limits the detection range; thus, the GSM signal can be employed for short-range surveillance applications.

Global navigation satellite system (GNSS) satellites can be employed as transmitters of opportunity for passive radars [46, 47]. The availability of GNSS satellites offers a wide coverage, which prompt their use for passive radars.

Digital audio broadcast (DAB) and digital video broadcast terrestrial (DVB-T) have been considered as transmitters of opportunity for many passive radar systems [10–12]. DVB-T signals are noise-like with a bandwidth of 8 MHz, which allows a range resolution of about 33 m. The high radiated power allows the passive radar to perform medium-range surveillance applications.

The capabilities of Wi-Fi based passive radars have been assessed for indoor sensing [48–50]. Wi-Fi based PCL radars can be employed to improve security in public spaces and to identify and track objects of interest.

Table 2.1 summarizes the main parameters of the most common illuminators of opportunity. Each parameter defines one of the system performances. For example, the signal bandwidth defines the range-resolution, and the radiated power defines the maximum detection range. In addition, the signal ambiguity function is a key parameter for the IO choice; it reveals the inherent range and Doppler ambiguities of the signal. Thus, signals with a thumbtack-shaped ambiguity function (such as digital modulated signals) are suitable for PCL radar applications [7].

2.4 Conclusion

In this chapter, we introduced the most important characteristics of the bistatic PCL radars, and we provided the required background for a study about this radar class. We showed the interesting advantages of the PCL radars, and we cited the essential challenges to deal with. We noticed that the bistatic range and velocity depend on the target location in a complex manner different to that for monostatic radars, which complicates the required signal processing and dictates a perfect transmitter-receiver synchronization.

As shown earlier, noncooperative transmitters in the environment can be exploited for passive detection. This can lead to considerable benefits in civilian and military applications such as low cost, interception immunity, and ease of deployment. The choice of an illuminator of opportunity is related to the required performances such as range resolution and maximum range.

In this work, we consider DVB-T transmitters as illuminators of opportunity. This choice is justified by the suitable characteristics of DVB-T signals as an illumination source such as a wide bandwidth, a high radiated power, and the possibility of enhancing the received signal quality. In fact, DVB-T PCL radars can benefit of the known signal structure to apply specific signal processing methods which increase the reference signal quality and remove the static clutter from the surveillance signal. These methods will be studied in the next chapters.

Chapter 3

DVB-T signal as an illumination source for PCL radars

3.1 Introduction

DVB-T signals are an attractive illumination source for PCL radars due to the thumbtack-shaped ambiguity function and the considerable bandwidth. Other advantages of the use of DVB-T signals as IO are related to the signal structure, which allow specific signal processing methods for the received reference and surveillance signals. For instance, the reconstruction of the reference signal enhances its quality by mitigating the accompanying noise [12, 27, 51, 52]. The reference signal reconstruction is performed by demodulating the received signal, and regenerating a synthetic signal based on the retrieved symbols. In addition, the static clutter presenting in the surveillance signal can be estimated and cleared via the estimation of the propagation channel [53–55].

In this chapter, we study the principal characteristics of the DVB-T signal, and we provide an insight about the signal conditioning stages for the received signals. Section 3.2 introduces the orthogonal frequency-division multiplexing (OFDM) modulation method which is adopted by the DVB-T standard. Next, it presents the DVB-T signal structure by defining the subcarrier types and the characteristics of each type. Then, it details the implementation scheme of the DVB-T signal generation, and it defines the guard interval notion.

In section 3.3, we present the signal conditioning methods for the received signal. We introduce the time and frequency synchronization methods. Next, we present the methods of the propagation channel estimation. Then, we introduce the symbol detection stage and we calculate the resulting detection error.

Section 3.4 presents the characteristics of the DVB-T signal. It provides the statistical model of the time-domain signal and its components. Then, it assesses the ambiguity function of the DVB-T signal, and its suitability for PCL applications.

3.2 DVB-T signal modulation

3.2.1 OFDM modulation

Orthogonal frequency-division multiplexing (OFDM) is a digital multi-carrier modulation scheme that employs a large number of orthogonal subcarriers to carry data. Each subcarrier is modulated using phase shift keying (PSK) or quadrature amplitude modulation (QAM) [56, 57]. Figure 3.1 shows the spectrum of the OFDM modulation result; the spectral overlapping of the OFDM modulation subcarriers increases the spectral efficiency.

The OFDM modulation is widely used in both wired and wireless applications such as asymmetric digital subscriber line (ADSL) technology, digital video broadcasting cable (DVB-C), digital audio broadcasting (DAB) systems, and digital video broadcasting terrestrial (DVB-T) transmission [58].

The large application field of the OFDM modulation is due to its remarkable advantages. It achieves high spectral efficiency due to the orthogonality of the employed subcarriers, which results in a nearly rectangular spectrum for a large subcarrier number. In addition, it can be simply and efficiently implemented using the fast Fourier transform (FFT). Moreover, it is robust against narrow-band interference, inter-symbol interference (ISI), and fading due to multipath [59, 60]. Finally, it offers the possibility of operating in single frequency network (SFN) mode [61].

One of the main disadvantages of the OFDM scheme is the high peak-to-average power ratio (PAPR) which leads to signal distortion when passing through amplifiers. Further, the use of guard intervals reduces its spectral efficiency. Furthermore, OFDM modulation is sensitive to Doppler spread and phase noise [62]. Also, an accurate time and frequency synchronization is required to maintain the subcarrier orthogonality [61].

3.2.2 DVB-T signal Structure

The DVB-T standard employs the OFDM modulation with two transmission modes 2K and 8K. The transmitted signal is organized into frames, and each frame is formed by 68 symbols. The number of subcarriers for the 2K mode is $K = 1705$, and that for the 8K mode is $K = 6817$.

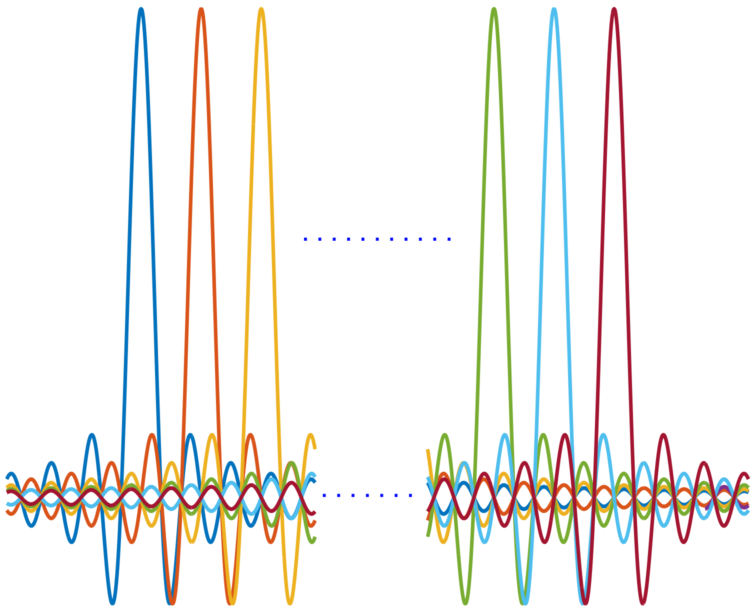

FIGURE 3.1: OFDM signal spectrum.

Each symbol is formed by a useful part of duration T_U and a guard interval of duration T_G. The guard interval is formed by the cyclic prefix, and its duration can be selected from these four values $T_G \in \{T_U/4, T_U/8, T_U/16, T_U/32\}$ [63]. We note the full duration of one DVB-T symbol as T_s, which is given by

$$T_s = T_U + T_G. \tag{3.1}$$

Figure 3.2 presents the DVB-T frame structure. For each DVB-T symbol, the subcarriers transport three types of data: useful data, transmission parameter signaling (TPS), and pilots [12].

Table 3.1 summarizes the main parameters of DVB-T signals for the two transmission modes 2K and 8K. We note $\mathbf{c}$ the array of the coded symbols (data, pilots, and TPS). If we neglect the TPS subcarrier contribution, we can write

$$\mathbf{c} = \begin{pmatrix} \mathbf{c}_d \\ \mathbf{c}_p \end{pmatrix}, \tag{3.2}$$

where $\mathbf{c}_d$ represents the coded data symbols with a size of $K_d \times 1$, and $\mathbf{c}_p$ represents the pilot symbols with a size of $K_p \times 1$. Where K_d and K_p are the number of data subcarriers and the number of pilot subcarriers, respectively.

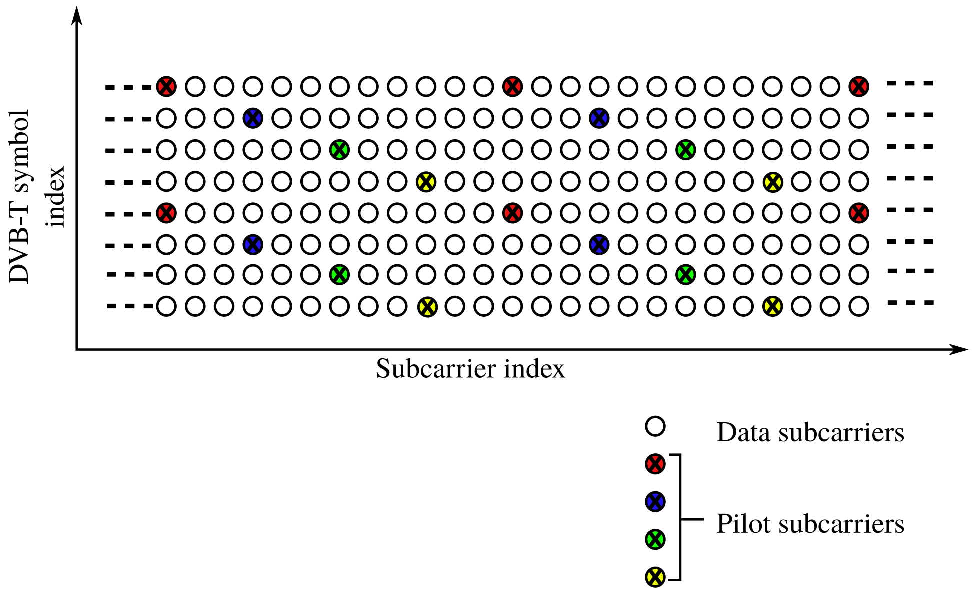

Figure 3.2: DVB-T frame structure.

Parameter	2K mode	8K mode
Number of subcarriers K	1705	6817
Number of data subcarriers K_d	1512	6048
Number of pilot subcarriers K_p	176	701
Number of TPS subcarriers K_{TPS}	17	68
Useful symbol duration T_U	224 μs	896 μs
Subcarrier spacing ΔF	4464 Hz	1116 Hz
Signal bandwidth B	7.61 MHz	7.61 MHz

Table 3.1: Main parameters of the DVB-T signal.

3.2.2.1 Data subcarriers

Data subcarriers are modulated with either QAM symbols, or QPSK symbols. The data bit stream undergoes several stages before being mapped into QAM (or QPSK) symbols; such as outer-coding, outer-interleaving, inner-coding, and inner-interleaving [63]. The coded data symbols, c_d, are normalized to achieve an average power equal to 1:

$$\mathrm{E}\left[c_d\, c_d^*\right] = 1, \tag{3.3}$$

3.2.2.2 Pilot subcarriers

The pilot subcarriers are employed by the receiver for signal synchronization and for received symbol equalization. They are transmitted at known frequencies and with known amplitudes. There are two types of pilots: continual pilots and scattered pilots. The continual pilots occupy

2K				8K									
0	48	54	87	0	48	54	87	141	156	192	201	255	279
141	156	192	201	282	333	432	450	483	525	531	618	636	714
255	279	282	333	759	765	780	804	873	888	918	939	942	969
432	450	483	525	984	1050	1101	1107	1110	1137	1140	1146	1206	1269
531	618	636	714	1323	1377	1491	1683	1704	1752	1758	1791	1845	1860
759	765	780	804	1896	1905	1959	1983	1986	2037	2136	2154	2187	2229
873	888	918	939	2235	2322	2340	2418	2463	2469	2484	2508	2577	2592
942	969	984	1050	2622	2643	2646	2673	2688	2754	2805	2811	2814	2841
1101	1107	1110	1137	2844	2850	2910	2973	3027	3081	3195	3387	3408	3456
1140	1146	1206	1269	3462	3495	3549	3564	3600	3609	3663	3687	3690	3741
1323	1377	1491	1683	3840	3858	3891	3933	3939	4026	4044	4122	4167	4173
1704				4188	4212	4281	4296	4326	4347	4350	4377	4392	4458
				4509	4515	4518	4545	4548	4554	4614	4677	4731	4785
				4899	5091	5112	5160	5166	5199	5253	5268	5304	5313
				5367	5391	5394	5445	5544	5562	5595	5637	5643	5730
				5748	5826	5871	5877	5892	5916	5985	6000	6030	6051
				6054	6081	6096	6162	6213	6219	6222	6249	6252	6258
				6318	6381	6435	6489	6603					

TABLE 3.2: Subcarrier indices for continual pilots.

the same frequencies for all DVB-T symbols as shown in table 3.2. The scattered pilot location varies from one DVB-T symbol to another following a periodic rule. The location of the scattered pilots is calculated by [63]

$$k = 3(i \bmod 4) + 12\ \mathrm{r}|\mathrm{r\ integer}, \mathrm{r} \geq 0,\ k \in \{0 : K-1\}, \tag{3.4}$$

where k is the subcarrier index and i is the DVB-T symbol index ranging form 0 to 67. It follows that the scattered pilot distribution follows four patterns as shown in figure 3.2.

The pilot subcarriers are loaded with a pseudo random binary sequence (PRBS) and transmitted with a boosted power compared to data subcarriers. The pilot symbol amplitudes, c_p, can be $c_p = \pm\frac{4}{3}$, which yields

$$\mathrm{E}\left[c_p\, c_p^*\right] = \frac{16}{9}. \tag{3.5}$$

3.2.2.3 TPS subcarriers

Transmission parameter signaling (TPS) subcarriers convey information related to the transmission scheme parameters such as the channel coding and the modulation type. There are 17

2K					8K							
34	50	209	346	413	34	50	209	346	413	569	595	688
569	595	688	790	901	790	901	1073	1219	1262	1286	1469	1594
1073	1219	1262	1286	1469	1687	1738	1754	1913	2050	2117	2273	2299
594	1687				2392	2494	2605	2777	2923	2966	2990	3173
					3298	3391	3442	3458	3617	3754	3821	3977
					4003	4096	4198	4309	4481	4627	4670	4694
					4877	5002	5095	5146	5162	5321	5458	5525
					5681	5707	5800	5902	6013	6185	6331	6374
					6398	6581	6706	6799				

TABLE 3.3: Subcarrier indices for TPS.

TPS subcarriers in the 2K mode, and 68 TPS subcarriers in the 8K mode. The TPS subcarriers are modulated using a differential binary phase shift keying (BPSK), and occupy the same frequencies for all DVB-T symbols as shown in table 3.3 [63].

Figure 3.3 presents the typical constellation of the transmitted signal employing 64-QAM modulation. Pilot and TPS symbols are real-valued, and data symbols are complex.

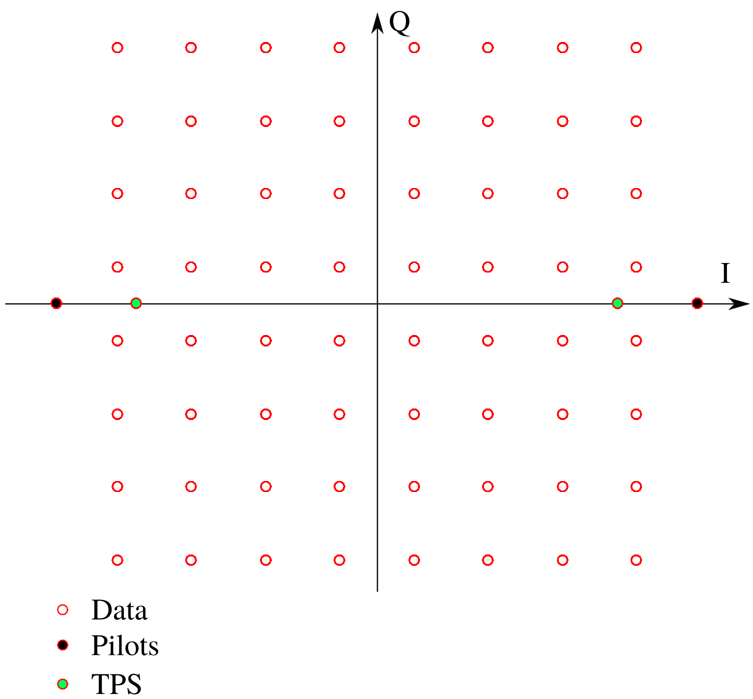

FIGURE 3.3: Constellation of the transmitted DVB-T symbol formed by 64-QAM, TPS, and pilots.

3.2.3 Practical implementation

As mentioned earlier, one DVB-T symbol involves K orthogonal subcarriers. In practice, the fast Fourier transform (FFT) is employed to implement the OFDM modulation as shown in figure 3.4. The K subcarriers are loaded with data, pilot, and TPS symbols (c_k). The IFFT output provides the time-domain useful part of the DVB-T symbol. Then, a guard interval is added to form the full time-domain DVB-T symbol. The model of the resulting signal can be expressed as follows [63]

$$s(n) = \sum_{k=0}^{K-1} c_k e^{j2\pi f_k n}, \tag{3.6}$$

where c_k are the coded symbols (data, pilots, or TPS), and f_k is the frequency of the k^{th} subcarrier given by

$$f_k = \frac{k - K/2}{T_U}. \tag{3.7}$$

Each subcarrier signal is time-limited, which leads to an out-of-band radiation for the full DVB-T symbol, and thus, creates a considerable adjacent channel interference (ACI) [64]. To deal with this issue, the IFFT length N_{FFT} is chosen to be larger than the subcarrier number K, and the remaining $(N_{\mathrm{FFT}} - K)$ bins are set to zero (as shown in figure 3.4) to reduce the edge effect [58, 65]. For example, the 8K-mode employ an FFT block of size $N_{\mathrm{FFT}} = 8192$ and the number of active subcarriers is $K = 6817$.

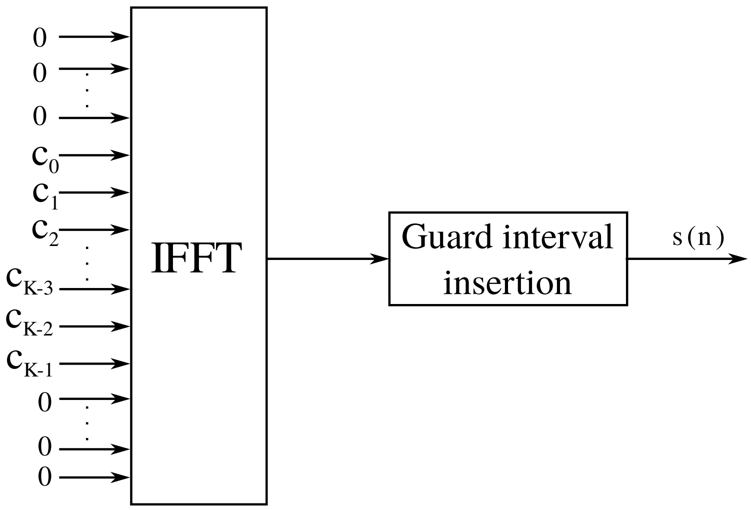

FIGURE 3.4: DVB-T signal modulation.

The guard interval is inserted in the time domain to mitigate the inter-symbol interference (ISI). In the DVB-T standard, the guard interval is a cyclic extension of the useful part of the DVB-T symbol [64]. It consists of copying the last N_G samples of the useful part into its beginning as shown in figure 3.5. Its length, N_G, is chosen longer than or equal to the maximum delay of the multipath channel [64].

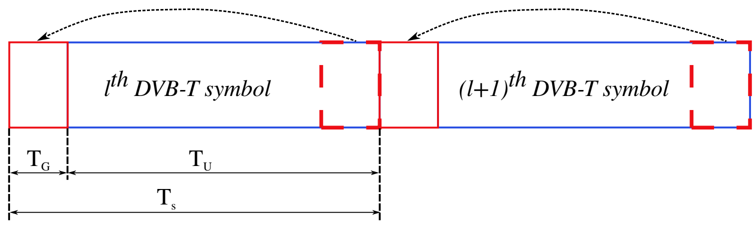

Figure 3.5: Guard interval insertion in DVB-T symbols.

3.3 DVB-T signal demodulation

The DVB-T signal demodulation is a multi-stage operation as shown in figure 3.3. The received signal needs to be time and frequency synchronized. The synchronized signal undergoes an FFT transformation to retrieve the frequency-domain symbols. Next, the propagation channel is estimated and employed for equalization. The equalized symbols are detected to provide an estimate of the transmitted ones.

3.3.1 Signal synchronization

The DVB-T signal synchronization is a crucial task for the receivers. Many research studies have considered this issue [66–74]. The synchronization deals with two challenges: the unknown arrival time of the DVB-T symbol and the possible frequency mismatch between the transmitter and the receiver oscillators. The time synchronization of the DVB-T symbols is required to prevent the inter-symbol interference (ISI), and to achieve an accurate demodulation. And the

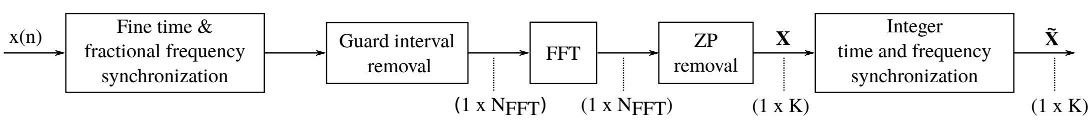

(a) Signal synchronization.

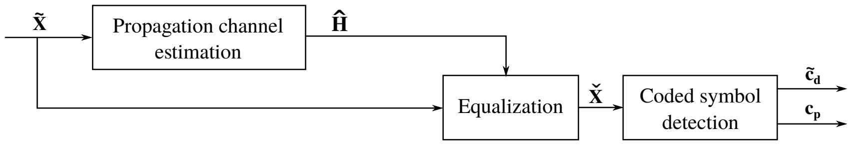

(b) Propagation channel estimation and coded symbol detection.

Figure 3.6: DVB-T signal demodulation.

carrier frequency offset (CFO) compensation maintains the subcarrier orthogonality and avoids inter-carrier interference (ICI).

The DVB-T signal includes sufficient information to achieve an accurate synchronization. The guard interval and the pilot subcarriers are exploited for time and frequency synchronization. The signal synchronization is a multi-stage task as shown in figure 3.6a. Firstly, the time synchronization is performed exploiting the guard interval correlation. Secondly, the fractional frequency offset is estimated and compensated. Thirdly, the integer part of the frequency offset is recovered employing the continual pilots. Finally, the scattered pilot pattern is detected for each DVB-T symbol.

The synchronization schemes assume the knowledge of the guard interval length and the transmission mode (2K or 8K). Usually, these two parameters are known, otherwise, there are methods to accurately estimate them [70, 72].

3.3.1.1 Fine time and fractional frequency synchronization

The aim of the fine time offset estimation is to locate the DVB-T symbol start position. Accurate fine time synchronization allows precise positioning of the FFT window. The fine time offset estimation is performed in the time domain by measuring the correlations of the guard interval for different time delays; the maximum correlation value indicates the correct time offset [66, 69, 71].

As already stated, the guard interval is formed by copying the last N_G samples of the symbol useful part, and inserting them into the beginning of the symbol. The correlation between the guard interval and the last N_G samples of the DVB-T symbol is employed for the fine time offset estimation. Let us consider the following model of the received signal

$$x(n) = s(n - \theta)e^{j2\pi\phi n} + v(n), \tag{3.8}$$

where $s(n)$ is the transmitted signal, θ is the fine time offset, $v(n)$ is an additive white Gaussian noise with a variance σ_v^2, and ϕ is the carrier frequency offset. The carrier frequency offset ϕ is the sum of two components [68, 70]:

$$\phi = \frac{b}{T_U} + \frac{I}{T_U}, \tag{3.9}$$

where $-0.5 \leq b \leq 0.5$ and I is an integer.

The correlation output for the time delay m is given by

$$\gamma(m) = \sum_{n=m}^{m+N_G-1} x(n)x^*(n+N_U), \tag{3.10}$$

where N_U is the number of samples of the DVB-T symbol useful part.

The maximum likelihood (ML) estimate of the fine time offset is obtained by [69]

$$\hat{\theta}_{ML} = \text{argmax}_{\theta}(|\gamma(\theta)|). \tag{3.11}$$

Figure 3.7 presents the magnitude and phase of the correlation defined in (3.10) for simulated DVB-T signal in the 8K-mode and with $N_G = 2048$. The main peaks of the correlation magnitude indicate the beginning of the DVB-T symbols. We note that the knowledge of the guard interval length is required to employ the ML estimation method.

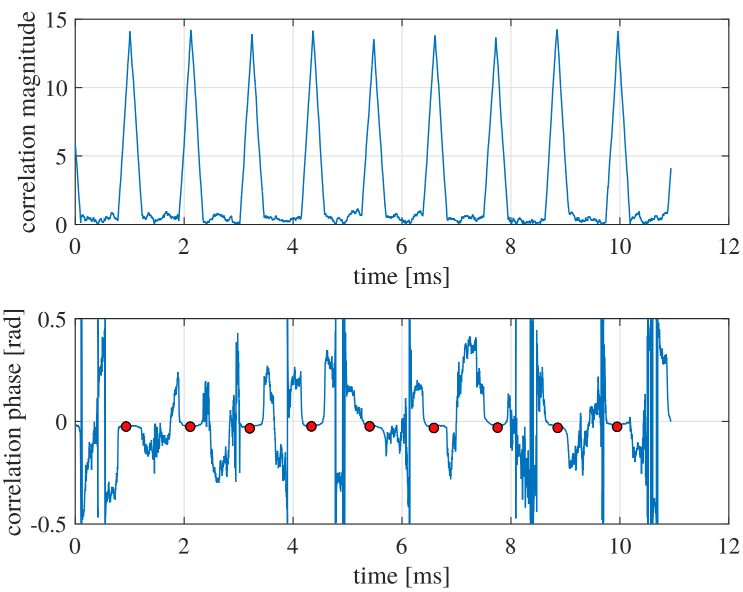

FIGURE 3.7: Maximum likelihood (ML) estimation of fine time and fractional carrier frequency offsets.

The fractional carrier frequency offset can be jointly estimated with the fine time offset [66]. The phase of the main peaks in figure 3.7 (the red circles) indicate the fractional CFO. The ML estimate of the parameter b in (3.9) given by

$$\hat{b}_{ML} = \frac{-1}{2\pi}\angle\gamma(\hat{\theta}_{ML}). \tag{3.12}$$

3.3.1.2 Integer frequency synchronization

After the compensation of the fractional CFO, the post-FFT synchronization stage is feasible. The knowledge of the beginning of the DVB-T symbols allows to split the signal (after fractional CFO compensation) into blocks of size $(N_U + N_G)$. The guard interval is removed from each DVB-T symbol and an FFT is applied on the resulting blocks. We note $X(i,k)$ the elements of the post-FFT results (or the frequency-domain signal), where i is the DVB-T symbol index and k is the subcarrier index.

The continual pilot subcarriers are employed to estimate the integer frequency offset which is a multiple of the subcarrier spacing ΔF. We define the average correlation coefficient as follows [70]

$$\Gamma(k_0) = \frac{\sum_{k\in\Omega_{\mathrm{CP}}} X(i+1,k+k_0)X^*(i,k+k_0)}{\sqrt{\left(\sum_{k\in\Omega_{\mathrm{CP}}} |X(i+1,k+k_0)|^2\right)\left(\sum_{k\in\Omega_{\mathrm{CP}}} |X(i,k+k_0)|^2\right)}}, \tag{3.13}$$

where Ω_{CP} represents the continual subcarrier indices (table 3.2). The integer frequency offset expressed by I in (3.9) is obtained by maximizing $\Gamma(k_0)$:

$$\hat{I}_{ML} = \mathrm{argmax}_{k_0}(|\Gamma(k_0)|). \tag{3.14}$$

Figure 3.8 presents the results of the integer frequency offset estimation. The metric output is maximized for $\hat{I}_{ML} = 2$ which is equivalent to a frequency offset of $2/T_U = 2.232$ kHz. The compensation of the integer frequency offset is then performed to recover the subcarrier orthogonality, which prevents the inter-carrier interference.

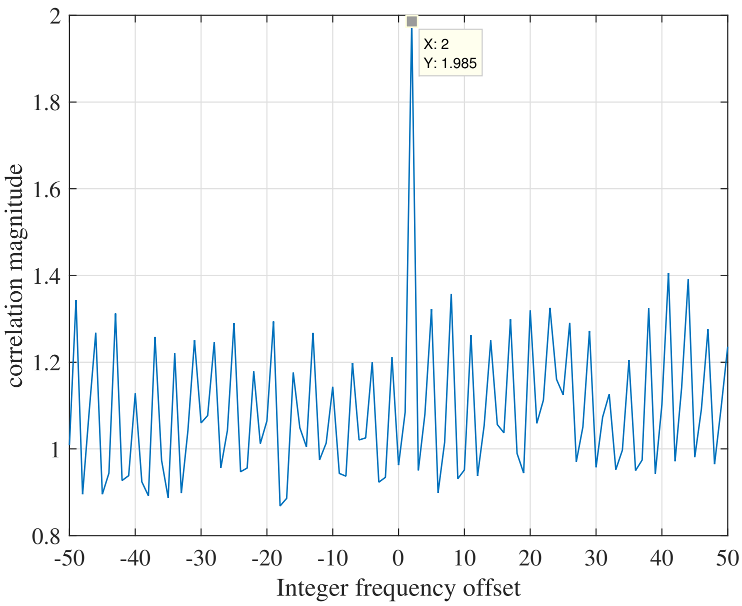

FIGURE 3.8: Integer frequency offset estimation employing continual pilots.

3.3.1.3 Scattered pilot pattern estimation

As shown in section 3.2, the scattered pilot distribution follows a periodic rule, which results in four patterns. The knowledge of the pilot pattern for the i^{th} DVB-T symbol is required to perform an accurate propagation channel estimation. Otherwise, the use of the continual pilots is insufficient to achieve an accurate channel estimation.

The expression in (3.13) can be employed to estimate the scattered pilot pattern for a given DVB-T symbol. Instead of averaging exclusively over the continual pilots, the averaging includes also the scattered pilots for the four patterns. The result is four metrics as shown in figure 3.9. The maximum value refers to the actual scattered pilot pattern; in this case, the pattern number 3 is the pattern of the symbol under test. The scattered pilot pattern estimation is performed for one time; the patterns of the following symbols are deduced since the patterns are periodic.

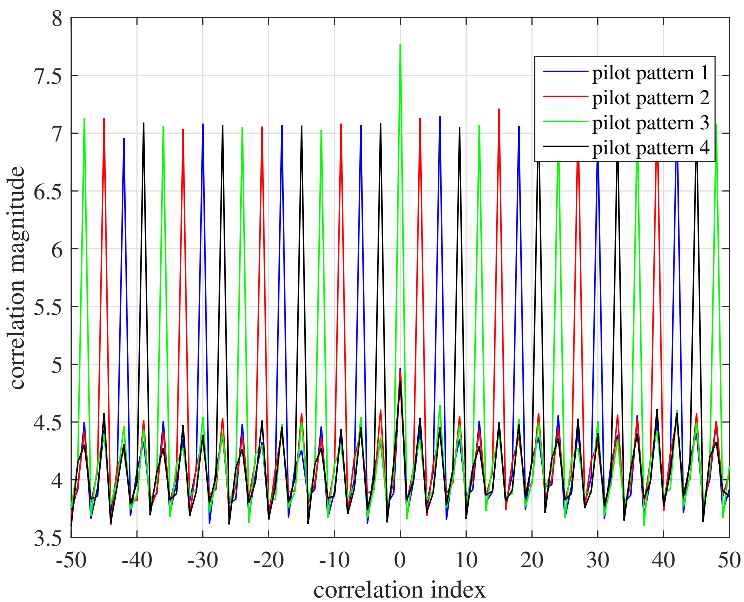

FIGURE 3.9: Estimation of the scattered pilot pattern.

3.3.2 Propagation channel estimation

The transmitted DVB-T signal undergoes various effects such as fading, scattering, and attenuation. Therefore, the receiver must be able to estimate the propagation channel to recover the transmitted data. We assume that the channel response is stationary during the coherent processing interval. In OFDM systems (including DVB-T), the propagation channel is estimated in the frequency domain by employing the pilot subcarriers [60, 75–79]. The most common channel estimation methods for OFDM systems based on pilot subcarriers are: the least squares (LS), the minimum mean square error (MMSE), and the singular-value decomposition (SVD). After the estimation of the channel response at the pilot subcarriers, that response is interpolated to provide the full channel response. We note $\tilde{\mathbf{X}}$ the frequency domain synchronized signal, which can be expressed as follows [75]

$$\tilde{\mathbf{X}} = \mathbf{C}\;\mathbf{H} + \mathbf{V}, \tag{3.15}$$

where $\mathbf{H}$ is the channel response in the frequency domain for the K subcarriers, $\mathbf{V}$ is the Fourier transform of the noise $v(n)$, and $\mathbf{C}$ is a diagonal matrix which includes the transmitted coded symbols (data, pilots, and TPS)

$$\mathbf{C} = \begin{pmatrix} c_1 & 0 & \dots & 0 \\ 0 & c_2 & \ddots & \vdots \\ \vdots & \ddots & \ddots & 0 \\ 0 & \dots & 0 & c_K \end{pmatrix}. \tag{3.16}$$

3.3.2.1 LS channel estimation

The least squares method for the propagation channel estimation is the simplest to implement since it requires no prior information about the propagation channel. To calculate the LS channel response at the pilot subcarriers, the received symbols at the pilot subcarriers, $\tilde{\mathbf{X}}_{\mathbf{p}}$, are extracted

$$\tilde{\mathbf{X}}_{\mathbf{p}} = \mathbf{C}_{\mathbf{p}}\;\mathbf{H}_{\mathbf{p}} + \mathbf{V}_{\mathbf{p}}, \tag{3.17}$$

where the elements of $\tilde{\mathbf{X}}_{\mathbf{p}}$ are retrieved as follows

$$\tilde{X}_p(k) = \tilde{X}(k) \;\text{ with }\; k \in \Omega_{\mathrm{P}}, \tag{3.18}$$

where Ω_{P} represents the pilot subcarrier indices of length $K_P = 176$ for the 2K-mode and $K_P = 701$ for the 8K-mode. The quantities $\mathbf{C}_{\mathbf{p}}$, $\mathbf{H}_{\mathbf{p}}$, and $\mathbf{V}_{\mathbf{p}}$ can be defined in a similar manner.

The channel response based on the LS criterion is given by [76]

$$\hat{\mathbf{H}}_{\mathbf{p},\mathbf{LS}} = \mathbf{C}_{\mathbf{p}}^{\mathbf{-1}}\;\tilde{\mathbf{X}}_{\mathbf{p}}, \tag{3.19}$$

a linear or a polynomial interpolation is then employed to obtain the channel response for the rest of the subcarriers $\hat{\mathbf{H}}$.

3.3.2.2 MMSE channel estimation

The minimum mean square error (MMSE) estimator provides better performances for the channel estimation compared to the LS method. The MMSE method exploits prior information about the propagation channel (correlation matrix of the channel in the frequency domain) and the signal-to-noise ratio (SNR) of the received signal. The MMSE estimate of the channel response for the pilot subcarriers is calculated as follows [77]

$$\hat{\mathbf{H}}_{\mathbf{p},\mathbf{MMSE}} = \mathbf{R}_{\mathbf{H_p}} \left(\mathbf{R}_{\mathbf{H_p}} + \sigma_v^2 \left(\mathbf{C_p} \mathbf{C_p^H} \right)^{-1} \right)^{-1} \hat{\mathbf{H}}_{\mathbf{p},\mathbf{LS}}, \tag{3.20}$$

where $\mathbf{R}_{\mathbf{H_p}}$ is the correlation matrix of the channel at the pilot subcarriers, which is given by

$$\mathbf{R}_{\mathbf{H_p}} = \mathrm{E}\left[\mathbf{H_p} \mathbf{H_p^H} \right]. \tag{3.21}$$

The MMSE estimation method provides an accurate channel estimate, however, its main drawback is the high complexity since it includes matrix inversion operations.

3.3.2.3 SVD channel estimation

The computational complexity of the MMSE method can be reduced by employing a low-rank approximation using the singular value decomposition of the matrix $\mathbf{R}_{\mathbf{H_p}}$. The channel correlation matrix can be decomposed as follows [77]

$$\mathbf{R}_{\mathbf{H_p}} = \mathbf{U} \boldsymbol{\Lambda} \mathbf{U^H}, \tag{3.22}$$

where $\mathbf{U}$ is a matrix with orthonormal columns and $\boldsymbol{\Lambda}$ is a diagonal matrix that includes the singular values.

A new rank u is then chosen smaller than K_p by selecting the most significant singular values, which yields

$$\hat{\mathbf{H}}_{\mathbf{p},\mathbf{SVD}} = \mathbf{U} \begin{pmatrix} \boldsymbol{\Delta}_{\mathbf{u}} & 0 \\ 0 & 0 \end{pmatrix} \mathbf{U^H} \hat{\mathbf{H}}_{\mathbf{p},\mathbf{LS}}, \tag{3.23}$$

where $\boldsymbol{\Delta}_{\mathbf{u}}$ is a diagonal matrix containing a modified version of the singular values [77].

3.3.3 Coded symbol estimation

The estimated response of the propagation channel, $\hat{\mathbf{H}}$, is employed to equalize the symbols $\tilde{\mathbf{X}}$, which compensates the channel impact on the transmitted signal. We note $\check{\mathbf{X}}$ the equalized symbols; they are obtained as follows

$$\check{X}(k) = \tilde{X}(k)/\hat{H}(k). \tag{3.24}$$

The detection of the equalized symbols $\check{\mathbf{X}}$ at data subcarrier positions provides an estimate of the transmitted QAM symbols which we note $\tilde{\mathbf{c}}_d$. The pilot subcarriers are known (frequencies and amplitudes), it follows that the resulting coded symbols after demodulation can be expressed as follows

$$\tilde{\mathbf{c}} = \begin{pmatrix} \tilde{\mathbf{c}}_d \\ \mathbf{c}_p \end{pmatrix}. \tag{3.25}$$

Although, the received signal is synchronized, the residual carrier frequency offset and the phase noise can affect the demodulation process. Thus, an adequate processing is required to compensate these two issues. To demonstrate the signal demodulation chain, we use real measurement sequences and apply the required processing to achieve an accurate symbol detection.

Figure 3.10 presents a post-FFT 64-QAM constellation $\tilde{\mathbf{X}}$. We notice the impact of the propagation channel which led to inter-carrier interference. This can be corrected by the equalization of the post-FFT symbols employing the channel estimate. The equalization result, $\check{\mathbf{X}}$, is depicted in figure 3.11. The constellation symbols are distinguishable, however, the symbol rotation can lead to a significant symbol detection error. The symbol rotation is due to the residual carrier frequency offset and the sampling frequency offset. The solution is a tracking loop for the estimation and the compensation of the residual frequency offset [68, 69, 74].

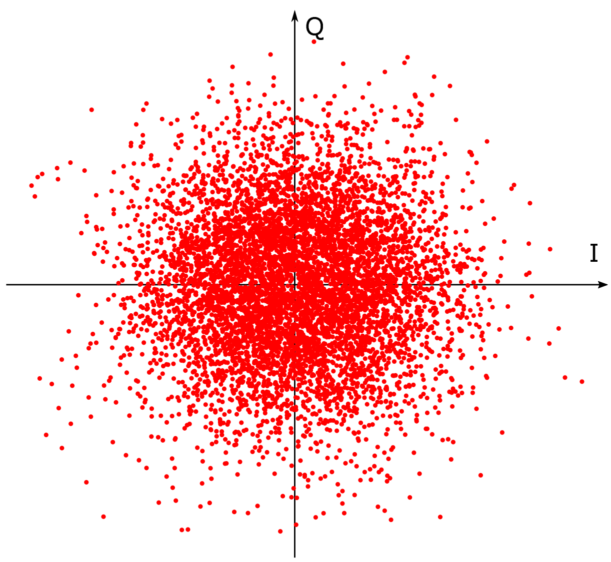

FIGURE 3.10: Post-FFT constellation shows the propagation channel impact.

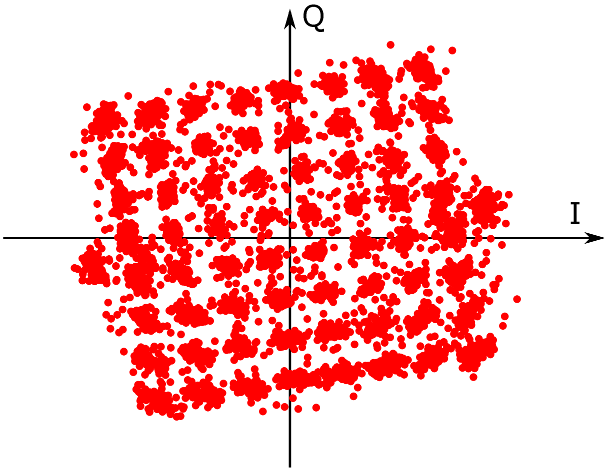

FIGURE 3.11: Equalized constellation with residual CFO and phase noise.

Figure 3.12 presents the constellation after the residual CFO compensation. The symbol rotation is corrected since we can notice that pilot and TPS symbols are with real values (located on the in-phase axis). However, we notice the overlapping of the decision regions especially for the outer symbols, which is due to the phase noise of the receiver local oscillator. Several methods for phase noise correction have been presented [73, 80]. In this work, we consider a decision-directed method [73]; the final result is shown in figure 3.13. Finally, the decision regions of the QAM constellation are clear, which reduces the symbol detection error.

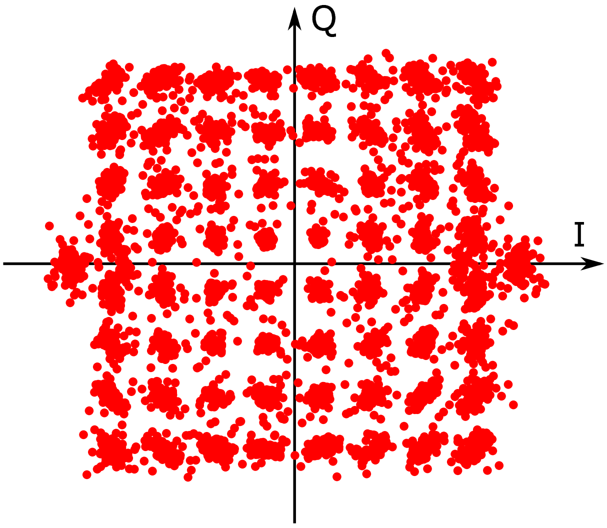

FIGURE 3.12: The received constellation after residual carrier offset correction.

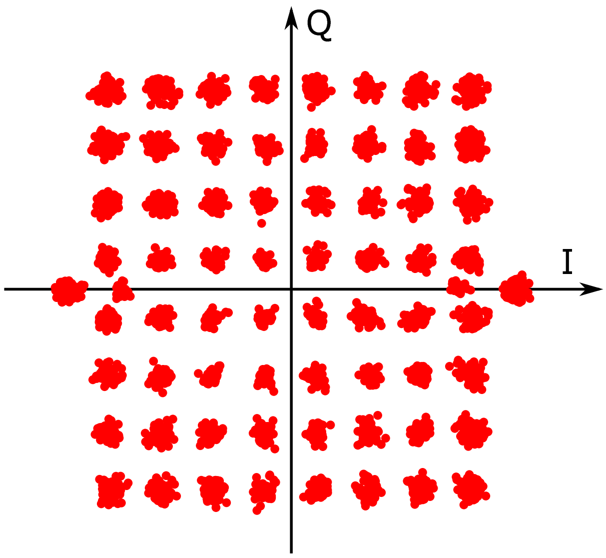

FIGURE 3.13: The received constellation after phase noise correction.

3.3.4 Symbol error rate

Beside the synchronization impact, the accuracy of the coded symbol detection depends on the signal-to-noise ratio of the received signal. Figure 3.14 presents received 64-QAM constellations for DVB-T frames under three SNR scenarios. We notice that the signal noise can induce a serious degradation of the symbol detection accuracy since the received symbols are no more included in the decision regions. We note that the quantity SNR refers to the carrier-to-noise ratio and not to the energy per bit to noise power spectral density ratio E_b/N_0. The two quantities (SNR and E_b/N_0) are related as follows [81]

$$\mathrm{SNR} = \eta E_b/N_0, \tag{3.26}$$

with η is the spectral efficiency, which can be calculated as follows for the 64-QAM DVB-T modulation

$$\eta = \frac{8K}{BT_U}, \tag{3.27}$$

where K is the subcarrier number, B is the signal bandwidth, and T_U is the duration of the useful part of one DVB-T symbol. For instance, in 8K-mode DVB-T signals, we get

$$\mathrm{SNR} \simeq E_b/N_0 + 9 \text{ [dB]}. \tag{3.28}$$

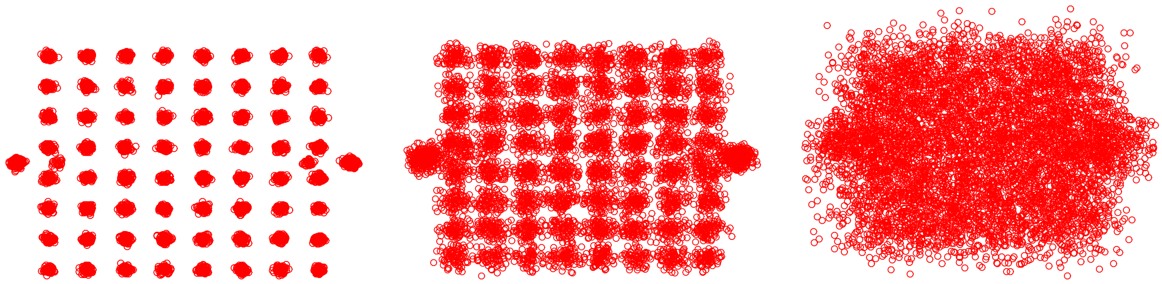

(A) SNR = 30 dB. (B) SNR = 20 dB. (C) SNR = 10 dB.

FIGURE 3.14: Received 64-QAM constellations for different SNR values.

We note $\mathrm{P_e}$ the symbol error rate (SER). For the M-QAM modulation, the SER can be calculated as follows [57]

$$\mathrm{P_e} = 4\left(1-\frac{1}{\sqrt{M}}\right)Q\left(\sqrt{2k_f(E_b/N_0)}\right) - 4\left(1-\frac{2}{\sqrt{M}}+\frac{1}{M}\right)Q^2\left(\sqrt{2k_f(E_b/N_0)}\right), \quad (3.29)$$

where k_f is a normalizing factor given by

$$k_f = \left(\frac{2}{3}(M-1)\right)^{-1/2}, \quad (3.30)$$

and the Q function is given by [57]

$$Q(x) = \frac{1}{\sqrt{2\pi}}\int_x^{+\infty} e^{-t^2/2}dt, \quad (3.31)$$

Figure 3.15 shows the results of the symbol error rate for the 64-QAM modulation employing the theoretical expression and using Monte-Carlo simulations. We notice that to achieve a SER of 10^{-4}, an SNR of 25 dB is required, which demonstrates the sensitivity of the QAM detection accuracy to the quality of the received signal.

3.4 DVB-T signal characteristics

3.4.1 Statistical distribution

As mentioned earlier, the DVB-T subcarriers convey data and pilots. It follows that the resulting time signal, $s(n)$, can be considered as the sum of two components: a data signal and a pilot signal [82–84]. Thus, we can write [84]

$$s(n) = p(n) + d(n), \quad (3.32)$$

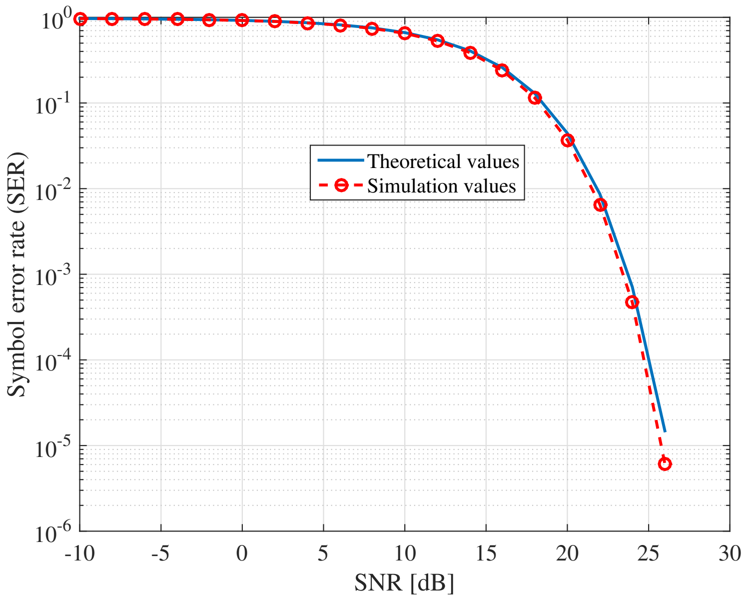

FIGURE 3.15: Symbol error rate (SER) for the 64-QAM.

where $p(n)$ is the pilot signal with a variance σ_p^2, and $d(n)$ is the data signal with a variance σ_d^2. Since data and pilot signals are statistically independent, we can write

$$\sigma_s^2 = \sigma_p^2 + \sigma_d^2. \tag{3.33}$$

The coded symbols c_k (data, TPS, and pilots) are independent identically distributed (i.i.d.) random variables. Data symbols are i.i.d. random variables due to the randomization stage that precede the outer-coder. The latter enhances the data independence together with the outer-interleaver, the inner-coder, and the inner-interleaver [85]. TPS and pilot symbols are i.i.d since they result from a pseudo random binary sequence (PRBS) [63]. In addition, the time-domain signal is obtained through an IFFT of the coded symbols c_k, and the IFFT of statistically independent inputs will produce statistically independent outputs [86]. And the sum of a large number of i.i.d. variables approaches a Gaussian distribution (invoking the central limit theorem). Therefore, we can consider the transmitted DVB-T signal $s(n)$ as Gaussian with zero mean and variance σ_s^2, i.e. $s(n) \sim \mathcal{CN}(0, \sigma_s^2)$ [85–88].

Figure 3.16 presents the probability density function (PDF) for the real part of a simulated DVB-T signal with a duration of 0.1 s which is about 10^6 samples, a 8K transmission mode and, a guard interval length $T_G = T_U/4$. The distribution of the generated data is shown using histogram representation. To illustrate that the obtained distribution is Gaussian, we calculate the mean and variance of the simulated data and employ them to generate the theoretical values for the PDF. The results show a perfect match between the simulation results and the theoretical ones which validates the assumption about the distribution of the DVB-T signal.

Similarly, we can verify that both of the two components data signal and pilot signal follow a complex Gaussian distribution with zero mean and variances σ_d^2 and σ_p^2, respectively. Hence, we can write $d(n) \sim \mathcal{CN}(0, \sigma_d^2)$ and $p(n) \sim \mathcal{CN}(0, \sigma_p^2)$.

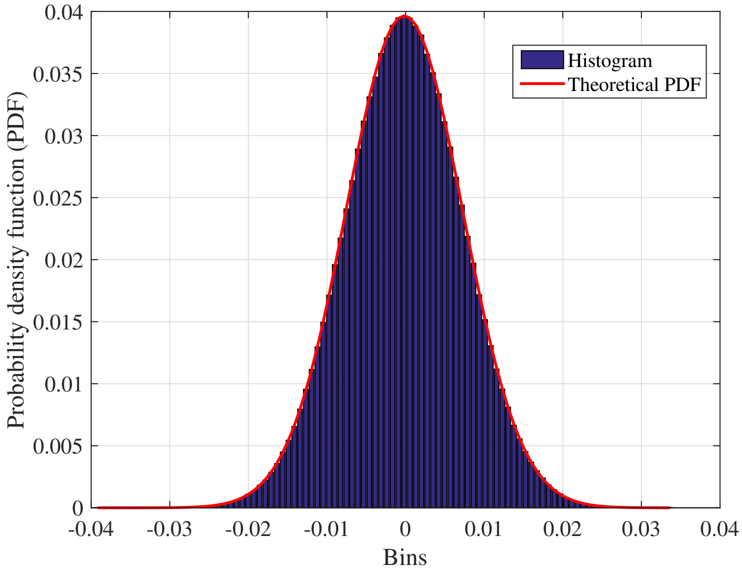

FIGURE 3.16: Statistical distribution of the time-domain DVB-T signal.

3.4.2 Ambiguity function

As previously stated, the ambiguity function represents the matched filter output; it provides an insight about the suitability of the tested waveform for the desired application. The ambiguity function of the DVB-T signal has been the subject of many studies [12, 24, 25, 85, 89–92]; it can be calculated using equation (2.15). Figure 3.17 shows the ambiguity function of a simulated DVB-T signal. The signal is generated with 8K transmission mode, a guard interval length of $T_G = T_U/4$, and a coherent integration interval $T_{\text{CPI}} = 0.1\ s$ which is equivalent to $N = 10^6$. The Doppler frequency range is $[-400\,\text{Hz} : 400\,\text{Hz}]$, and the time delay values are limited to $[-34\,\mu s : 34\,\mu s]$ which yields a maximum range of ± 10 km. The figure shows a strong peak at the origin (zero Doppler and zero range) over a background of -50 dB, and ambiguities -40 dB lower than the main peak. The thumbtack shape of the DVB-T signal ambiguity function is due to the noise-like nature of the signal [7], which is an attractive feature for PCL radars.

The ambiguities are caused by the periodic components of the DVB-T signal such as the guard interval and the pilot subcarriers. Many studies have considered these ambiguities as an additional source of interference and have attempted to deal with it [12, 24, 25, 85, 89–92]. The provided solution is to modify the reference signal by creating a mismatch with the surveillance signal: the guard interval is blanked and the pilot subcarriers are filtered or equalized. The pilot subcarrier equalization is performed by changing their amplitudes (for the reference signal) from $\pm 4/3$ to $\pm 3/4$, which reduces the level of the ambiguities created by the pilots [12].

The ambiguities of the DVB-T signal do not occupy a considerable portion of the range-Doppler domain, and their locations are known. In addition, their power level is about -40dB lower than the main peak, thus, they cannot mask target returns. Further, the most significant ambiguity is caused by the guard interval correlation; and it occurs at a delay T_U which is equivalent to a range of 268 km (higher than the expected maximum detection range). Therefore, in this work, we do not consider any improvement of the DVB-T signal ambiguity function.

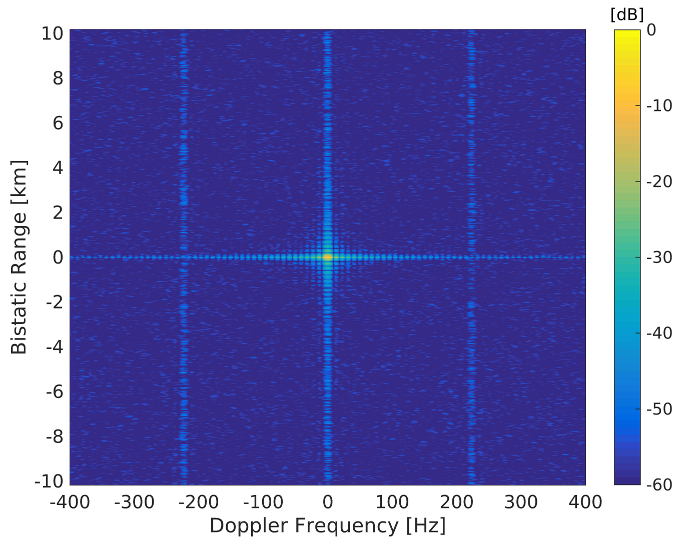

FIGURE 3.17: Simulated ambiguity function of DVB-T signal with a transmission mode 8K, guard interval $T_G = T_U/4$, and coherent integration interval 0.1 s.

Figure 3.18 presents a zero-range cut of the ambiguity function for the DVB-T signal. The similarity with the cardinal sine signal can be clearly noticed, which is due to the rectangular shape of the DVB-T signal spectrum. The Doppler resolution and the sidelobe level depend on the length of the coherent processing interval [85].

Figure 3.19 shows a zero-Doppler cut of the ambiguity function for the DVB-T signal, which provides an insight about the range resolution when employing the DVB-T signal for radar applications. The width of the main peak reflects the range resolution; in fact, the range cell length for DVB-T based PCL radars is around 33 m which makes DVB-T signals an attractive source of illumination for PCL radars.

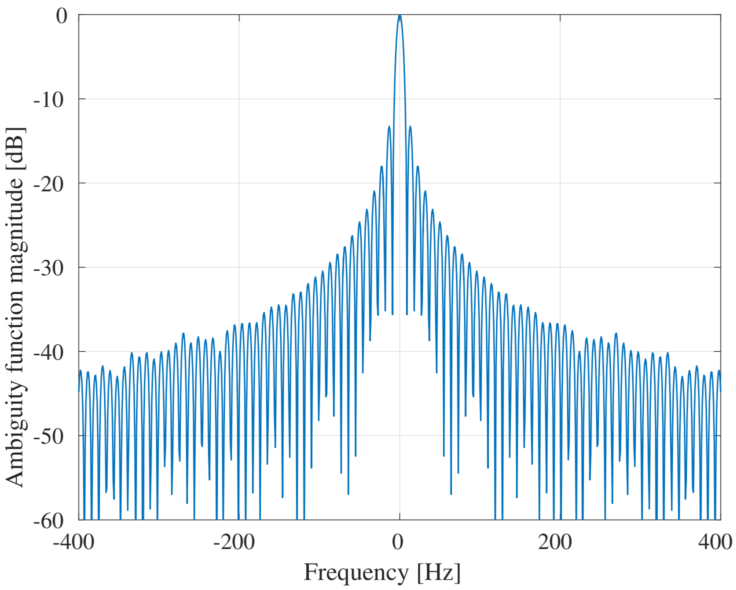

FIGURE 3.18: Zero-range cut of the ambiguity function for DVB-T signal.

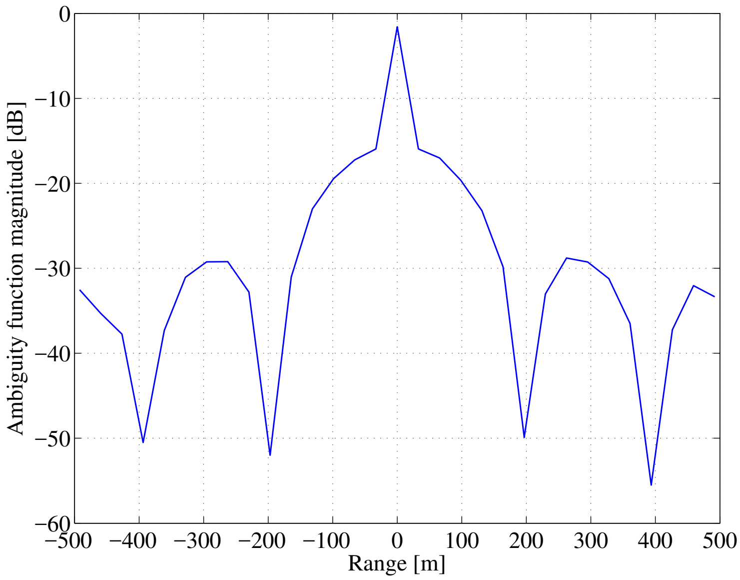

FIGURE 3.19: Zero-Doppler cut of the ambiguity function for DVB-T signal.

3.5 Conclusion

In this chapter, we provided the essential details about the DVB-T signals, and we presented the required signal processing methods that allow an adequate exploitation of the DVB-T signals in PCL radars. We showed that the DVB-T is characterized by a noise-like nature, which results in a thumbtack ambiguity function. We saw that the DVB-T signal follows a Gaussian distribution, which will ease the theoretical study of the detection performances when employing DVB-T signals for PCL radars. We provided also a set of signal processing methods that enables the synchronization of the received signal in time and frequency, the propagation channel estimation, and the symbol decoding.

The well-known structure of the DVB-T signal is an advantage for passive radar applications since it allows a perfect synchronization of the received signals, and permits a set of signal processing methods that enhance their quality. The next chapters study in details the reference signal reconstruction and the static clutter suppression for DVB-T based PCL radars.

Chapter 4

Target detection for DVB-T based PCL radars with a noisy reference signal

4.1 Introduction

The lack of control over the transmitted waves and the ignorance of the exact transmitted signal characterize PCL systems. To deal with the absence of the exact transmitted signal, PCL radars employ a dedicated receiving channel to acquire the direct-path signal which we call the reference signal. The reference signal quality depends on many factors such as the transmitter-receiver distance and the environmental interference sources. In realistic cases, the signal-to-noise ratio of the reference signal can be low, which certainly affects the detection performances [14, 18–20]. In this chapter, we consider a bistatic DVB-T based PCL radar with a noisy reference signal, we assess the impact of this noise, and we study methods that deal with this scenario.

Section 4.2 evaluates the impact of the reference signal noise on the detection performance. First, the difference between the matched filter (MF) and the cross-correlation (CC) detector is presented. Next, the noise impact on the detector output is assessed qualitatively by considering the produced range-Doppler diagrams for different scenarios. Then, we employ the analytic closed-form expression of the detection probability to quantify the impact of the reference signal noise on the detection probability.

In section 4.3, we introduce the reference signal reconstruction strategy which intends to enhance the signal-to-noise ratio of the reference signal. This strategy is feasible for DVB-T based PCL radars; it is performed by decoding the received signal and employing the detected symbols to form a noise-free reference signal. We first present the principle of the reconstruction method. Next, we provide a detailed analytic study of the detection process, which yields closed-form expressions for the false-alarm probability and the detection probability. Then, we show the numerical results for the expected detection probability when a reconstructed reference signal is employed. Finally, we present the limitations of this method.

Section 4.4 proposes a new detection strategy for DVB-T based PCL radars by employing a locally generated pilot signal. The pilot signal is locally generated at the receiver and employed for detection. The pilot signal generation is made possible thanks to the full knowledge of the pilot subcarriers (frequency and amplitudes). Again, we provide the closed-form expression of the detection probability for the proposed method, and we compare the retrieved results with those of a noisy reference signal and a reconstructed signal.

In section 4.5, we present an optimum reconstruction method for the reference signal in DVB-T based PCL radars. It minimizes the mean square error (MSE) between the reconstructed signal and the transmitted one, which extends the feasibility of the reference signal reconstruction for low SNR values.

4.2 Impact of the reference signal noise

In this section, we provide a detailed study about the impact of the reference signal noise on the behavior of the cross-correlation detector. We start by comparing the matched filter and the CC detector. Next, we carry out a qualitative assessment of the noise impact on the target detection by considering its effect on the resulting range-Doppler diagrams. Then, we present the impact of the reference signal noise on the expected detection probability.

4.2.1 Matched filter and cross-correlation detector

In radar applications, the detection filter response is chosen to maximize the signal-to-noise ratio of the detector output, which maximizes the detection probability [33]. The matched filter (MF) is the optimal detection filter for a signal in an additive Gaussian noise background [31, 33, 93]; it maximizes the signal-to-noise ratio of the detector output. The matched filter employs the exact template of the transmitted signal to sense its existence in the received signal. Any modification on the employed signal template reduces the SNR of the detector output and thus, degrades the detection probability.

For PCL radars employing noncooperative transmitters, the exact signal template is inaccessible. Usually, a reference channel is employed to collect the direct-path signal from the illuminator of opportunity. The received reference signal replaces the exact signal employed in the MF detector, and the resulting detection method is called cross-correlation (CC) detector [12, 14]. Consequently, the reference signal quality impacts the detection performance, and the CC detector behavior can approach that of the MF detector for high-quality reference signals.

In realistic scenarios, the distance separating the receiver and the illuminator of opportunity can be considerable, which leads to significant propagation losses and degrades the received signal SNR. In addition, multipath signals and interference sources may further degrade the received reference signal. Therefore, a degradation of the CC detector performance compared to the MF is expected [14, 18–20, 94–97]. In [14], a quantitative assessment of the impact of the reference signal noise on the CC detector performance has been addressed. Such study allows the prediction of the detection probability for different scenarios, it shows that the reference signal SNR affects significantly the detection probability. And for low SNR values, the detection probability is sharply degraded.

Table 4.1 presents the measured signal-to-noise ratio values for different DVB-T transmitters located around Brussels area. The measurements were performed using a Yagi antenna with a gain of 11 dBi and a USRP B100 board. The antenna polarization (vertical or horizontal) followed that of the transmitter. The SNR is calculated following the formula in equation 4.45. We notice that the direct-path signal quality depends on the transmitter-receiver distance; and we remark that for relatively distant transmitters, the SNR is very low. Beside the transmitter-receiver distance, the quality of the received signal depends on transmitter power and the transmitter-receiver visibility.

Therefore, a realistic modeling of the PCL systems requires the consideration of the possible low quality of the reference signal. In this chapter, we consider a low $\mathrm{SNR_r}$ scenario, we assess its impact, and we propose three methods to deal with this scenario for DVB-T based PCL radars.

4.2.2 Qualitative assessment

To specify the exact impact of the reference signal noise on the detection performance, we carry out a qualitative assessment of the CC detector behavior for different $\mathrm{SNR_r}$ values (SNR in the reference signal). In order to do so, we simulate two targets with parameters (range, Doppler, and $\mathrm{SNR_s}$) presented in table 4.2, and a coherent processing interval of length 0.1 s (equivalent to $N = 10^6$ time samples). It has been demonstrated that this value of CPI maximizes the target SNR without inducing range and Doppler walks for DVB-T signals [98, 99]. Figure 4.1 demonstrates the detection strategy by employing the received reference signal.

Name	Power (kW)	Frequency (MHz)	Distance (km)	SNR (dB)
Tour des finances	10	482	2.2	18
Tour des finances	10	754	2.2	20
Veltem	20	482	16	3.8
Wavre	10	754	18	3.2
Antwerpen	10	506	41.7	2.5
Schoten	20	506	50.8	1
Gand	7	482	51.8	-28.7
Genk	20	506	79	-15.6
Tournai	20	754	80.8	-18.2

TABLE 4.1: Measured SNR for different transmitters of opportunity.

	Range [km]	Doppler [Hz]	SNR_s [dB]
Target 1	2	100	-30
Targte 2	1.6	-200	-45

TABLE 4.2: Simulation parameters.

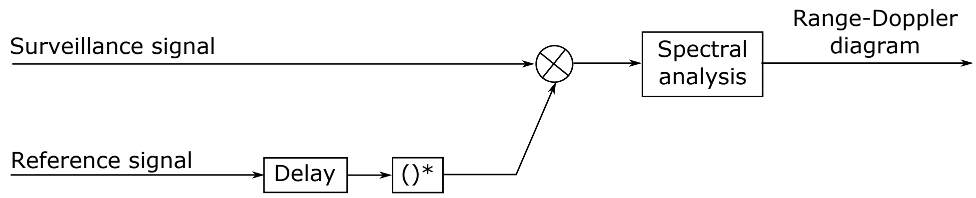

FIGURE 4.1: Detection strategy employing the received reference signal.

Figure 4.2 presents the range-Doppler diagram for a signal-to-noise ratio in the reference signal of $SNR_r = 10$ dB. We notice that both targets are clearly distinguishable since the noise-floor level is considerably lower than the target spots. It follows that the detection threshold for a given false-alarm probability will allow the detection of both targets.

Figure 4.3 shows the range-Doppler diagram for $SNR_r = 0$ dB and with the same simulation parameters as in the previous case. The target with $SNR_s = -30$ dB remains distinguishable, however, the one with $SNR_s = -45$ dB is hardily distinguishable from the noise-floor. The noise-floor rise increases the detection threshold, which leads to miss the detection of the low-magnitude target echoes.

In figure 4.4, we show the range-Doppler diagram for an extreme scenario where the reference signal-to-noise ratio is $SNR_r = -10$ dB. The first target persists distinguishable ($SNR_s = -30$ dB) with a substantial increase of the noise-floor level which buried the second target ($SNR_s = -45$ dB). In this case, low-magnitude target returns are certainly buried, which leads to a significant degradation of the detection probability.

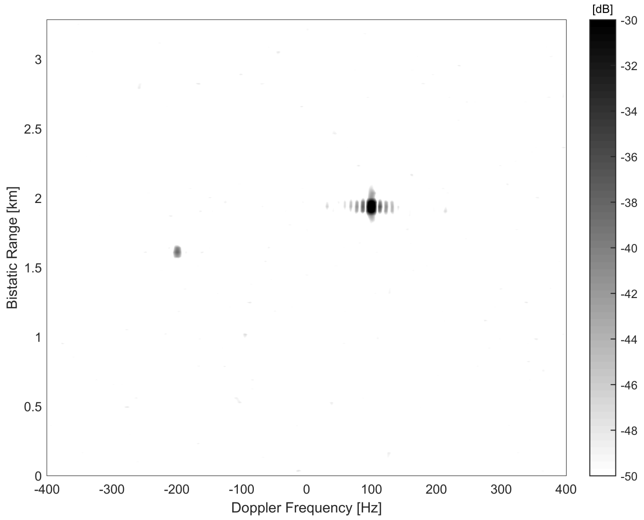

FIGURE 4.2: Range-Doppler diagram for two targets at (2 km, 100 Hz) and (1.6 km, -200 Hz), with $\mathrm{SNR_r} = 10$ dB, $\mathrm{SNR_s}(1) = -30$ dB, $\mathrm{SNR_s}(2) = -45$ dB, and $N = 10^6$.

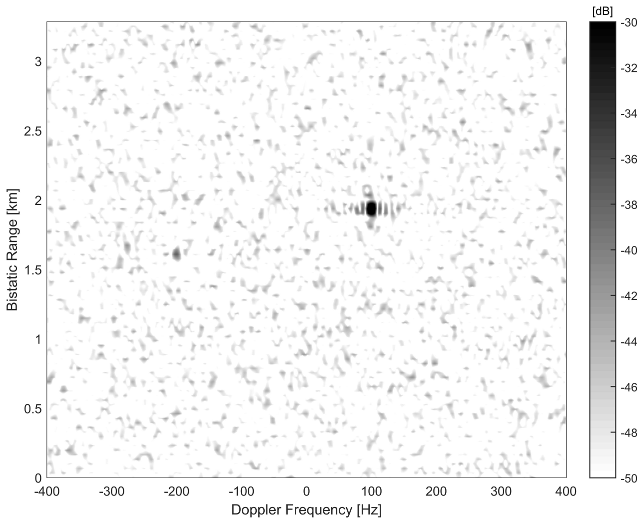

FIGURE 4.3: Range-Doppler diagram for two targets at (2 km, 100 Hz) and (1.6 km, -200 Hz), with $\mathrm{SNR_r} = 0$ dB, $\mathrm{SNR_s}(1) = -30$ dB, $\mathrm{SNR_s}(2) = -45$ dB, and $N = 10^6$.

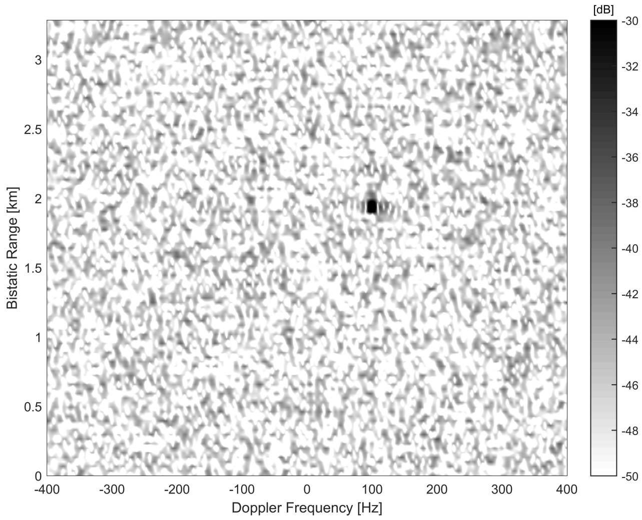

FIGURE 4.4: Range-Doppler diagram for two targets at (2 km, 100 Hz) and (1.6 km, -200 Hz), with $\mathrm{SNR_r} = -10$ dB, $\mathrm{SNR_s}(1) = -30$ dB, $\mathrm{SNR_s}(2) = -45$ dB, and $N = 10^6$.

The previous experiments have shown that the reference signal noise acts by increasing the noise-floor level of the detector output. To illustrate this, we consider cuts of the previous range-Doppler diagrams at the first target range, the results are shown in figure 4.5. We notice that the noise-floor level increases for low $\mathrm{SNR_r}$ values.

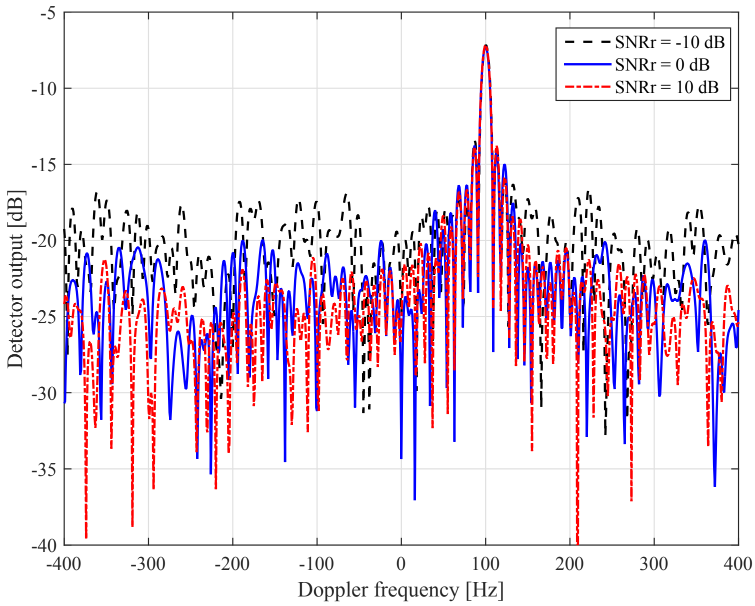

FIGURE 4.5: One-dimensional cut at the target range.

Therefore, we have confirmed that the reference signal noise affects the noise-floor level of the detector output. This can mask low-magnitude target returns, and increases the detection threshold for a given false-alarm probability, which decreases the detection probability. A quantitative study of the reference signal noise impact on the detection performance is required to provide a clearer insight about the extent of this phenomenon.

4.2.3 Quantitative assessment

To quantify the impact of the reference signal noise on the detection performance for the cross-correlation detector, we can calculate the detection probability as a function of $\mathrm{SNR_r}$ [14]. To do so, we consider the reference signal model expressed in equation (2.10). For the surveillance signal, we consider the following simplified model

$$\begin{cases} \mathrm{H}_0 : x_s(n) = w(n), \\ \mathrm{H}_1 : x_s(n) = \alpha s(n-\kappa)e^{j2\pi f_d n} + w(n). \end{cases} \tag{4.1}$$

In the null hypothesis (H_0), no target echo is present in the surveillance signal. And in the alternative hypothesis (H_1), the target echo is present in the surveillance signal with a magnitude α, a time delay κ, and a Doppler shift f_d.

The detection test at the range-Doppler cell (κ, f_d) is performed as follows [14]

$$|\bar{T}|^2 \underset{\mathrm{H}_0}{\overset{\mathrm{H}_1}{\gtrless}} \zeta, \tag{4.2}$$

where ζ is the detection threshold, and $\bar{T}$ is the test statistic which is given by

$$\bar{T} = \sum_{n=0}^{N-1} T(n), \tag{4.3}$$

where N is the length of the coherent processing interval, and the instantaneous output of the detection filter, $T(n)$, is obtained by

$$T(n) = x_s(n)x_r^*(n-\kappa)e^{-j2\pi f_d n}. \tag{4.4}$$

The test statistic $\bar{T}$ follows a complex Gaussian distribution for both hypotheses H_0 and H_1. Under H_0, the distribution parameters (mean and variance) are μ_0 and σ_0^2 with [14]

$$\begin{cases} \mu_0 = 0, \\ \sigma_0^2 = N\sigma_w^2\left(|\xi|^2\sigma_s^2 + \sigma_v^2\right). \end{cases} \tag{4.5}$$

And for the alternative hypothesis H_1, the distribution parameters are [14]

$$\begin{cases} \mu_1 = N\alpha\xi^*\sigma_s^2, \\ \sigma_1^2 = N\left(|\alpha|^2\sigma_s^2\left(|\xi|^2\sigma_s^2+\sigma_v^2\right)+\sigma_w^2\left(|\xi|^2\sigma_s^2+\sigma_v^2\right)\right). \end{cases} \tag{4.6}$$

The detection threshold for a given false-alarm probability $\mathrm{P_{FA}}$ is calculated as follows [14]

$$\zeta = \sigma_0^2 \log(\mathrm{P_{FA}}^{-1}), \tag{4.7}$$

and the closed-form expression of the detection probability $\mathrm{P_D}$ is [14]

$$\mathrm{P_D} = Q_1\left(\sqrt{\frac{2|\mu_1|^2}{\sigma_1^2}}, \sqrt{\frac{2\zeta}{\sigma_1^2}}\right), \tag{4.8}$$

where $Q_1(.,.)$ is the generalized Marcum Q-function of order 1 [100].

Figure 4.6 presents the detection probability contours as a function of $\mathrm{SNR_r}$ and $\mathrm{SNR_s}$. These results are obtained through the expression in (4.8), with a coherent integration interval length $N = 10^5$ and a false-alarm probability $\mathrm{P_{FA}} = 10^{-4}$. We distinguish two regions according to the detection probability behavior. For $\mathrm{SNR_r} > 10$ dB, the detection probability mostly depends on the target echo power ($\mathrm{SNR_s}$). Thus, the $\mathrm{SNR_r}$ level does not significantly affect the detection performance. This limit value depends on the length of the coherent processing interval and the false-alarm probability. For $\mathrm{SNR_r} < 10$ dB, the detection probability is severely affected by the level of the reference signal noise. For a given value of $\mathrm{SNR_s}$, the detection probability sharply decreases for low $\mathrm{SNR_r}$ values, which emphasizes the impact of the reference signal noise. In fact, a decrease of the $\mathrm{SNR_r}$ level is equivalent to a loss of the target echo level ($\mathrm{SNR_s}$). For instance, to achieve a detection probability of 0.9 for $\mathrm{SNR_r} = 0$ dB, an $\mathrm{SNR_s} = -35$ dB is required. However, to achieve the same performance for an $\mathrm{SNR_r} = -10$ dB, the required target echo level is $\mathrm{SNR_s} = -28$ dB, which is equivalent to 7 dB loss in the target echo.

4.3 Reference signal reconstruction

In this section, we present the reference signal reconstruction in DVB-T based PCL radars. This approach aims to enhance the reference signal quality. We first present its principle and feasibility. Next, we carry out an analytic study to retrieve the closed-form expression of the detection probability. Then, we provide the numerical results and we quantify the detection improvement related to the signal reconstruction. Finally, we present the limitations of this method.

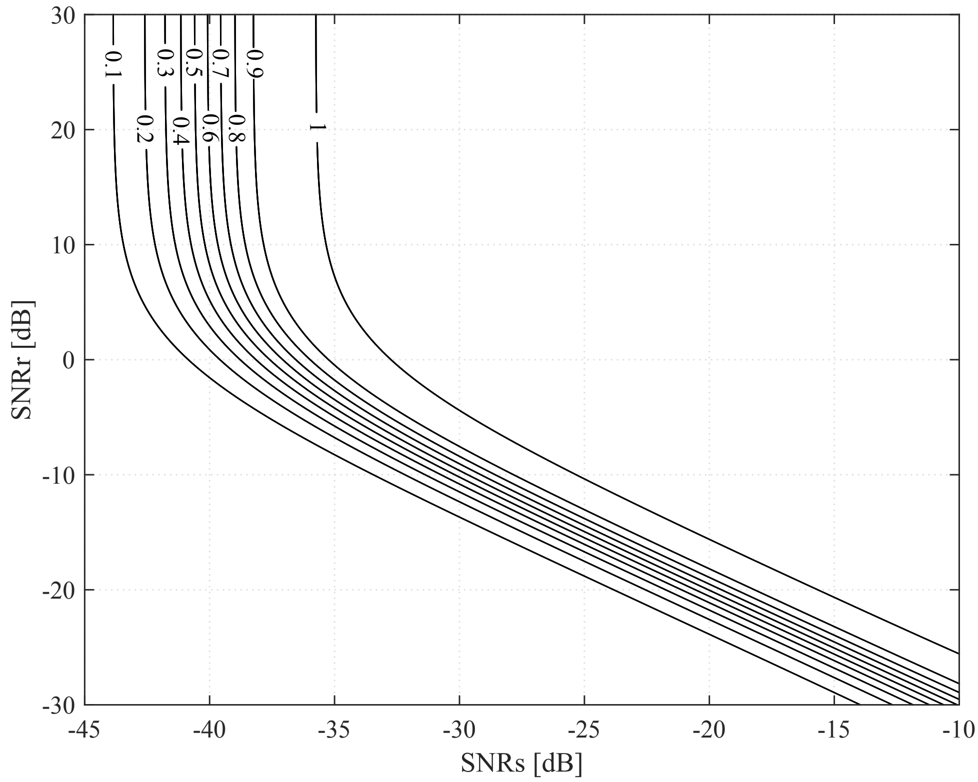

FIGURE 4.6: Detection probability as a function of $\mathrm{SNR_r}$ and $\mathrm{SNR_s}$ with $N = 10^5$ and $\mathrm{P_{FA}} = 10^{-4}$.

4.3.1 Principle

As was mentioned in the previous section, the reference signal noise affects the detection performances. It increases the noise-floor level of the detection filter output, which rises the detection threshold, and thus decreases the detection probability. This impact can be reduced by increasing the length of the coherent processing interval, however, this solution increases the computation cost and causes Doppler and range walk effects [37]. DVB-T based PCL radars can exploit the prior knowledge about the signal structure to reconstruct the received reference signal and create a less-noisy copy of the transmitted signal [9, 26, 27, 51, 101]. The reference signal reconstruction is feasible thanks to the possibility of demodulating the DVB-T signals. Usually, the transmitter parameters such as the transmission mode and the guard interval length are known, which facilitates the signal demodulation.

Figure 4.7 presents the reference signal reconstruction strategy. The signal conditioning stage involves the synchronization and the equalization tasks. The received reference signal is demodulated as presented in chapter 3, which provides an estimate of the transmitted coded symbols that we noted $\tilde{\mathbf{c}}$ (equation 3.25). These symbols are employed to generate a new signal by following the modulation steps in figure 3.4. The resulting signal is called reconstructed reference signal, and it will replace the noisy reference signal for detection.

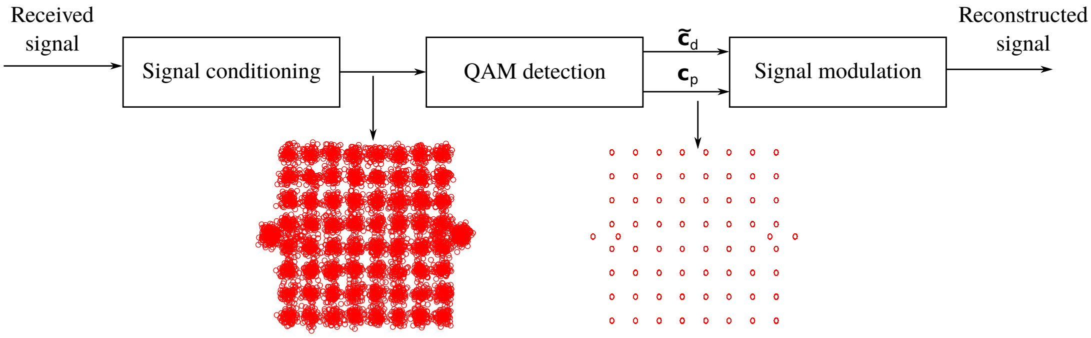

FIGURE 4.7: Reference signal reconstruction principle.

4.3.2 Statistical analysis

To assess the impact of the reference signal reconstruction on the detection performance, we propose to carry out an analytic study of the detection process. The aim of this study is to retrieve closed-form expressions for the test statistic parameters (mean and variance), which allow to calculate the detection probability. In order to do so, we consider a reconstructed reference signal, and the simplified model of the surveillance signal presented in (4.1). We note $\hat{s}(n)$ the reconstructed signal based on the estimated symbols $\tilde{\mathbf{c}}$.

As indicated in chapter 3, the DVB-T signal can be considered as the sum of two signals: data signal and pilot signal. It follows that equation (3.32) can be expressed for the reconstructed signal case as follows

$$\hat{s}(n) = p(n) + \tilde{d}(n), \tag{4.9}$$

where $p(n)$ is the pilot signal, and $\tilde{d}(n)$ is the reconstructed data signal. To retrieve generic expressions for the static test parameters and the detection probability, we adopt the following model for the reconstructed reference signal

$$\hat{s}(n) = p(n) + a\tilde{d}(n), \tag{4.10}$$

where a is a positive parameter.

Figure 4.8 summarizes the detection method employing a reconstructed reference signal. The detection test is performed over all possible range-velocity cells, which results in a range-Doppler diagram. In this section, we intend to characterize the detection test in the target cell (κ, f_d). For the reconstructed reference signal case, the instantaneous output of the detection filter is expressed as follows

$$T(n) = x_s(n)\hat{s}^*(n-\kappa)e^{-j2\pi f_d n}, \tag{4.11}$$

under the alternative hypothesis (H_1), we can write

$$T(n) = \left(\alpha s(n-\kappa)e^{j2\pi f_d n} + w(n)\right)\hat{s}^*(n-\kappa)e^{-j2\pi f_d n}, \tag{4.12}$$

it follows that

$$T(n) = \alpha s(n-\kappa)\hat{s}^*(n-\kappa) + w(n)\hat{s}^*(n-\kappa)e^{-j2\pi f_d n}. \tag{4.13}$$

Since $\hat{s}(n)$ and $w(n)$ are statistically independent, the mean value of the statistic $T(n)$ under H_1 is equivalent to

$$\mathrm{E}\left[T(n)|\mathrm{H}_1\right] = \alpha \mathrm{E}\left[s(n-\kappa)\hat{s}^*(n-\kappa)\right], \tag{4.14}$$

exploiting the fact that the DVB-T signal can be written as the sum of data signal and pilot signal, we get

$$\mathrm{E}\left[T(n)|\mathrm{H}_1\right] = \alpha \mathrm{E}\left[\left(p(n)+d(n)\right)\left(p(n)+a\tilde{d}(n)\right)^*\right], \tag{4.15}$$

so,

$$\mathrm{E}\left[T(n)|\mathrm{H}_1\right] = \alpha \mathrm{E}\left[|p(n)|^2 + ad(n)\tilde{d}^*(n) + ap(n)\tilde{d}^*(n) + p^*(n)d(n)\right], \tag{4.16}$$

since $p(n)$ is statistically independent of $d(n)$ and $\tilde{d}(n)$, we can write

$$\mathrm{E}\left[T(n)|\mathrm{H}_1\right] = \alpha \mathrm{E}\left[|p(n)|^2 + ad(n)\tilde{d}^*(n)\right], \tag{4.17}$$

we have $\mathrm{E}\left[|p(n)|^2\right] = \sigma_p^2$, hence,

$$\mathrm{E}\left[T(n)|\mathrm{H}_1\right] = \alpha\left(\sigma_p^2 + a\mathrm{E}\left[d(n)\tilde{d}^*(n)\right]\right). \tag{4.18}$$

Let us define the quantity ϵ as

$$\epsilon = \mathrm{E}\left[d(n)\tilde{d}^*(n)\right], \tag{4.19}$$

exploiting the definition of the time-domain DVB-T signal in equation (3.6), we can write

$$\epsilon = \mathrm{E}\left[\sum_{k_1=1}^{K_d}\sum_{k_2=1}^{K_d} c_{k_1}\tilde{c}_{k_2}^* e^{j2\pi f_{k_1} n} e^{-j2\pi f_{k_2} n}\right], \tag{4.20}$$

since the subcarriers are orthogonal [12], we get

$$\mathrm{E}\left[c_{k_1}\tilde{c}_{k_2}^* e^{j2\pi f_{k_1} n} e^{-j2\pi f_{k_2} n}\right]_{k_1 \neq k_2} = 0, \tag{4.21}$$

which yields

$$\epsilon = \mathrm{E}\left[\sum_{k=1}^{K_d} c_k \tilde{c}_k^*\right], \tag{4.22}$$

or simply,

$$\epsilon = \sum_{k=1}^{K_d} \mathrm{E}\left[c_k \tilde{c}_k^*\right], \tag{4.23}$$

or

$$\epsilon = K_d \mathrm{E}\left[c_k \tilde{c}_k^*\right]. \tag{4.24}$$

The symbols $\tilde{\mathbf{c}}$ are detected with an error probability $\mathrm{P_e}$, which yields

$$\begin{cases} \tilde{c}_k \neq c_k & \text{with a probability} \;\; \mathrm{P_e}, \\ \tilde{c}_k = c_k & \text{with a probability} \;\; (1-\mathrm{P_e}), \end{cases} \tag{4.25}$$

it follows that [12]

$$\mathrm{E}\left[c_k \tilde{c}_k^*\right]_{\tilde{c}_k \neq c_k} = 0, \tag{4.26}$$

which allows to write equation 4.24 as

$$\epsilon = K_d (1-\mathrm{P_e}) \mathrm{E}\left[c_k c_k^*\right]. \tag{4.27}$$

The variance of the data signal, σ_d^2, can be calculated as follows

$$\sigma_d^2 = K_d \mathrm{E}\left[c_k c_k^*\right], \tag{4.28}$$

hence, we can write

$$\epsilon = (1-\mathrm{P_e})\sigma_d^2, \tag{4.29}$$

finally, we get

$$\mathrm{E}\left[T(n)|\mathrm{H_1}\right] = \alpha \left(\sigma_p^2 + a(1-\mathrm{P_e})\sigma_d^2\right). \tag{4.30}$$

Following the same steps, we get the variance value as

$$\begin{aligned} \mathrm{var}\left[T(n)|\mathrm{H_1}\right] = \; & |\alpha|^2 \left(\sigma_p^4 + a^2(1-\mathrm{P_e})^2\sigma_d^4\right) \\ & + |\alpha|^2 \left(a^2 + 2a(1-\mathrm{P_e}) + 1\right) \sigma_d^2 \sigma_p^2 \\ & + \left(\sigma_p^2 + a^2\sigma_d^2\right) \sigma_w^2. \end{aligned} \tag{4.31}$$

To retrieve the mean and variance of $T(n)$ under $\mathrm{H_1}$, we set $\alpha = 0$.

The test statistic $\bar{T}$ is the sum of N independent and identically distributed random variables $T(n)$. By invoking the central limit theorem [102], we can consider that $\bar{T}$ follows a complex Gaussian distribution with a mean μ_1 and a variance σ_1^2 under the alternative hypothesis ($\mathrm{H_1}$) given by

$$\mu_1 = N\, \mathrm{E}\left[T(n)|\mathrm{H_1}\right], \tag{4.32}$$

$$\sigma_1^2 = N \, \mathrm{var} \left[T(n) | \mathrm{H}_1 \right], \tag{4.33}$$

and a variance σ_1^2 under the null hypothesis (H_0)

$$\sigma_0^2 = N \, \mathrm{var} \left[T(n) | \mathrm{H}_0 \right], \tag{4.34}$$

the mean value under H_0 is null.

To retrieve the analytic values of the detection threshold and the detection probability for the reference reconstruction case, equations (4.32), (4.33), and (4.34) are injected in equations (4.7) and (4.8), respectively. And the parameter a is set to 1.

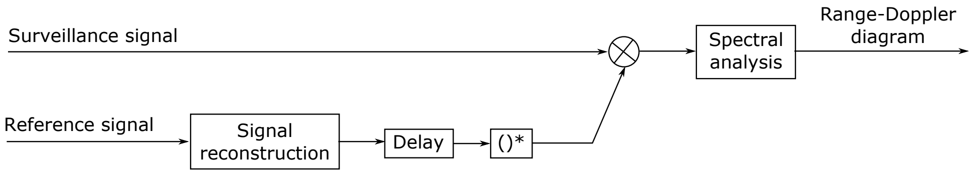

FIGURE 4.8: Detection strategy employing a reconstructed reference signal.

4.3.3 Numerical results

To validate the retrieved closed-form expressions, we carried out Monte-Carlo (MC) simulations for the detection probability with a number of trials $N_{trials} = 10^6$. We employed generated DVB-T sequences of length $N = 10^5$, signal-to-noise ratio of the surveillance signal $\mathrm{SNR_s} = -30$ dB, and false-alarm probability $\mathrm{P_{FA}} = 10^{-4}$. Figure 4.9 presents the theoretical results (TH) for the noisy reference signal and the reconstructed signal, and the MC results for the latter. Firstly, we notice that the theoretical values perfectly match with the MC results, which validates the retrieved analytic expressions. Secondly, we observe a significant improvement of the detection probability for the reconstructed signal case compared to the noisy reference signal, which is due to the improvement of the signal quality (noise reduction) in the reconstructed signal.

To obtain a wider insight about the signal reconstruction impact on the detection performance, we need to evaluate the detection probability for different $\mathrm{SNR_s}$ values. Figure 4.10 shows the detection probability contours, where different values of $\mathrm{SNR_r}$ and $\mathrm{SNR_s}$ are employed with $\mathrm{P_{FA}} = 10^{-4}$ and $N = 10^5$. According to the $\mathrm{SNR_r}$ value, we distinguish two regions. The first one is for $\mathrm{SNR_r} > 10$ dB, the impact of the reference signal noise is insignificant and so is the reconstruction impact. The second region is for $\mathrm{SNR_r} < 10$ dB, the reference signal reconstruction improves the detection probability for all $\mathrm{SNR_s}$ values, which demonstrates the efficiency of the reference signal reconstruction for noise reduction.

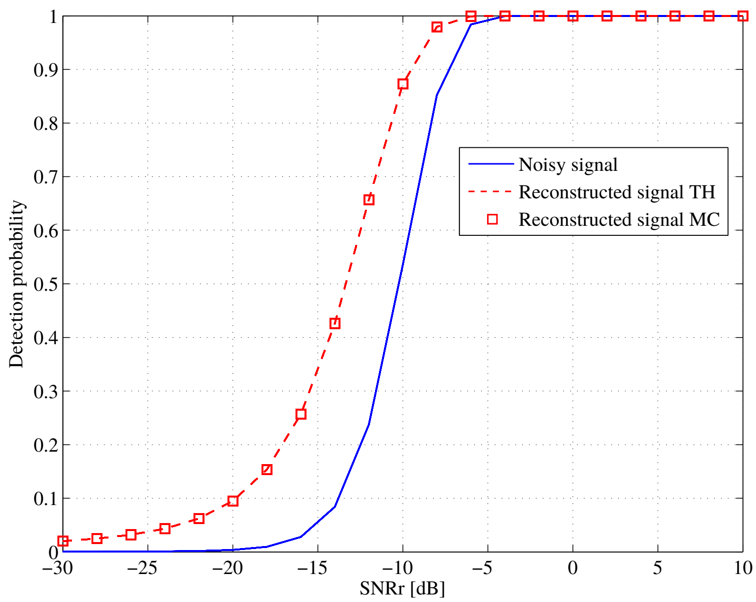

FIGURE 4.9: Detection probability as a function of $\mathrm{SNR_r}$.

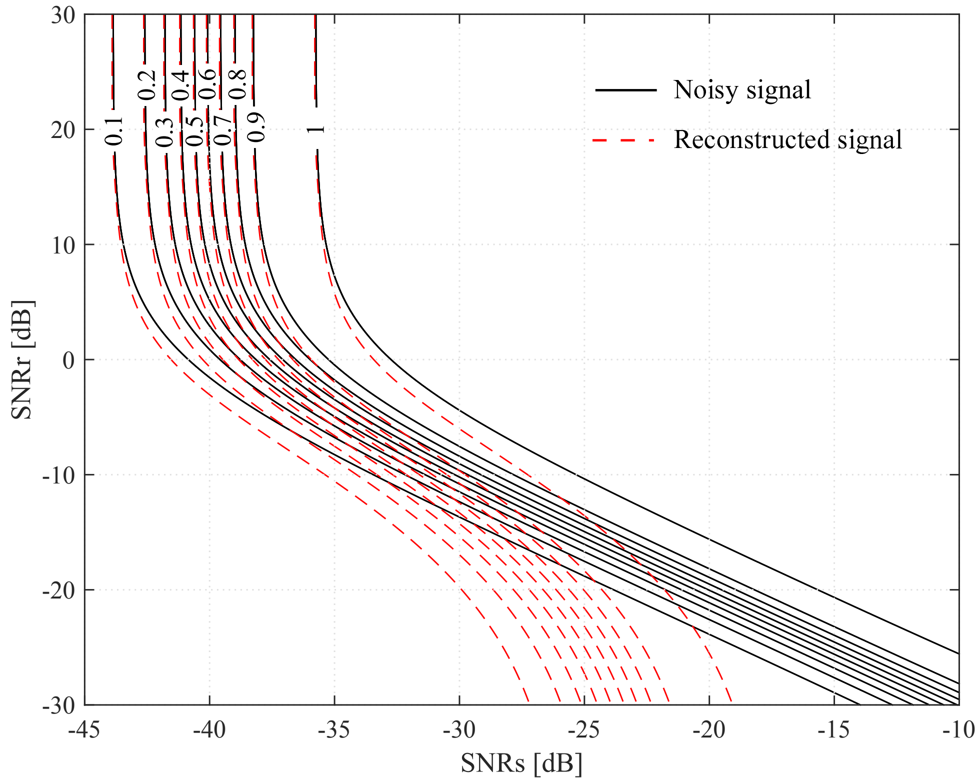

FIGURE 4.10: Detection probability as a function of $\mathrm{SNR_r}$ and $\mathrm{SNR_s}$ with $N = 10^5$ and $\mathrm{P_{FA}} = 10^{-4}$.

4.3.4 Limitations

We noticed that the reference signal reconstruction can be an efficient way for improving the detection probability in DVB-T based PCL radars. However, for low $\mathrm{SNR_r}$, this improvement is limited. Obviously, the performance of the reconstruction method depends on the accuracy of the QAM detection which is a function of the signal-to-noise ratio of the received signal. For low $\mathrm{SNR_r}$ scenarios, the QAM symbol detection error ($\mathrm{P_e}$) is significant, which induces a mismatch between the reconstructed signal and the exact one. In this section, we investigate the impact of the reconstruction mismatch on the detection performance when a reconstructed reference signal is used.

We can show that employing a reconstructed signal which presents a mismatch with the exact signal degrades the coherent integration gain. To do so, we consider a simulation of one target with an echo magnitude $\mathrm{SNR_s} = -30$ dB and a coherent integration interval of length $N = 10^6$. Figure 4.11 shows the results where two reference signal variants are employed: a noisy signal ($\mathrm{SNR_r} = -10$ dB) and a reconstructed one. At the target location (100 Hz), we notice a significant decrease of the peak magnitude (for the reconstructed signal), which is due to the loss in the coherent integration gain caused by the induced reconstruction mismatch.

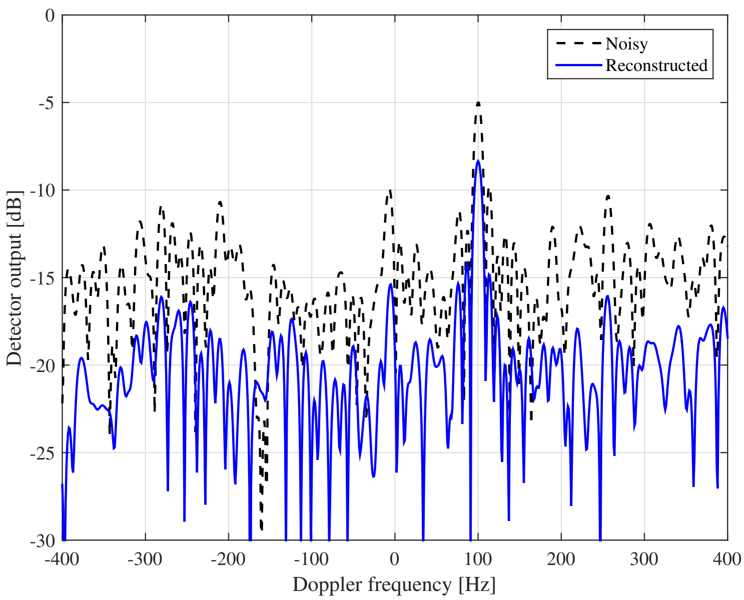

FIGURE 4.11: Coherent integration loss due to the reconstruction mismatch.

To assess the coherent integration loss, we can evaluate the mean value of the statistic test under the alternative hypothesis $\mathrm{H_1}$ expressed in equation (4.32). Figure 4.12 presents the parameter μ_1 as a function of $\mathrm{SNR_r}$ for a CPI length of $N = 10^5$ and a target magnitude $\mathrm{SNR_s} = -35$ dB. The figure compares the parameter μ_1 for a noisy reference signal and for a reconstructed signal.

The results show a significant degradation of the coherent integration for low $\mathrm{SNR_r}$ values, which reduces the efficiency of the reference signal reconstruction for a low $\mathrm{SNR_r}$.

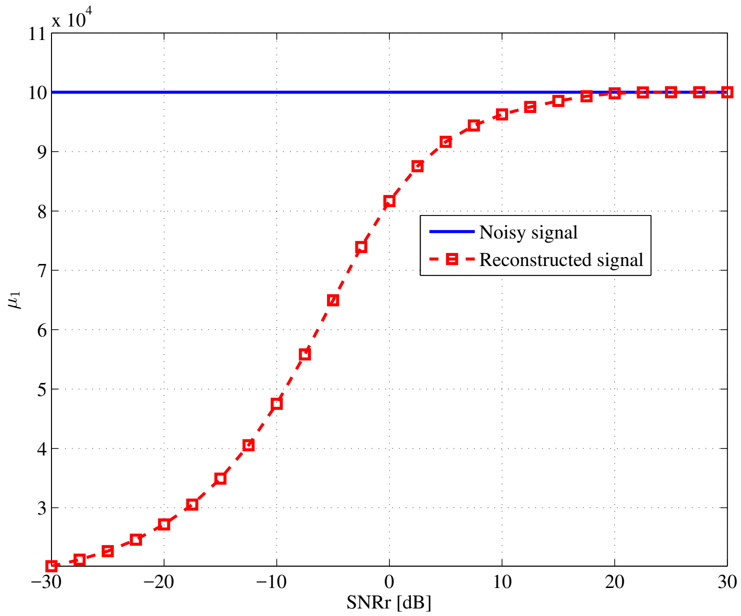

FIGURE 4.12: Mean value of the statistic test $\bar{T}$ under the alternative hypothesis H_1 for $\mathrm{SNR_s} = -35$ dB and $N = 10^5$.

So far, we demonstrated that the reference signal reconstruction loses its performance for low $\mathrm{SNR_r}$ values due to the degradation of the coherent integration gain. In addition to the coherent integration loss, the reconstruction mismatch creates an additional noise source (wrongly reconstructed data signal), which degrades the detection probability. This impact can be assessed by considering the variance of the detection statistic $\bar{T}$ under the null hypothesis H_0. Figure 4.13 presents the variation of the parameter σ_0^2 as a function of $\mathrm{SNR_r}$ for two reference variants: a noisy signal and a reconstructed one. For $\mathrm{SNR_r} < 10$ dB, we notice an increase of σ_0^2 due to the reconstruction mismatch (the wrongly reconstructed data signal), which increases the detection threshold for a given false-alarm probability, and thus, degrades the detection probability.

4.4 Detection employing a pilot signal

In chapter 3, we showed that the DVB-T signal is the sum of two components: a data signal and a pilot signal. The latter is formed by pilot subcarriers; their amplitudes and frequencies are known [63]. Pilot subcarriers represent around 10 % of the total number of subcarriers in the DVB-T signal (176/1705 for 2k – mode and 701/6817 for 8k – mode). They are employed for signal synchronization [74] and propagation channel estimation [60, 76, 79]. In this section, we propose another method for detection in DVB-T based PCL systems by employing the pilot

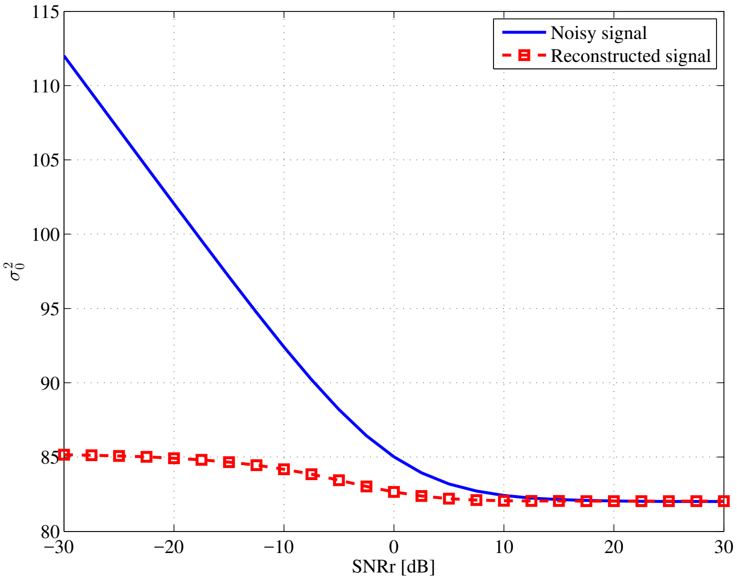

FIGURE 4.13: Variance of the statistic test $\bar{T}$ under the null hypothesis H_0 for $\mathrm{SNR_s} = -35$ dB and $N = 10^5$.

signal; a locally generated pilot signal replaces the received reference signal. This method can improve the detection probability for low $\mathrm{SNR_r}$ values. In addition, it can decrease the system cost since the reference channel will be unnecessary, which is a considerable advantage when employing several transmitters (multi-static scenario).

4.4.1 Principle

Figure 4.14 presents the proposed detection strategy. The received reference signal is replaced by a locally generated pilot signal. The pilot signal is generated by forming DVB-T frames exclusively by pilot subcarriers while data and TPS subcarriers are set to zero. The positions of the pilot subcarriers (continual and scattered) in the symbol are known, and so are their amplitudes. An IFFT is applied on the generated frames and a guard interval is added to obtain the time-domain pilot signal. Then, the pilot signal is cross-correlated with the surveillance signal.

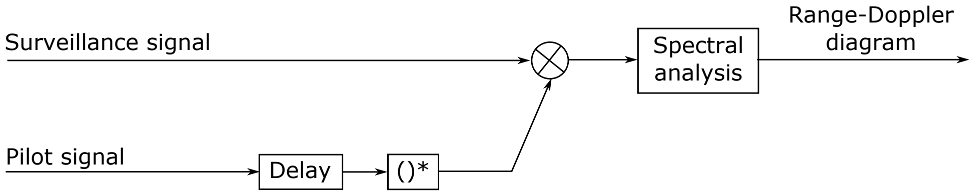

FIGURE 4.14: Detection strategy employing a locally generated pilot signal.

The instantaneous output $T(n)$ of the detection filter for the pilot-based detection can be calculated as follows

$$T(n) = x_s(n)p^*(n-\kappa)e^{-j2\pi f_d n}, \tag{4.35}$$

it follows that the test statistic parameters (mean and variance) can be deduced by setting $a = 0$ in the equations (4.32), (4.33), and (4.34). Hence, we can write

$$\begin{cases} \mu_1 = N\alpha\sigma_p^2, \\ \sigma_0^2 = N\sigma_p^2\sigma_w^2, \\ \sigma_1^2 = N\left(|\alpha|^2\left(\sigma_p^4 + \sigma_d^2\sigma_p^2\right) + \sigma_p^2\sigma_w^2\right). \end{cases} \tag{4.36}$$

These expressions are injected in equations (4.7) and (4.8) to retrieve the detection threshold and the detection probability.

4.4.2 Numerical results

Figure 4.15 presents the detection probability results for three reference signal types: noisy, reconstructed, and pilot signals. We employed the following parameters $\mathrm{SNR_s} = -32$ dB, $\mathrm{P_{FA}} = 10^{-4}$, and $N = 10^5$. Since the pilot signal is locally generated, the detection probability for the approach employing a pilot signal is obviously independent of the $\mathrm{SNR_r}$ value. In addition, employing a pilot signal for detection outperforms the use of a noisy reference signal for $\mathrm{SNR_r} < -7$ dB, which is explained by the fact that for those values, the degradation due to the reference signal noise is larger than that due to the use of a pilot signal only. The pilot-based detection method surpasses the use of a reconstructed signal for $\mathrm{SNR_r} < -9$ dB, this is due to the important integration loss induced by the mismatch between the imperfectly reconstructed signal and the exact one (caused by the QAM detection error).

Figure 4.16 presents the detection probability for the detection method employing pilot signal as a function of $\mathrm{SNR_s}$ for $\mathrm{P_{FA}} = 10^{-4}$ and $N = 10^6$ (equivalent to 0.1 s). We notice that at $\mathrm{SNR_s} = -40$ dB, the detection probability reaches 0.96 which is quite good for realistic cases. Therefore, the use of pilot signal for detection in DVB-T based PCL radars can be an alternative for the noisy reference signal for low $\mathrm{SNR_r}$ values.

4.5 Optimum reference signal reconstruction

In this section, we propose an optimum method for reference signal reconstruction in DVB-T PCL radars. It optimally filters the detected QAM symbols to minimize the mean square error

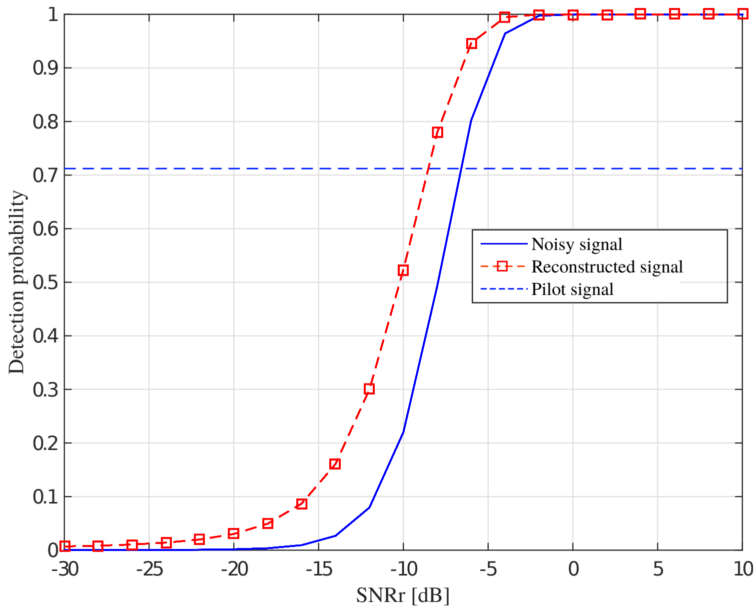

FIGURE 4.15: Detection probability as a function of $\mathrm{SNR_r}$ for $\mathrm{SNR_s} = -32$ dB, $\mathrm{P_{FA}} = 10^{-4}$, and $N = 10^5$.

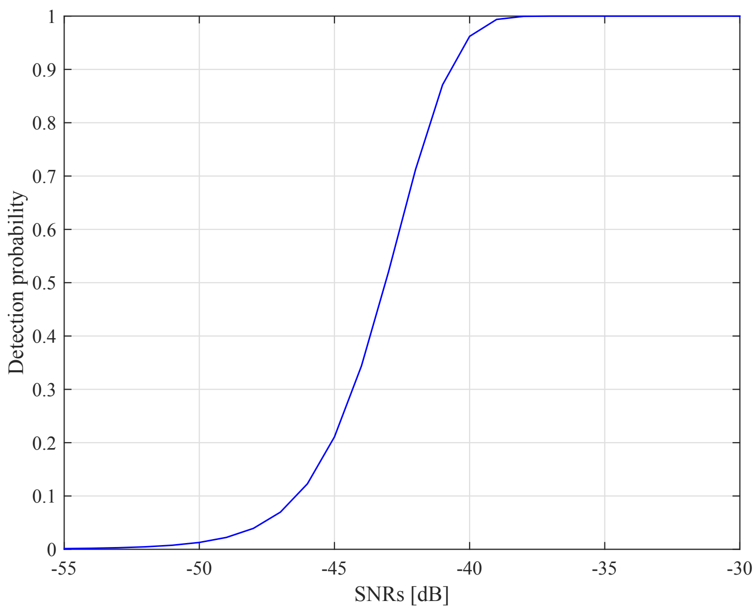

FIGURE 4.16: Detection probability for pilot signal as a function of $\mathrm{SNR_s}$ for $\mathrm{P_{FA}} = 10^{-4}$ and $N = 10^6$.

(MSE) between the reconstructed signal and the transmitted one. This approach is expected to provide performance at leas equal to that of pilot-based method for low $\mathrm{SNR_r}$.

4.5.1 Optimum filter design

As explained earlier, the performance degradation of the conventional signal reconstruction is due to the reconstruction mismatch of the data signal. This degradation is reflected in the integration gain loss and in the additional noise caused by the wrongly reconstructed signal. As seen in section 4.4, the use of a locally generated pilot signal for detection outperforms the conventional reconstruction method for low $\mathrm{SNR_r}$ values. Thus, one can just exclude the use of data signal for low $\mathrm{SNR_r}$ values by setting a threshold at which the pilot detection is better than the conventional reconstruction. However, we know that the conventionally reconstructed signal involves a perfectly reconstructed pilot signal. Therefore, we can design an optimum filter for the reconstructed reference signal, which minimizes the (MSE) between the reconstructed signal and the transmitted one for a given $\mathrm{SNR_r}$ value. Figure 4.17 presents the optimum reconstruction principle.

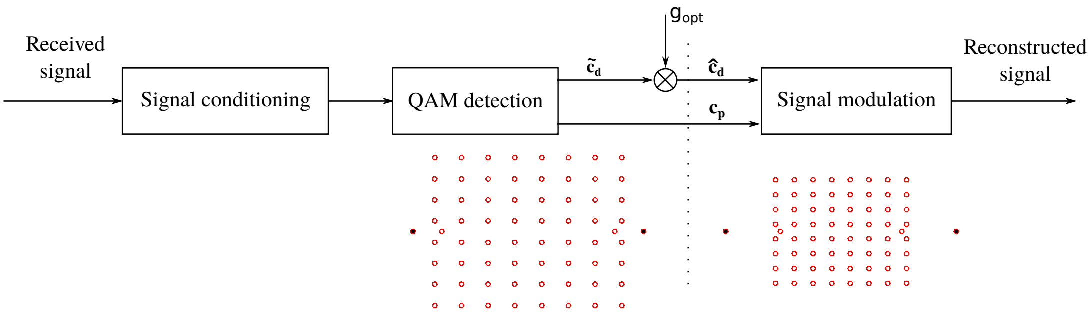

FIGURE 4.17: Principle of the optimum reference signal reconstruction.

As previously stated, the exact signal $s(n)$ and the reconstructed signal $\hat{s}(n)$ are obtained by modulating the coded symbols $\mathbf{c}$ and $\tilde{\mathbf{c}}$, respectively. Thus, minimizing the MSE between $\mathbf{c}$ and $\tilde{\mathbf{c}}$ is equivalent to minimizing it between $s(n)$ and $\hat{s}(n)$. In this section, we aim to optimally filter the detected symbols ($\tilde{\mathbf{c}}$) to minimize the reconstruction MSE. We note $\hat{\mathbf{c}}$ the optimally filtered coded symbols calculated as follows

$$\hat{\mathbf{c}} = \begin{pmatrix} g_d \, \tilde{\mathbf{c}}_d \\ g_p \, \mathbf{c}_p \end{pmatrix}, \tag{4.37}$$

where g_d and g_p are the optimum filter weights for data and pilot symbols, respectively.

The optimum filter weights minimizes the mean square error (MSE) of symbol estimation which we note J. For each symbol c, we can write

$$J = \mathrm{E}\left[|g\tilde{c} - c|^2\right], \tag{4.38}$$

where g is the filter weight. The optimum filter weights are calculated as follows [103]

$$g = \mathrm{E}\left[\tilde{c}c^*\right] / \mathrm{E}\left[\tilde{c}\tilde{c}^*\right]. \tag{4.39}$$

The pilot subcarriers are reconstructed with no error, which yields to $\tilde{c}_p = c_p$, it follows that the filter weights for pilot subcarriers are given by $g_p = 1$. For data subcarriers, we have

$$\tilde{c}_d = c_d \text{ with a probability of } (1 - \mathrm{P_e}), \tag{4.40}$$

and we have $\mathrm{E}\left[\tilde{c}_d c_d^*\right] = 0$ for $\tilde{c}_d \neq c_d$ [12], thus, we can write

$$\mathrm{E}\left[\tilde{c}_d c_d^*\right] = (1 - \mathrm{P_e})\mathrm{E}\left[\tilde{c}_d \tilde{c}_d^*\right], \tag{4.41}$$

hence, the optimum filter weights for data subcarriers are given by

$$g_d = (1 - \mathrm{P_e}), \tag{4.42}$$

therefore, the optimally filtered symbols can be expressed as

$$\hat{\mathbf{c}} = \begin{pmatrix} (1 - \mathrm{P_e})\tilde{\mathbf{c}}_d \\ \mathbf{c}_p \end{pmatrix}. \tag{4.43}$$

The optimally reconstructed signal is obtained my modulating the filtered symbols $\hat{\mathbf{c}}$, it can be expressed as follows

$$\hat{s}(n) = p(n) + (1 - \mathrm{P_e})\tilde{d}(n). \tag{4.44}$$

Figure 4.18 presents the resulting filtered constellations. Obviously, the pilot symbols keep the same amplitudes as before filtering, however, the amplitudes of data symbols are reduced according to the filter weight g_d. This will control the contribution of the data symbols in the reconstructed signal, which reduces the mismatch noise.

Figure 4.19 shows the mean square error (MSE) of the detected data symbols versus the filtered ones as a function of the reference signal SNR. The symbol MSE reflects the mismatch between the reconstructed signal and the exact one. We notice that the proposed method for optimum

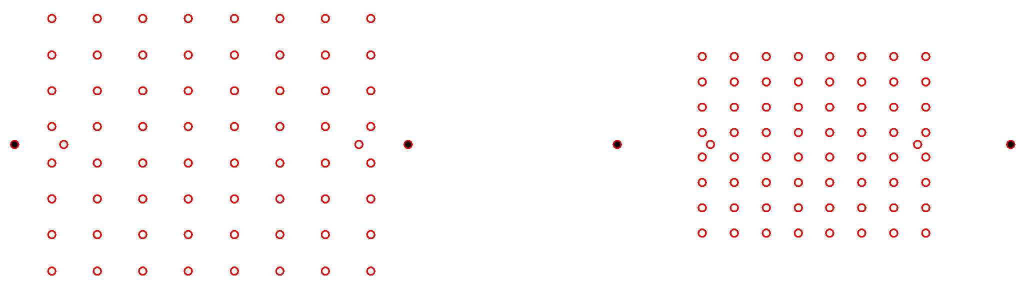

(A) Detected symbols. (B) Filtered symbols.

FIGURE 4.18: QAM symbol filtering.

filtering the detected symbols can reduce the MSE significantly for low SNR values compared to the conventional reconstruction.

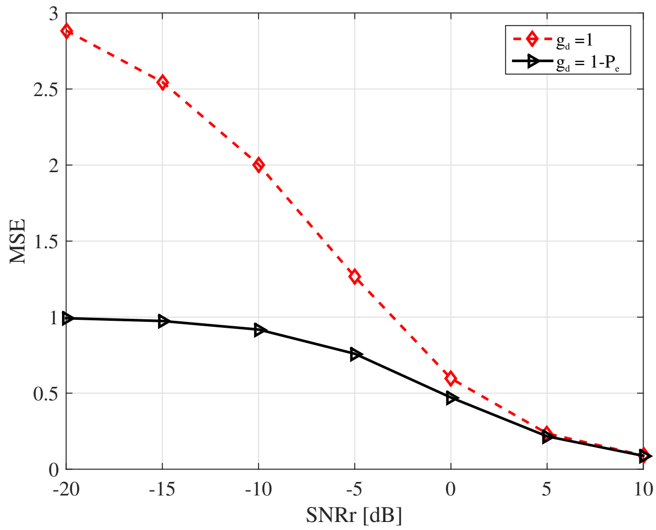

FIGURE 4.19: Mean square error (MSE) of the detected QAM symbols.

Calculating the filter weight g_d requires the knowledge of $\mathrm{P_e}$ which is a function of $\mathrm{SNR_r}$. An estimate of the signal-to-noise ratio in the reference signal can be calculated as follows [84]

$$\hat{\mathrm{SNR}}_{\mathrm{r}} = \frac{|\hat{\xi}|^2 \left(1 + \sigma_d^2/\sigma_p^2\right) \sigma_p^2}{r_x - |\hat{\xi}|^2 \left(1 + \sigma_d^2/\sigma_p^2\right) \sigma_p^2}, \tag{4.45}$$

where r_x is the power of the received reference signal calculated as follows

$$r_x = \mathrm{E}\left[x_r(n) x_r^*(n)\right], \tag{4.46}$$

and $\hat{\xi}$ is an estimate of the parameter ξ in equation (2.10) which is given by

$$\hat{\xi} = r_{xp}/\sigma_p^2, \tag{4.47}$$

with

$$r_{xp} = \mathrm{E}\left[x_r(n)p^*(n)\right]. \tag{4.48}$$

By setting $a = (1 - \mathrm{P_e})$ in the equations (4.32), (4.33), and (4.34), we can calculate the closed-form expressions for test statistics parameters related to the optimum reconstruction method. And to obtain the theoretical detection threshold and detection probability, we inject the retrieved parameters in equations (4.7) and (4.8).

4.5.2 Results

4.5.2.1 Noise-floor reduction

To verify the efficiency of the proposed method for reference signal reconstruction, we first employ a simulated target echo, and we calculate the corresponding range-Doppler diagram (RDD). The target is located at (2 km, 100 Hz) with an echo magnitude of $\mathrm{SNR_s} = -35$ dB, a reference signal with $\mathrm{SNR_r} = -5$ dB, and a coherent integration interval length $N = 10^6$. Figure 4.20 presents the resulting RDD employing the noisy reference signal ($\mathrm{SNR_r} = -5$ dB). We remark that the target is hardly distinguishable due to the considerable increase of the noise-floor level caused by the reference signal noise.

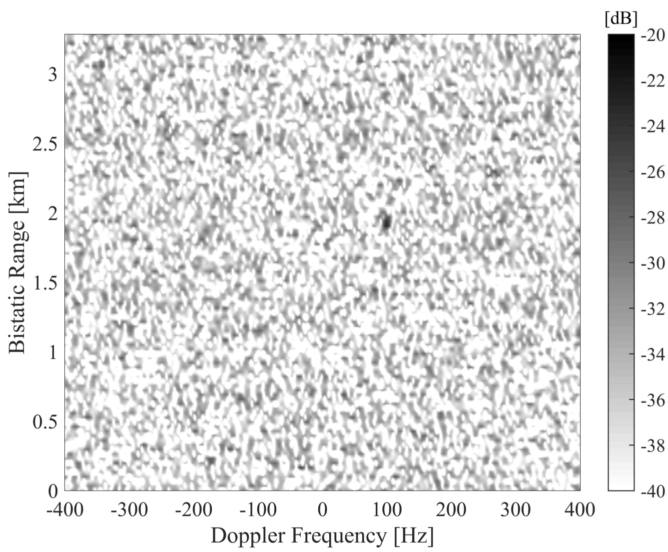

FIGURE 4.20: Range-Doppler diagram for one target at (2 km, 100 Hz) with $\mathrm{SNR_r} = -5$ dB, $\mathrm{SNR_s} = -35$ dB, and $N = 10^6$ (noisy reference signal).

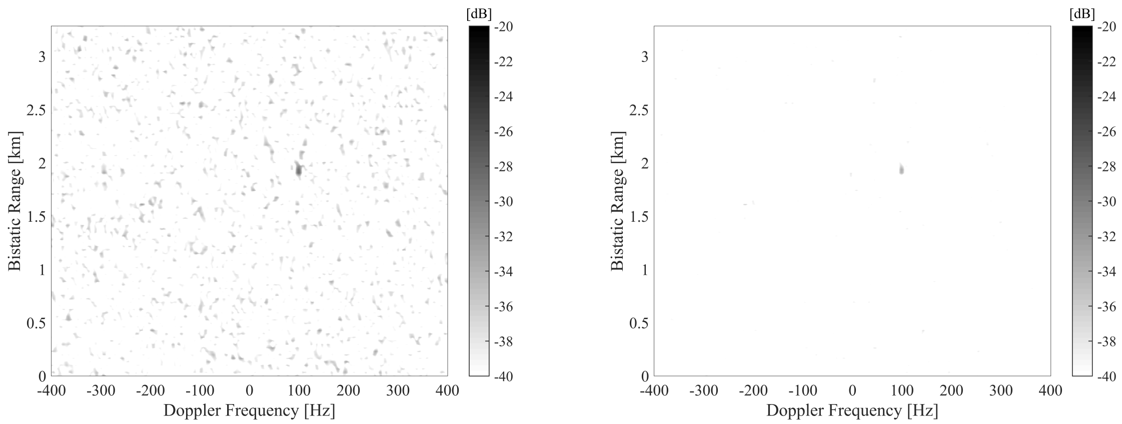

(A) Conventionally reconstructed reference signal. (B) Optimally reconstructed reference signal.

FIGURE 4.21: Range-Doppler diagram for one target at (2 km, 100 Hz) with $\mathrm{SNR_r} = -5$ dB, $\mathrm{SNR_s} = -35$ dB, and $N = 10^6$.

To reduce the reference signal noise, we perform a conventional reconstruction and an optimum one. Figure 4.21 presents the obtained results. We notice that the conventional reconstruction has reduced the noise-floor level, however, the residual peaks may obstruct the target detection or declare false-alarms. In contrast, the proposed method for reference signal reconstruction results in a clearly distinguishable target spot with a magnitude significantly higher than the noise-floor level, which illustrates the effectiveness of the proposed method.

The optimum filtering acts by reducing the mismatch between the reconstructed signal and the exact one, which results in a reduction of the additional reconstruction noise, and thus, decreases the noise-floor level of the detection filter output. To assess the behavior of the noise-floor level we consider the variance of the the statistic test $\bar{T}$ under the null hypothesis H_0. Figure 4.22 presents the parameter σ_0^2 (which reflects the noise-floor level) as a function of $\mathrm{SNR_r}$. For $\mathrm{SNR_r} < 10$ dB, the resulting σ_0^2 value for the optimally reconstructed signal is lower than that for the conventionally reconstructed signal, which illustrates the efficiency of the optimum reconstruction for noise-floor reduction.

4.5.2.2 Real-data results

To validate the retrieved results, we compare the impact of the conventional and optimum reconstruction methods on real-data sets. The recorded DVB-T signals correspond to the Veltem transmitter (table 4.1) with a baseline of 16 km and an $\mathrm{SNR_r} = 3.8$ dB. Figure 4.23 presents the sum of many range-Doppler diagrams which emphasizes the airplane path; the received reference signal is used to obtain these results. In addition, the figure shows the exact airplane path obtained via automatic dependent surveillance-broadcast (ADS-B) signals (detailed in

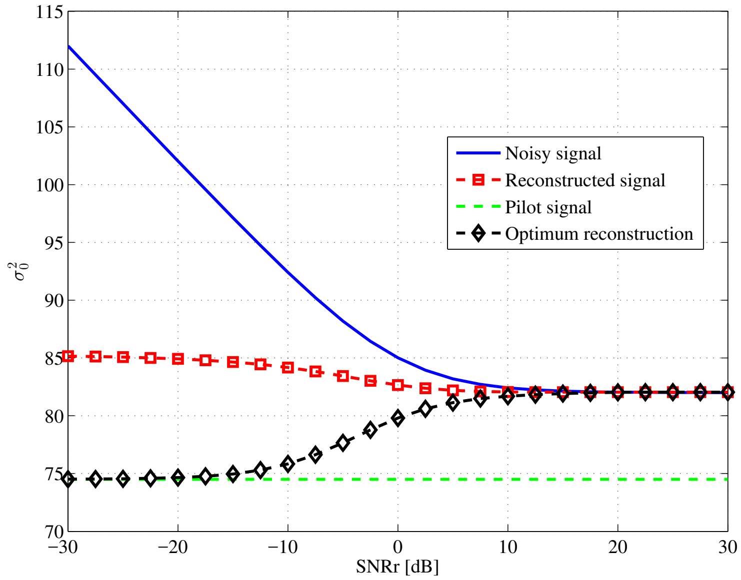

FIGURE 4.22: Variance of the statistic test $\bar{T}$ under the null hypothesis H_0 for $SNR_s = -35$ dB and $N = 10^5$.

chapter 6). The results correspond to an airplane during the take-off maneuver. We notice that the airplane track is hardly distinguishable due to the considerable increase of the noise-floor level caused by the reference signal noise.

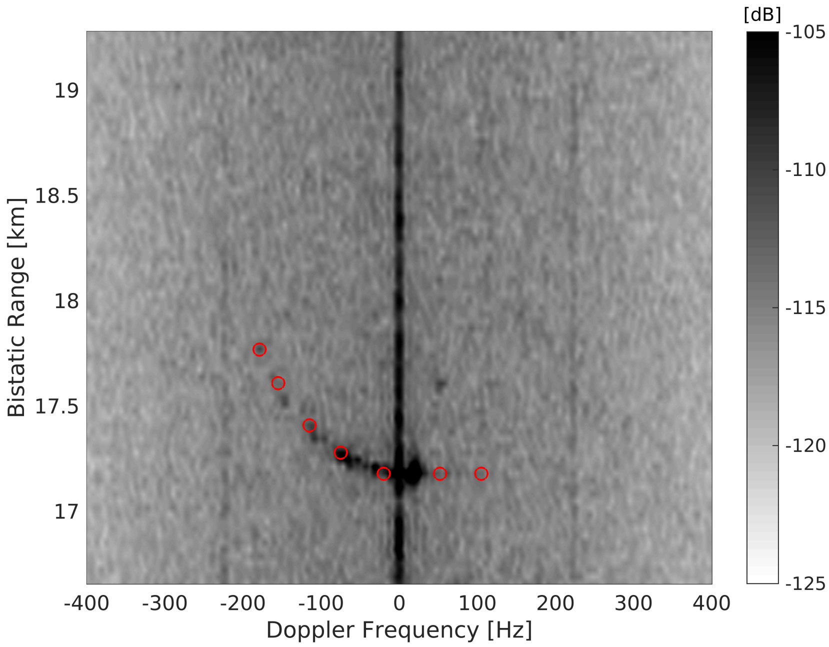

FIGURE 4.23: Real-data RDD results for a noisy reference signal with $SNR_r = 3.8$ dB and $T_{CPI} = 0.1$ s.

To reduce the impact of the reference signal noise, we perform a conventional reconstruction and an optimum one; figures 4.24 and 4.25 present the results. We notice that the conventional reconstruction has reduced the noise-floor level by around 5 dB, and that the optimum reconstruction achieved a noise-floor level reduction of more than 10 dB. Consequently, the the airplane track is easily distinguishable for the case of the optimally reconstructed reference signal.

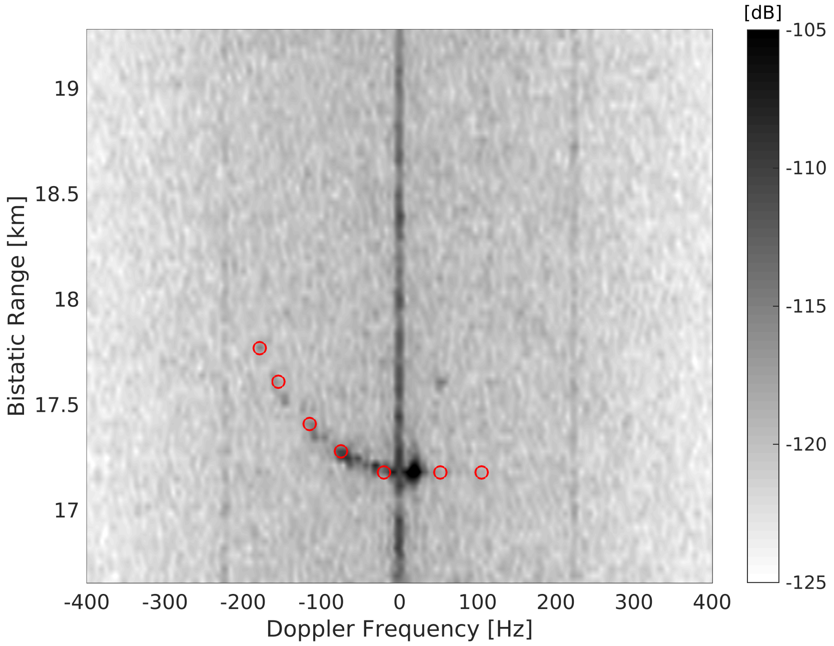

FIGURE 4.24: Real-data RDD results for a conventionally reconstructed reference signal with an initial $\mathrm{SNR_r} = 3.8$ dB and $T_{\mathrm{CPI}} = 0.1\ s$.

4.5.2.3 Detection probability improvement

In order to present the detection probability improvement due to the proposed reconstruction method, we calculate the detection probability as a function of $\mathrm{SNR_r}$ and we perform Monte-Carlo simulations (10^6 trials), for a target echo with $\mathrm{SNR_s} = -32$ dB, an integration interval of length $N = 10^5$, and a false alarm probability of $\mathrm{P_{FA}} = 10^{-4}$. The detection probability results are presented in figure 4.26. We notice a perfect match between the theoretical results (TH) and the MC results, which validates the retrieved expressions. In addition, we remark that the optimum reconstruction method outperforms the conventional method. The former achieves a detection probability at least equal to that for the pilot-only signal detection.

To demonstrate the optimality of the calculated filter weight, we calculate the detection probability as a function of the filter weight g_d for $\mathrm{SNR_r} = -10$ dB, $\mathrm{SNR_s} = -35$ dB, $N = 10^5$, and $\mathrm{P_{FA}} = 10^{-4}$; the results are presented in figure 4.27. In this scenario, the optimum filter weight is $g_d = 1 - \mathrm{P_e} \approx 0.2$, which is exactly the filter weight that maximizes the detection probability.

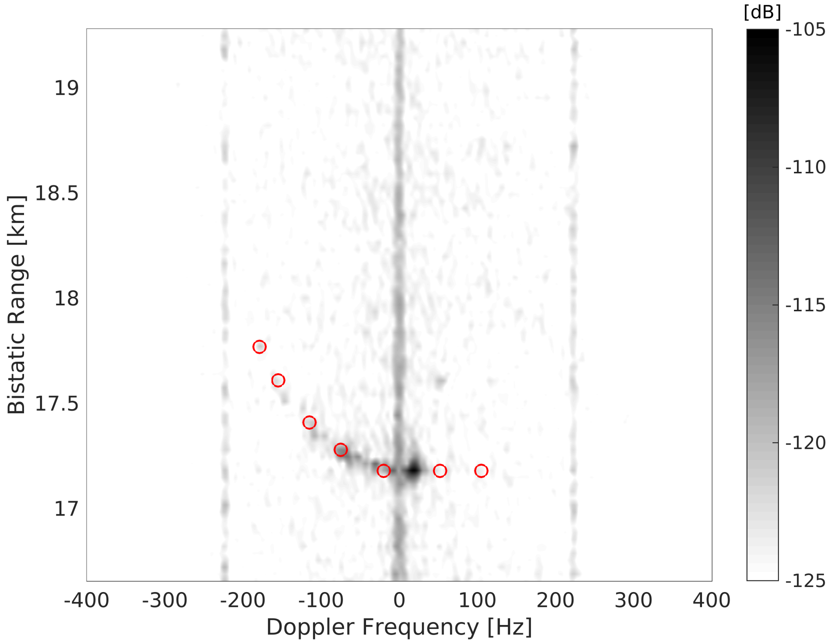

FIGURE 4.25: Real-data RDD results for a optimally reconstructed reference signal with an initial $\mathrm{SNR_r} = 3.8$ dB and $T_{\mathrm{CPI}} = 0.1\ s$.

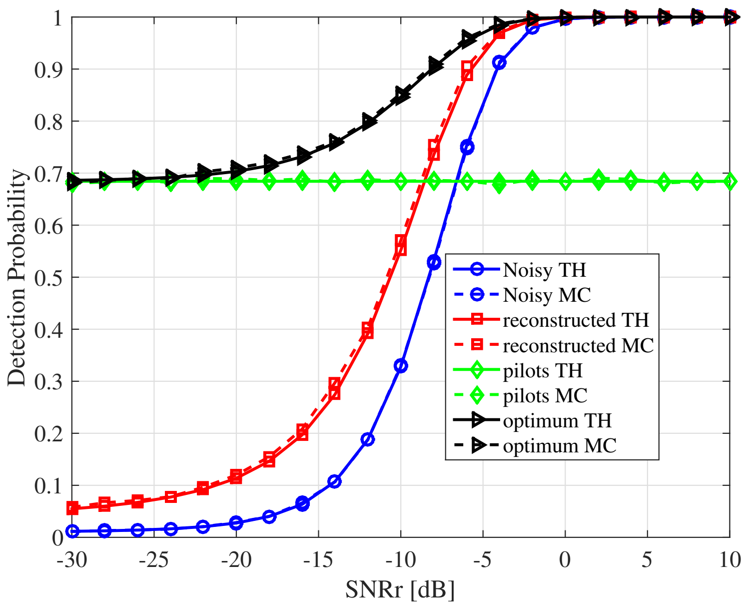

FIGURE 4.26: Detection probability as a function of $\mathrm{SNR_r}$ for $\mathrm{SNR_s} = -32$ dB, $N = 10^5$, and $\mathrm{P_{FA}} = 10^{-4}$.

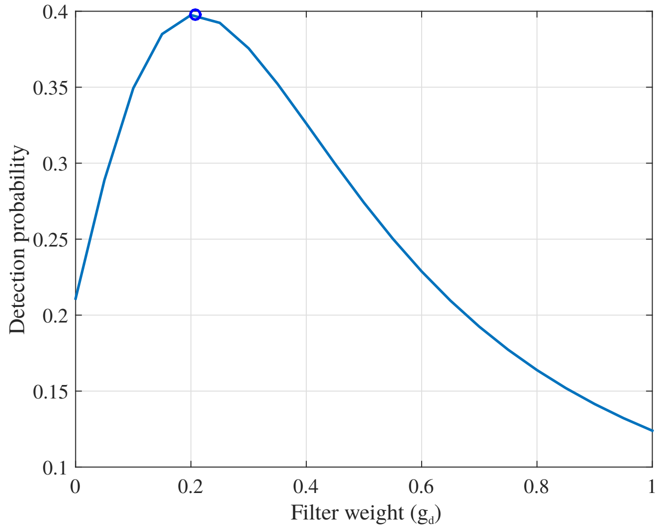

FIGURE 4.27: Detection probability as a function of the data symbol filtering weight for $\mathrm{SNR_r} = -10$ dB, $\mathrm{SNR_s} = -35$ dB, $N = 10^5$, and $\mathrm{P_{FA}} = 10^{-4}$.

To assess the behavior of the proposed method for different scenarios, we calculate the detection probability as a function of $\mathrm{SNR_r}$ and $\mathrm{SNR_s}$. Figure 4.28 presents the detection probability results for $N = 10^5$ and $\mathrm{P_{FA}} = 10^{-4}$. For $\mathrm{SNR_r} > 0$ dB, the conventional reconstruction and the optimum one provide approximately the same detection probability results. This is due to the negligible impact of the reconstruction error. For $\mathrm{SNR_r} < 0$ dB, the optimum reconstruction method significantly outperforms the conventional reconstruction method. These results can be explained by the optimum control of the data signal contribution, which reduces the reconstruction MSE and thus reduces the noise-floor level of the detector output. Therefore, the proposed method for reference signal reconstruction in DVB-T based PCL radars maximizes the detection probability by reducing the reconstruction mismatch, which extends the feasibility of the reference signal reconstruction approach for low $\mathrm{SNR_r}$.

4.6 Conclusion

In this chapter, we investigated the impact of the reference signal noise on the detection performances, we assessed the detection enhancement related to the reference signal reconstruction and the use of a pilot signal, and we proposed an optimum reconstruction method. We found that the reference signal noise acts by increasing the noise-floor level of the detection filter output, which buries low-magnitude targets and thus degrades the detection probability.

To reduce the impact of the reference signal noise in DVB-T based PCL radars, the signal reconstruction approach can be adopted. The reconstruction method is performed by decoding

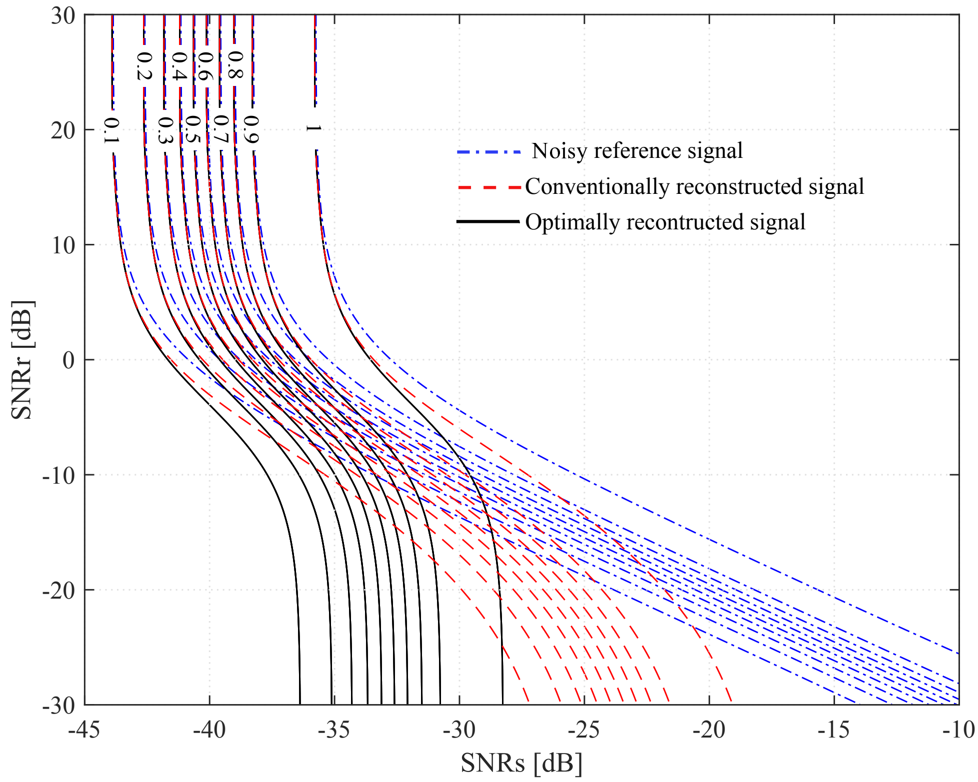

FIGURE 4.28: Detection probability as a function of $\mathrm{SNR_r}$ and $\mathrm{SNR_s}$, for $N = 10^5$ and $\mathrm{P_{FA}} = 10^{-4}$.

the received reference signal to recover the transmitted QAM symbols, and employ them to generate a noise-free signal. The reference signal reconstruction method is easy to implement and efficient as long as the reference signal SNR allows an accurate QAM symbol detection.

For low $\mathrm{SNR_r}$ values, the QAM symbols are detected with a significant error, which induces a mismatch between the reconstructed signal and the exact one, and thus, degrades the processing gain and the detection probability. For poor quality reference signals, we proposed to replace the received reference signal with a locally generated pilot signal. The use of a pilot signal for detection has shown its efficiency and superiority for low SNR values compared to the conventional signal reconstruction method. In addition, a significant cost reduction can be obtained by this method.

Obviously, the reconstructed reference signal involves a perfectly reconstructed pilot signal; thus, we proposed to optimally filter the detected symbols. This reduces the mismatch between the reconstructed signal and the exact one. The optimum reconstitution method extends the feasibility of the reference signal reconstitution method for DVB-T PCL radars. Consequently, relatively far illuminators of opportunity can be exploited (low SNR is expected), and the use of a single receiver architecture can be permitted (the reference signal will be received by the sidelobes of the antenna).

Chapter 5

Static clutter suppression methods

5.1 Introduction

Despite the numerous advantages of PCL radar systems, their silent operating mode is accompanied by two major issues. The first issue is the reference signal quality, which has been addressed in chapter 4. The second issue is the masking effects induced by the presence of the static clutter in the received surveillance signal. Unlike the simplified model of the surveillance signal adopted in chapter 4, a realistic model dictates the consideration of a direct-path and multipath components in the surveillance signal in addition to the target echoes. In fact, the direct-path signal forms the main part of the surveillance signal, and its magnitude is considerably larger than that of the target echo. The same remark, but with less significance, applies for the multipath components. This undesired presence degrades the detector dynamic range and can mask the target echoes [1]. Consequently, the reduction of the contribution of the static clutter (direct-path signal and multipath) is required to ensure an efficient operating PCL radar.

The direct-path and multipath reduction has been the subject of many research studies due to its importance, which results in several approaches. The first approach employs an adaptive antenna array to reduce the direct-path contribution, where a null is steered towards the transmitter direction [9, 11, 104, 105]. In the second approach, the terrain condition (mountains and buildings) are exploited to attenuate the direct-path signal [43, 106]. Unfortunately, these spatial filtering approaches increase the system cost and reduce its agility, which limits the passive radar main advantages (low cost and ease of deployment). In addition, the achieved null depth can be insufficient for the suppression requirements in PCL radar applications [107]. In the third approach, signal filtering methods are applied to filter-out the static clutter, these methods will be studied in this chapter.

In the literature, many filtering methods have been proposed to suppress the static clutter in the DVB-T based PCL radars. Among them, there are methods exploiting the correlation between the reference signal and the static clutter to estimate and suppress the latter, such as adaptive filters [12, 108, 109], the CLEAN algorithm [7, 110], and the extensive cancellation algorithm (ECA) [22]. Other clutter suppression methods exploit the structure of the DVB-T signal to estimate the propagation channel which reflects the clutter effect [54]. The performance of the cited methods has been studied considering a perfect reference signal, which is unrealistic. In this chapter, we investigate the impact of the reference signal noise on the clutter suppression methods, we assess the performance improvement due to the reference signal reconstruction, and we propose an efficient method for static clutter suppression.

Section 5.2 presents the impact of the static clutter on the detection performances. It first introduces the signal model of the surveillance signal considered in this chapter. Then, the major impacts caused by the static clutter are studied. It focuses on the following impacts: the noise-floor level increase, the dynamic range reduction, and the sidelobe masking effect.

In section 5.3, we present the adaptive filters employed for the static clutter suppression. We consider the least mean squares (LMS) algorithm and we assess its sensitivity to the reference signal noise. Next, we evaluate the improvement caused by the conventional reconstruction and the optimum one. Then, we address the limitations of the adaptive methods.

Section 5.4 discusses the sequential methods for clutter suppression such as CLEAN and ECA algorithms. It evaluates the impact of the reference signal quality on the achieved performance, and it presents the signal reconstruction consequences.

In section 5.5, the static clutter suppression methods based on the channel estimation are discussed and an improved method for channel estimation is proposed. Then, a comparison of the studied methods for clutter suppression is performed.

5.2 Static clutter impact

In this section, we introduce the signal model for the current chapter and we emphasis the considered assumptions about the received signal. Then, we assess the impact of the static clutter on the detection performance which can be limited into the dynamic range reduction, the noise-floor increase, and the sidelobe masking.

5.2.1 Signal model

For the reference signal model, we consider the model employed in chapter 4 where the reference signal is formed by a direct-path signal and a thermal noise. For the surveillance signal, we consider a realistic model unlike the previous chapter where the surveillance signal model was simplified to exclusively include the target echo and a thermal noise. The considered model takes into account the contribution of the direct-path signal and the multipath components. The surveillance signal $x_s(n)$ is expressed as follows [12]

$$\begin{cases} \mathrm{H}_0 : \; x_s(n) = \sum_{l=0}^{L-1} h_l s(n-\kappa_l) + w(n), \\ \\ \mathrm{H}_1 : \; x_s(n) = \sum_{l=0}^{L-1} h_l s(n-\kappa_l) + \alpha s(n-\kappa) e^{j2\pi f_d n} + w(n). \end{cases} \tag{5.1}$$

The clutter-to-noise ratio (CNR) and the target signal-to-noise ratio ($\mathrm{SNR_s}$) are defined in a similar manner as in equations (2.13) and (2.14).

5.2.2 Dynamic range and noise-floor level

The static clutter is principally formed by the direct-path signal and the reflections from the static scatterers located in the surveillance zone. The direct-path signal can be considerably larger than the target echo [12, 111], which results in a significant degradation of the detector dynamic range [1, 112]. Consequently, weak target echoes can be missed in the presence of the direct-path signal.

The masking effect of the static clutter manifests also in the increase of the noise-floor level as presented in figure 5.1 where one target is simulated for two CNR values. We notice that the increase of the CNR is accompanied by the increase of the noise-floor level, which may bury weak targets and thus degrades the detection probability.

5.2.3 Sidelobe masking effect

As seen in chapter 3, the ambiguity function of the DVB-T signal exhibits sidelobes in the frequency domain. The first sidelobe is 13 dB lower than the main lobe, and the following ones are with lower magnitudes. Thus, low velocity targets (i.e. low Doppler shift) can be masked by the static clutter sidelobes [107, 113]. Figure 5.2 presents simulation results for one target with 100 Hz Doppler shift in two CNR scenarios. We notice that the increase of the static clutter level induced the masking of the target echo by the sidelobes.

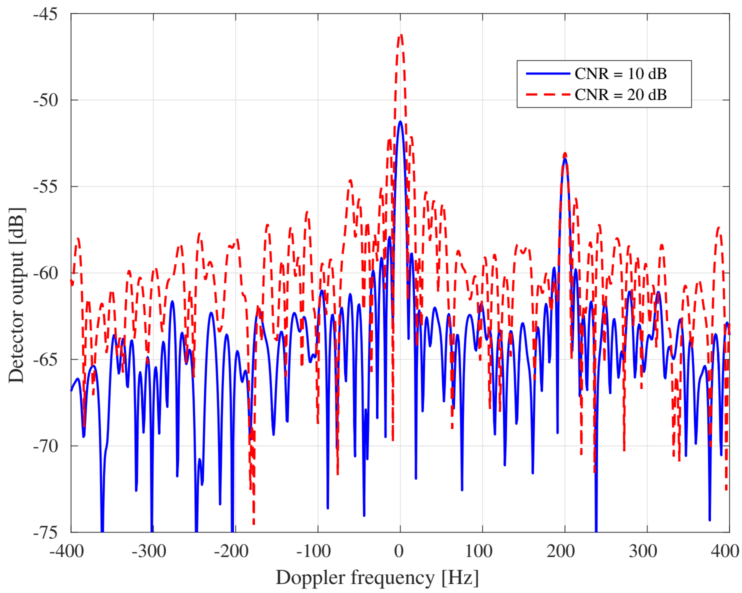

FIGURE 5.1: Noise-floor level increase due to the static clutter for one target with $\mathrm{SNR_s} = -20$ dB, $N = 10^6$, and $f_d = 200$ Hz.

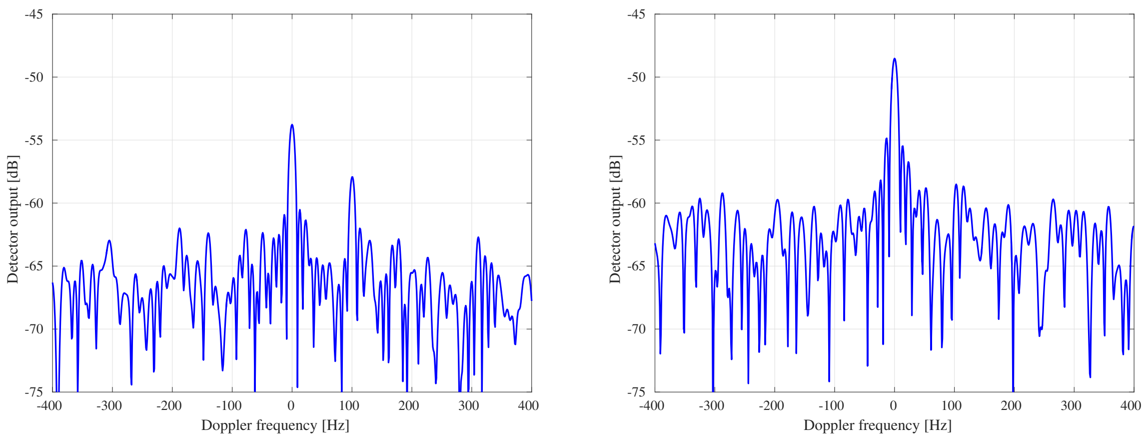

(A) CNR = 5 dB.

(B) CNR = 15 dB.

FIGURE 5.2: Sidelobe masking effect caused by the static clutter for one target with $\mathrm{SNR_s} = -30$ dB, $N = 10^6$, and $f_d = 100$ Hz.

The significant impact of the static clutter must be reduced, this can be done through the filtering of the received surveillance signal which will improve the detection performance and reduce the masking effect. The remainder of the chapter is dedicated to the assessment of a variety of static clutter suppression methods applied on DVB-T signals.

5.3 Adaptive methods

In the current section, the static clutter suppression methods based on the adaptive filter theory are addressed. It first presents their principle and structure. Next, their sensitivity to the reference signal noise is studied. Then, the impact of the reference signal reconstruction is presented.

5.3.1 Principle

The considered model of the static clutter in equation (5.1) is a weighted sum of time-delayed replicas of the transmitted signal, which is similar to the finite impulse filter (FIR) structure. Therefore, it is possible to suppress the static clutter from the surveillance signal employing adaptive filters. The adaptive filter structure requires two inputs: a primary input and a reference one [114]. Figure 5.3 presents the general principle of the static clutter adaptive cancellation. The surveillance signal is inputted as the desired signal (primary input) and the reference signal feeds the reference input. The adaptive filter weights are adjusted to match with the static clutter gains h_l, which results in an estimation of the static clutter signal. The estimated clutter signal is subtracted form the received surveillance signal, which provides a clutter-free signal. The adaptive cancellation does not require a prior knowledge of the signal characteristic and its structure is simple, which promoted its use for many PCL radar systems [12, 95, 107–109, 115–119].

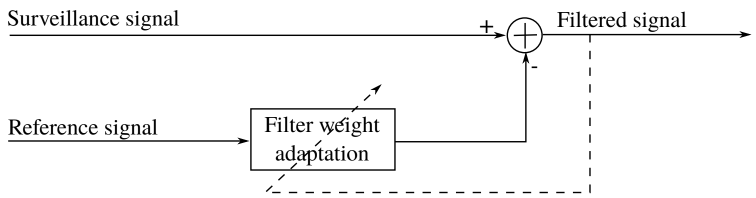

Figure 5.3: Adaptive static clutter cancellation.

Many variants of adaptive filter algorithms have been employed for static clutter suppression; we cite for example the least mean square (LMS) algorithm, the recursive least square (RLS) algorithm, and Wiener algorithm. This algorithm family minimizes the mean-square error between the estimated weights and the exact ones [103]. It is important to note that the filtering accuracy depends on the correlation between the reference signal and the static clutter components, in other words, a reference signal with high quality and stationary clutter weights are required for an efficient suppression [107]. In contrast, the target echoes are less correlated with the reference signal due to the Doppler shift, which reduces the filter impact on the desired signals.

5.3.2 Impact of the reference signal noise

The evaluation of the adaptive filters for static clutter suppression has been widely addressed in the literature [109, 118], where the comparison criteria were the direct-path attenuation capability, the noise-floor reduction, the processing cost, and the impact on the target echoes. These evaluation studies have considered a perfect reference signal, which is far from the realistic scenarios. In this section, we limit the study to the LMS algorithm and we investigate the impact of the reference signal quality on the performance of the static clutter suppression. In order to do so, we assess the direct-path (DP) signal attenuation when a noisy reference signal is employed.

Figure 5.4 presents the DP attenuation level as a function of the signal-to-noise ratio of the reference signal $\mathrm{SNR_r}$. The DP attenuation level is calculated as the difference between the initial power (before LMS filtering) and the residual power (after LMS) of the DP. Clearly, the static clutter suppression employing the LMS filtering method is affected by the reference signal quality. Further, we notice that an efficient DP removal requires a high $\mathrm{SNR_r}$ level ($\mathrm{SNR_r} \geq 25$ dB); and a low $\mathrm{SNR_r}$ significantly degrades the suppression performance. To investigate the performance degradation of the LMS suppression method, we present in figure 5.5 the evolution of the filter weight estimate for three $\mathrm{SNR_r}$ values. The shown results corresponds to the first tap weight (corresponds to the direct-path signal), which we set as $h_0 = 1$ in equation (5.1). Obviously, the $\mathrm{SNR_r}$ level affects the convergence value of the weight estimate; the lower the $\mathrm{SNR_r}$ level, the higher the convergence error. The weight estimation error induces a residual clutter signal, which reduces the suppression performance.

5.3.3 Impact of the reference signal reconstruction

As presented in chapter 4, PCL radars employing DVB-T signals can benefit form an enhancement of the reference signal quality by reconstructing the received signal. And we have proposed an optimum reconstruction method which outperforms the conventional approach in terms of the achieved detection probability. Here, we intend to assess the impact of the reference signal reconstruction (conventional and optimum methods) on the static clutter suppression employing an LMS filter. Figure 5.6 presents the evolution of the first tap estimate for two $\mathrm{SNR_r}$ scenarios and with three reference signal variants: noisy signal, conventionally reconstructed signal, and optimally reconstructed signal. Firstly, we notice that the signal reconstruction (conventional and optimum) clearly reduces the weight estimation error, which is another advantage of the signal reconstruction approach. Secondly, the optimally reconstructed reference signal outperforms the conventionally reconstructed signal for the estimation error reduction,

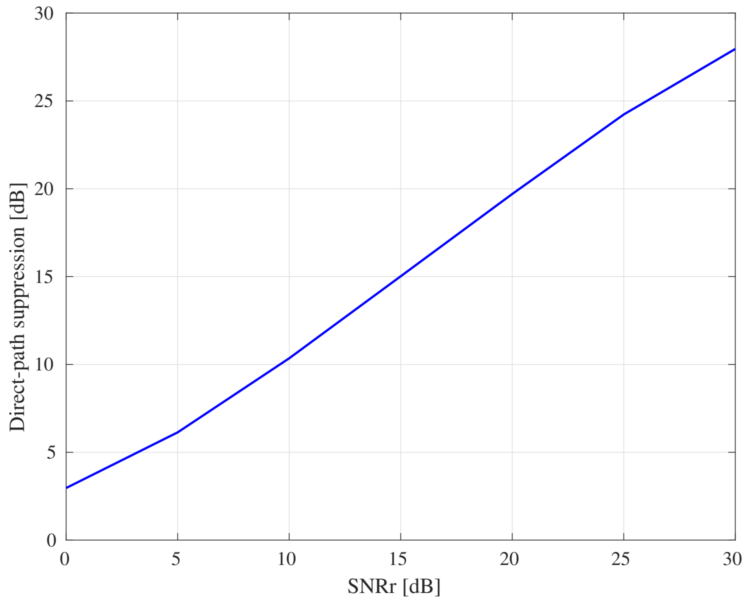

FIGURE 5.4: Direct-path signal attenuation as a function of the reference signal quality for LMS method.

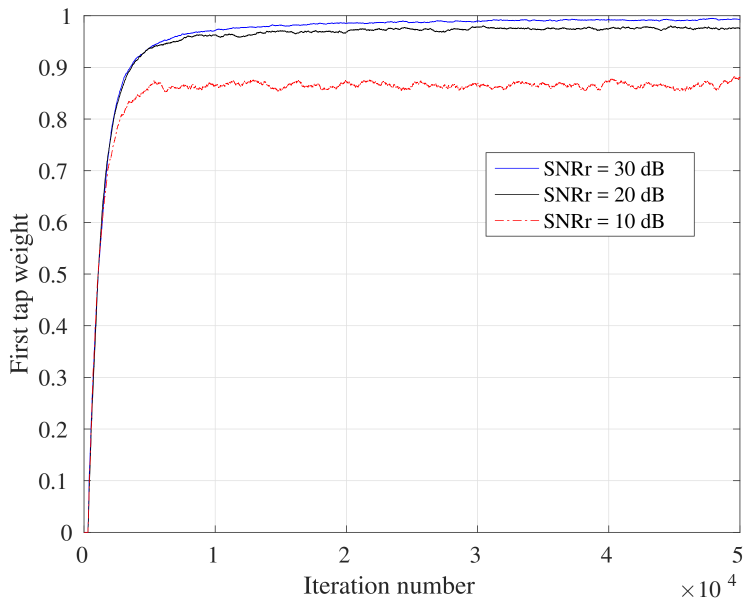

FIGURE 5.5: LMS convergence error.

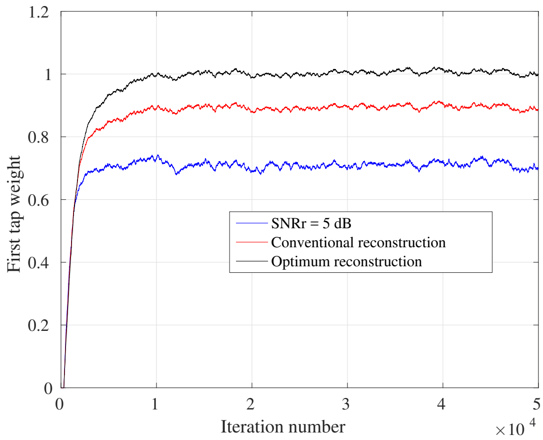

(A) $\mathrm{SNR_r} = 5$ dB.

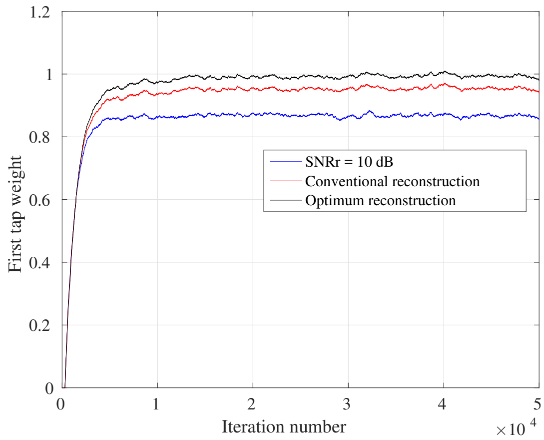

(B) $\mathrm{SNR_r} = 10$ dB.

FIGURE 5.6: Impact of the reference signal reconstruction on the LMS convergence.

which demonstrates the efficiency of the proposed reconstruction method in the static clutter suppression enhancement.

We define the normalized mean square error (NMSE) for the l^{th} static clutter component as follows

$$\mathrm{NMSE}(l) = \frac{\mathrm{E}\left[|h_l - \hat{h}_l|^2\right]}{\mathrm{E}\left[|h_l|^2\right]} \tag{5.2}$$

where h_l is the exact weight and $\hat{h}_l$ is the estimated one. Figure 5.7 shows the normalized mean square error of the LMS filter weight estimation as a function of the reference signal quality. Again, we notice the impact of the reference signal quality on the accuracy of the clutter weight estimation, and the improvement resulting from the signal reconstruction. In addition, the optimum reconstruction method is providing the minimal error value compared to the conventional method.

The reference signal reconstruction provides a less-noisy reference signal, which increases the correlation between the static clutter components and the reference input. And thus, reduces the estimation error and improves the suppression capability.

5.3.4 Limitations

The application of the adaptive filtering algorithms for the static clutter suppression can provide sufficient performances in PCL radars. However, they imply a relatively high computational load, which increases the system complexity and reduces the real-time operating capability. Further, the stability issues are often evoked together with the choice of the algorithm step-size. Furthermore, the previous section demonstrated their sensitivity to the reference signal noise,

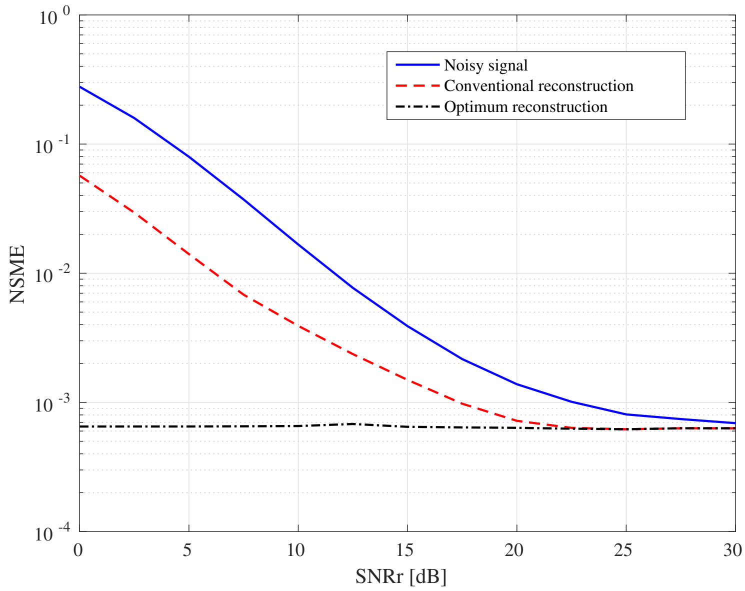

FIGURE 5.7: Normalized mean square error for LMS filter as a function of the reference signal noise.

which may result in a significant estimation error. Another limitation is that adaptive filters can only deal with zero-Doppler clutter components, thus, it has no ability to reject low-Doppler clutter [120] or strong target echoes [22].

5.4 Sequential methods

5.4.1 Principle

As explained in the previous section, the adaptive filtering methods applied for the clutter suppression are sensitive to the reference signal noise, and fail to reject low-Doppler clutter components and strong target masking effects. Other methods have been considered in the literature to deal with this issue; they are called sequential or multistage methods [7, 22, 110, 113, 121]. A sequential approach for the clutter suppression progressively detects and suppresses the undesired components of the received surveillance signal. It starts by eliminating the zero-Doppler clutter components. Next, it detects and suppresses the remaining near-zero-Doppler clutter components. Then, the strong targets are detected and their contribution in the surveillance signal is suppressed, which enables the detection of low magnitude targets. The sequential methods are executed for many iterations until a stopping criterion is reached.

The most popular sequential methods applied for clutter suppression in PCL radars are the CLEAN algorithm [7, 110, 121] and the extensive cancellation algorithm (ECA) [22, 113]. The

CLEAN algorithm acts by detecting the dominant component of the surveillance signal, generating replicas corresponding to the detected component, and subtracting it from the surveillance signal. This operation is repeated until a sufficient cleaning is achieved. The ECA algorithm is performed by projecting the surveillance signal in a subspace orthogonal to the clutter.

In this section, we consider the extensive cancellation algorithm and we assess its sensitivity to the reference signal noise. And we illustrate the resulting improvement from the reference signal reconstruction.

5.4.2 Extensive cancellation algorithm (ECA)

The extensive cancellation algorithm is based on the signal space projection technique [122]. It employs the least square approach to minimize the difference between the estimated clutter signal and the received surveillance signal [22], which is expressed as follows

$$\min_{\boldsymbol{\psi}}\{\|\mathbf{x}_{\mathrm{s}} - \mathbf{A}\boldsymbol{\psi}\|\}, \tag{5.3}$$

where $\mathbf{x}_{\mathrm{s}}$ is the surveillance signal of size $N \times 1$, and $\mathbf{A}$ is the matrix given by

$$\mathbf{A} = \mathbf{B}\left[\boldsymbol{\Lambda}_{-p}\mathbf{S}_{\mathrm{r}}, \dots, \boldsymbol{\Lambda}_{-1}\mathbf{S}_{\mathrm{r}}, \mathbf{S}_{\mathrm{r}}, \boldsymbol{\Lambda}_{1}\mathbf{S}_{\mathrm{r}}, \dots, \boldsymbol{\Lambda}_{p}\mathbf{S}_{\mathrm{r}}\right], \tag{5.4}$$

where $\mathbf{B}$ is an incidence matrix which selects the last N rows of the following matrix, $\boldsymbol{\Lambda}_p$ is a diagonal matrix applying the phase shift corresponding to the p^{th} Doppler value, and the matrix $\mathbf{S}_{\mathrm{r}}$ is formed as follows

$$\mathbf{S}_{\mathrm{r}} = \left[\mathbf{x}_{\mathrm{r}}, \mathbf{D}\mathbf{x}_{\mathrm{r}}, \mathbf{D}^2\mathbf{x}_{\mathrm{r}}, \dots, \mathbf{D}^{K_r-1}\mathbf{x}_{\mathrm{r}}\right], \tag{5.5}$$

where $\mathbf{x}_{\mathrm{r}}$ is the received reference signal of size $N \times 1$, the matrix $\mathbf{D}$ is a matrix that applies a delay of a single sample, and K_r is the number of the considered range bins. Note that the size of the matrix $\mathbf{A}$ depends on the number of the signal samples, the number of range bins, and the number of Doppler frequencies to be rejected $(2p + 1)$.

The LS solution of the minimization problem is (5.3) is given by

$$\hat{\boldsymbol{\psi}} = \left(\mathbf{A}^H\mathbf{A}\right)^{-1}\mathbf{A}^H\mathbf{x}_{\mathrm{s}}, \tag{5.6}$$

and the filtered surveillance signal is retrieved as follows

$$\mathbf{x}_{\mathrm{ECA}} = \mathbf{x}_{\mathrm{s}} - \mathbf{A}\hat{\boldsymbol{\psi}}. \tag{5.7}$$

Here, we intend to assess the sensitivity of the ECA clutter rejection method to the reference signal noise. In order to do so, we consider the direct-path attenuation level as a metric. The retrievals can be generalized on the rest of the clutter components since they are just delayed, shifted, and attenuated copies of the direct-path signal.

Figure 5.8 presents zero-range cut of the range-Doppler diagram for ECA filtered signals for different SNR_r values. We notice that the notch depth around the zero frequency axis, which reflects the suppression efficiency, depends on the reference signal quality; the lower the SNR_r value, the worst the DP attenuation. For a clearer insight about the ECA sensitivity to the reference signal noise, we calculate the direct-path attenuation level as a function of SNR_r; the results are presented in figure 5.9. Again, we notice that an efficient ECA operation requires a clean reference signal, which illustrates the ECA sensitivity towards the reference signal noise.

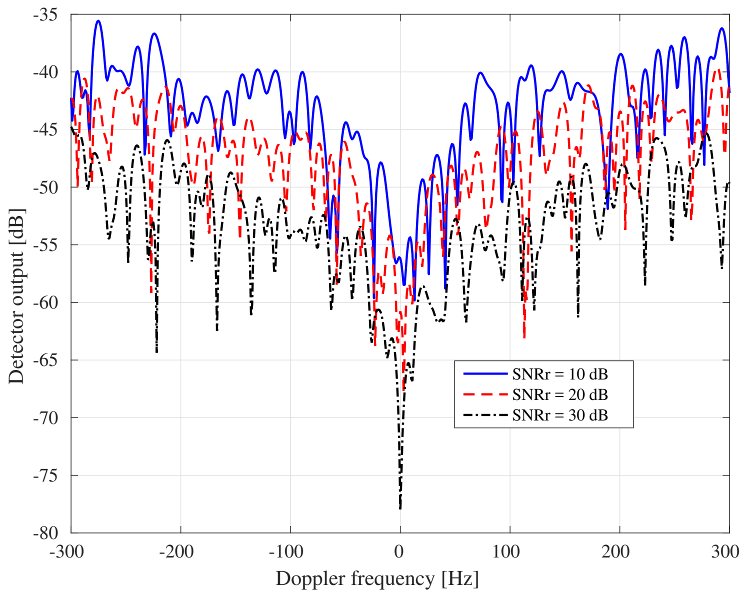

FIGURE 5.8: Impact of the reference signal noise on the ECA static clutter suppression.

To evaluate the impact of the reference signal reconstruction on the ECA suppression performance, we evaluate the NMSE of the estimate of the DP weight h_0 as a function of the SNR_r. Three reference signal variants are compared: noisy signal, conventionally reconstructed signal, and optimally reconstructed one. Figure 5.10 presents the resulting NMSE values. We notice that both conventional and optimum signal reconstruction methods improve the estimation of the clutter weights. However, the optimum reconstruction method provides better performance for $\text{SNR}_\text{r} < 25$ dB scenarios. For $\text{SNR}_\text{r} > 25$ dB, both reconstruction methods provide the same performance since the signal is perfectly reconstructed (the QAM estimation error is negligible).

Hence, we showed that the optimum reference signal reconstruction improves the static clutter suppression better that the conventional reconstruction. This is due to the optimum control of

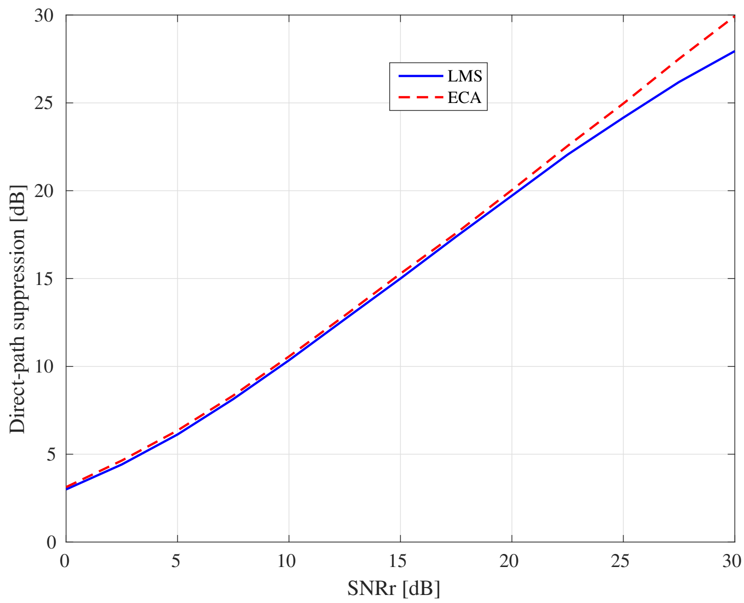

FIGURE 5.9: Direct-path signal suppression through ECA as a function of the reference signal SNR.

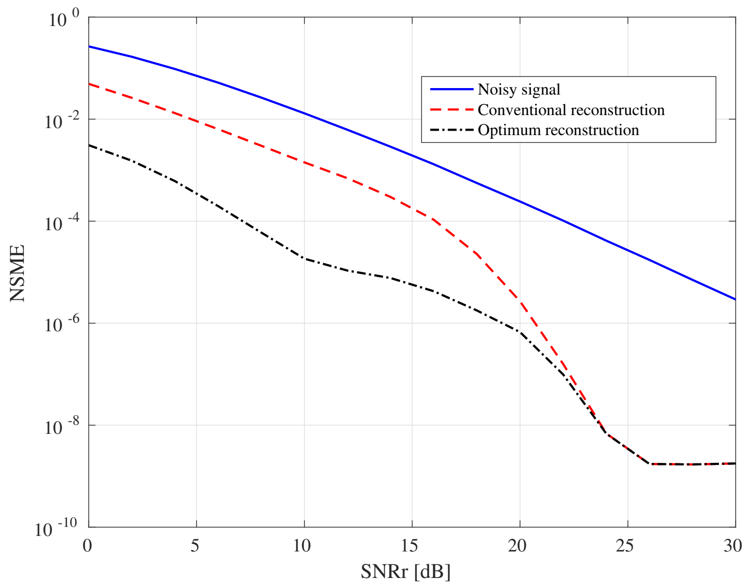

FIGURE 5.10: NMSE of the estimated DP weight h_0 for different reference signal reconstruction methods.

the data signal contribution, while the conventional method includes the entire estimated data signal which may form a noise source and reduces the correlation with the clutter components.

5.4.3 Limitations

Despite the suppression efficiency of the sequential methods, the induced computation load is high particularly the matrix inversion stage (see equation 5.6). For example, the nominal coherent processing interval is $T_{\mathrm{CPI}} = 0.1\ s$ for the DVB-T based passive radars, which is equivalent to about $N = 10^6$ samples. Thus, the inversion of an $N \times N$ matrix is required to perform the ECA. Obviously, the inversion of an $N \times N$ matrix is computationally intensive, and even with the improved version ECA-B [22] where the signal is divided into batches, the calculation load remains relatively high. Consequently, its application for real-time systems can be very challenging.

Both adaptive and sequential methods require enormous calculation resources, which rises the system cost and increases its complexity. In addition, when applied on DVB-T based PCL radars, these clutter suppression methods do not exploit the DVB-T signal characteristics. Exploiting the DVB-T signal structure may reduce the computation cost of the static clutter suppression, and provides better performances.

5.5 Static clutter suppression in the frequency domain

5.5.1 Principle

The DVB-T signal structure has allowed specific processing methods to enhance the reference signal quality. Similarly, several static clutter suppression methods have exploited the DVB-T signal structure. In this section, we consider two methods: the extensive cancellation algorithm by carriers (ECA-C) [53, 120] and the channel estimation method [54, 55]. These methods perform the static clutter suppression in the frequency domain. In order to do so, they require an estimate of the transmitted symbols and the frequency-domain components of the surveillance signal. The transmitted symbol estimates, $\tilde{\mathbf{c}}$, are obtained by demodulating the reference signal. We assume that the surveillance signal, $x_s(n)$, is time and frequency synchronized. Hence, its frequency-domain component for the i^{th} DVB-T symbol and the k^{th} subcarrier can be expressed as follows

$$\tilde{X}_s(i,k) = H(i,k)\, c_{i,k} \; + X_t(i,k) + W(i,k), \tag{5.8}$$

where $X_t(i,k)$ is the target echo contribution and W is the FFT of the noise $w(n)$. If we assume that the propagation channel is invariant during the coherent processing interval, we can write

$$\tilde{X}_s(i,k) = H(k)\, c_{i,k} \; + X_t(i,k) + W(i,k). \tag{5.9}$$

5.5.1.1 Extensive cancellation algorithm by carriers (ECA-C)

The ECA-C algorithm [53] is an optimization of the original ECA algorithm [22, 113] applied for clutter suppression in PCL radars employing OFDM waveforms such as DVB-T and DAB. The ECA-C offers a reduced computational load compared to the ECA; it performs the clutter suppression in the frequency domain and operates carrier by carrier. The ECA-C algorithm follows the same steps as the ECA, however, it replaces the time-domain reference signal $\mathbf{x}_\mathrm{r}$ by the estimated symbols $\tilde{\mathbf{c}}$, and replaces the time-domain surveillance signal $\mathbf{x}_\mathrm{s}$ by the symbols $\tilde{X}_s(i,k)$. The filtered symbols are modulated to retrieve the time-domain clutter-free signal.

Since the ECA-C algorithm is exclusively effective for zero-Doppler clutter suppression, an improved version is proposed in [120] which enables the suppression of the low-Doppler clutter. This method is named enhanced cancellation algorithm by carrier and Doppler shift (ECA-CD). Although, the ECA-C method could reduce the computational cost of ECA method, the way of operating carrier by carrier is still time and resource consuming.

5.5.1.2 Channel estimation for static clutter suppression

The second method for the clutter suppression in the frequency domain is based on the estimation of the propagation channel of the surveillance signal [54, 55]. It exploits the possibility of estimating the propagation channel in DVB-T signals which is originally designed to equalize received data. The channel estimation is made possible thanks to the pilot subcarriers which are known at the receiver. The channel estimate, $\hat{\mathbf{H}}$, together with the estimates of the transmitted symbols, $\tilde{\mathbf{c}}$, are employed to form a synthetic clutter signal which is subtracted from the received surveillance signal, $\tilde{\mathbf{X}}_\mathbf{s}$, to obtain a clean signal.

This method is presented in figure 5.11. The propagation channel is estimated by the least square (LS) method detailed in chapter 3. For the i^{th} DVB-T symbol and the k^{th} subcarrier, the clutter-free result is obtained as follows

$$X_{filtered}(i,k) = \tilde{X}_s(i,k) - \hat{H}(k)\, \tilde{c}_{i,k}, \tag{5.10}$$

The time-domain filtered signal, $x_{filtered}(n)$, is obtained by modulating the resulting symbols $\mathbf{X}_\mathrm{filtered}$.

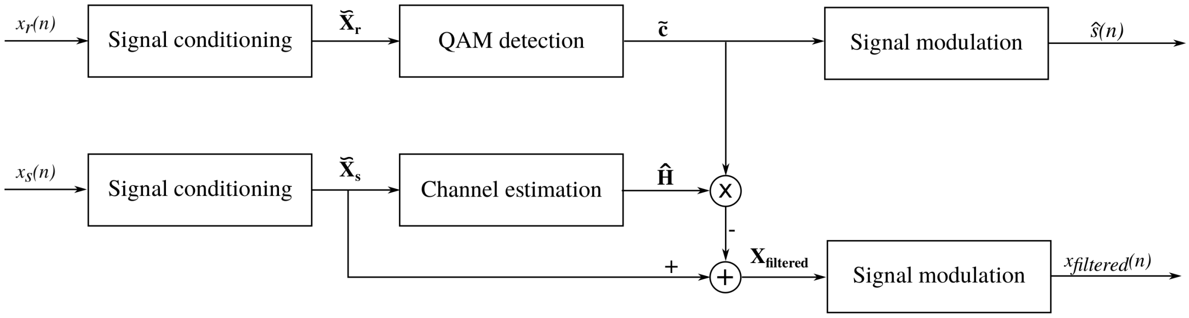

FIGURE 5.11: Static clutter suppression by channel estimation for DVB-T based PCL radars.

5.5.2 Improved channel estimation

The static clutter suppression employing the propagation channel requires an accurate propagation channel estimation. However, the channel estimation approach in the previous section induces interpolation errors since the full channel estimate is obtained by interpolating the pilot subcarrier responses which are spaced by 12 ΔF (ΔF is the subcarrier spacing). Consequently, the channel estimate error will result in residual clutter components. It follows that the reduction of the interpolation error will enhance the channel estimate accuracy and thus improves the static clutter suppression. In this section, we propose an improved channel estimation which reduces the interpolation error.

As was mentioned in chapter 3, the pilot pattern is 4 DVB-T symbol periodic, and each period is formed by four overlapping patterns. The interleaving of the four patterns reduces the interpolation gap from 12 ΔF to 3 ΔF, and thus reduces the interpolation errors. Therefore, we propose to calculate the averaged channel response for each pilot pattern (to reduce noise impact), interleave the four resulting channel estimates (to reduce the interpolation error), and interpolate the obtained channel response to get the full channel estimate.

Figure 5.12 presents the difference between the proposed method for channel estimation and the conventional LS method employed in [54]. The conventional LS method for channel estimation is executed symbol by symbol. For each DVB-T symbol, an estimate of the channel response at the pilot subcarriers is calculated and the full channel estimate is obtained by interpolation (linear interpolation in the figure). The average of the obtained channel estimates provides the final result. In contrast, the proposed method performs the interpolation after interleaving the four consecutive responses of the pilot patterns, which reduces the interpolation errors. Figure 5.13 presents a slice of the propagation channel and its estimate employing the conventional LS method and the estimate with the proposed method. Clearly, the proposed method provides better estimation accuracy of the propagation channel.

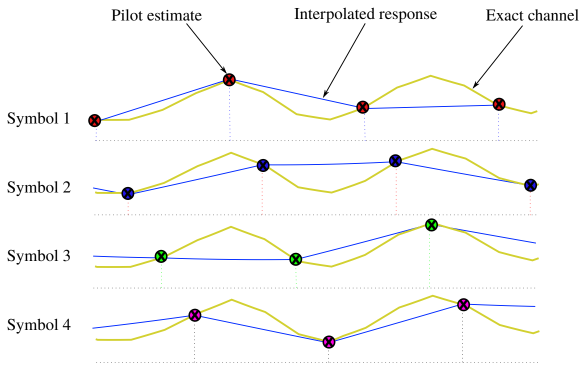

(A) Conventional LS estimation.

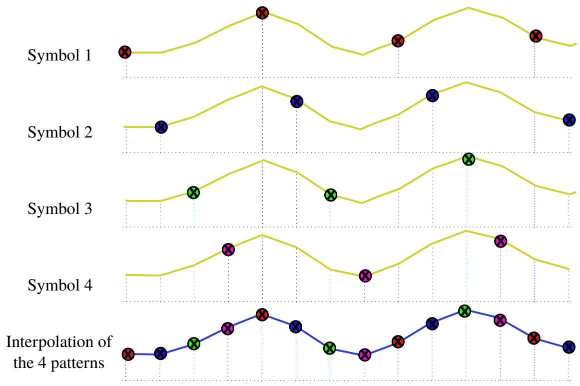

(B) Proposed LS estimation.

FIGURE 5.12: Propagation channel estimation for clutter suppression.

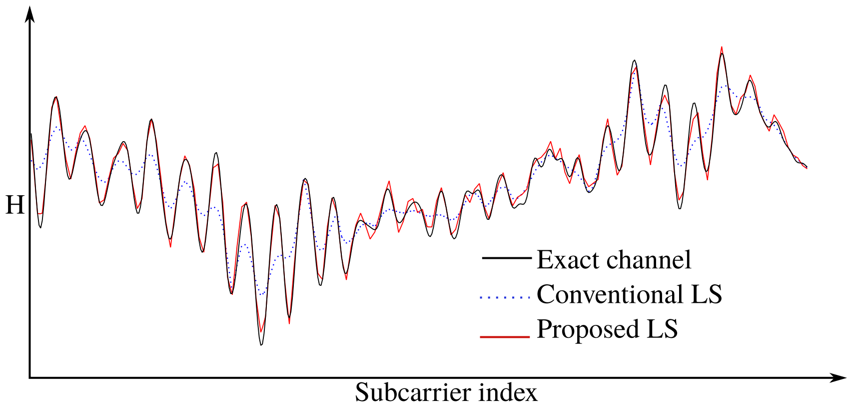

FIGURE 5.13: Comparison of the channel estimation accuracy between the conventional LS and the proposed LS.

In figure 5.14, we present the normalized mean square error (NMSE) of the channel estimation methods as a function of the clutter-to-noise ratio (CNR). We notice that the proposed method for channel estimation achieves lower NMSE than the method in [54]. This will result in a better estimation of the clutter signal and thus, an efficient static clutter suppression.

5.5.3 Comparison

To compare the studied methods for the clutter suppression, we propose to compare the direct-path attenuation level for the following methods: LMS filtering, ECA-C method, conventional channel estimate, and the improved channel estimate. The same reference signal quality (SNR_r) has been employed for all of the methods. Figure 5.15 presents a zero-range cut comparison of the cited methods. We notice that the residual DP for the LMS method is significant even after reference signal reconstruction. The LS channel method outperforms the LMS approach, and the improved channel estimation method provides approximately the same performance as the ECA-C.

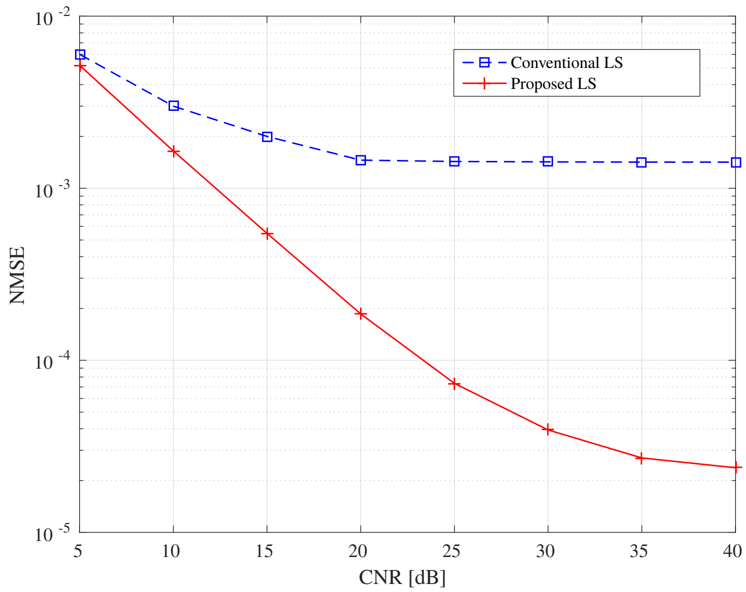

FIGURE 5.14: Comparison of the channel estimation NMSE between the conventional LS and the proposed LS.

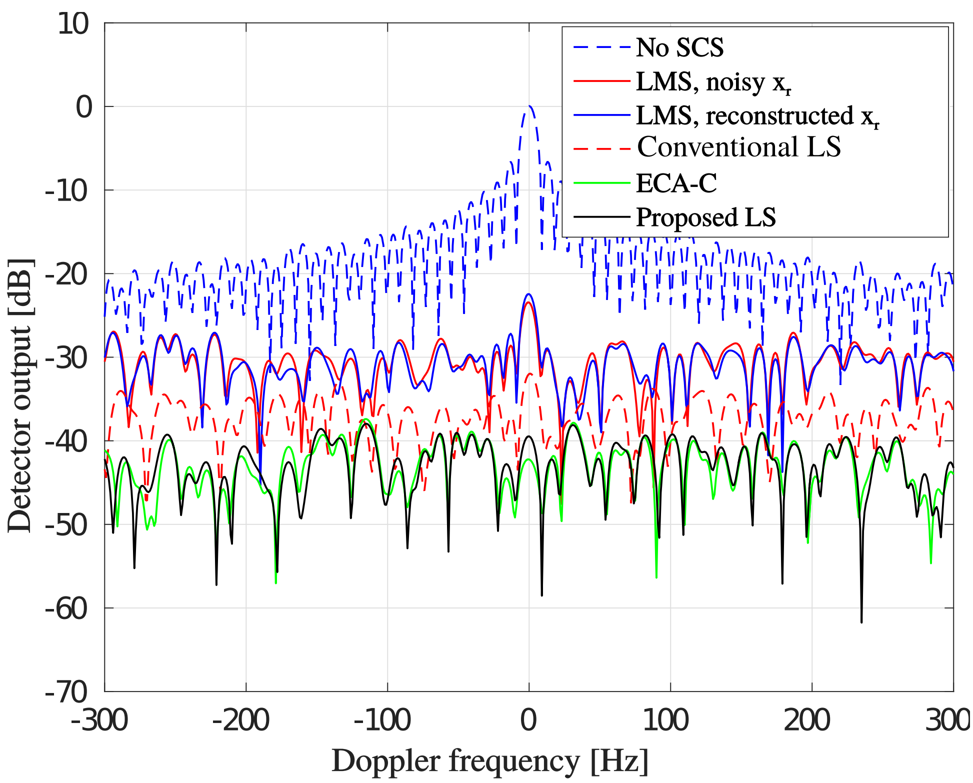

FIGURE 5.15: Comparison of the static clutter suppression (SCS) methods for direct-path attenuation.

To evaluate the impact of the studied static clutter suppression methods on real-data, we consider one measured data set of length 0.1 s where the target has a bistatic range of 2.6 km and a Doppler shift of -280 Hz. Figure 5.16 present the range-Doppler results for different processing methods. Figure 5.16a presents the resulting range-Doppler diagram for a non-filtered surveillance signal. We notice that the direct-path signal and the static clutter dominate the resulting diagram, which induced a high noise-floor level that masks the target echo. In figures 5.16b and 5.16c, the LMS and the conventional channel estimation [54] static clutter suppression methods were applied, respectively. The results clearly show the target position since the static clutter was significantly suppressed which resulted in a noise-floor reduction. Nevertheless, a residual static clutter can be noticed around the zero-Doppler axis, which is due to the limited performances of the two methods. Figures 5.16d and 5.16e present the results for the ECA-C approach and the the improved channel estimation approach, respectively. We remark that both methods performed an efficient static clutter suppression compared to the previous two methods, and that the results are approximately similar (the same remark as in figure 5.15).

It follows that the static clutter suppression methods in the frequency domain provide satisfactory results. In addition, these methods are less sensitive to the reference signal noise since they exploit the knowledge of the pilot subcarriers. Although the ECA-C method and the proposed method (based on an improved channel estimation) provide similar performances, the proposed method has a lower complexity since no matrix inversion operations are required. In fact, the prior knowledge about the pilot subcarriers gives an important advantage to channel estimation based method, which allows an accurate clutter estimation and suppression.

5.6 Conclusion

In this chapter, we provided an overview of the static clutter suppression methods for PCL radars. We showed that the presence of the static clutter in the surveillance signal reduces the dynamic range, increases the detector noise-floor level, and masks low-Doppler echoes by its sidelobes. To cope with these issues, many suppression methods have been proposed; we assessed the impact of the reference signal quality on those methods.

We found that the adaptive and sequential methods for static clutter suppression are remarkably sensitive to the reference signal noise, and that the reference signal reconstruction increases their efficiency. In addition, the performance improvement due to the optimum reconstruction outperforms the improvement due to the conventional one.

The frequency-domain clutter suppression methods exploit the DVB-T signal structure to reduce the inherent computation load, and to avoid the performance degradation due to the reference

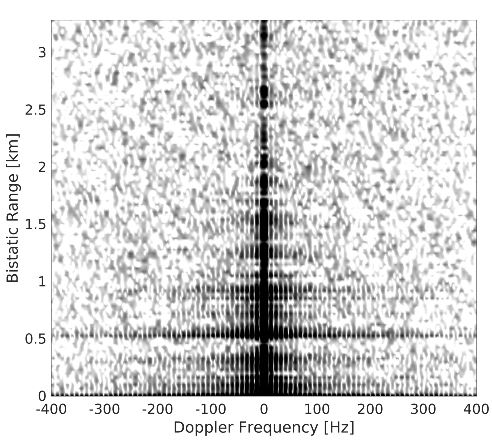

(A) No static clutter suppression.

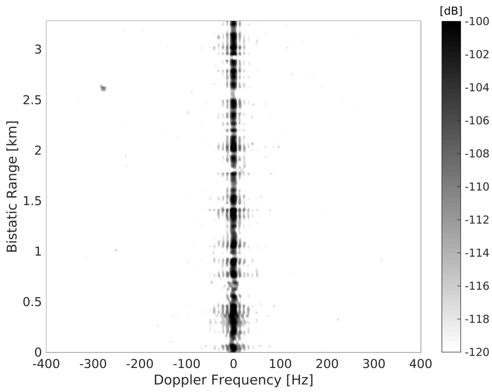

(B) LMS method.

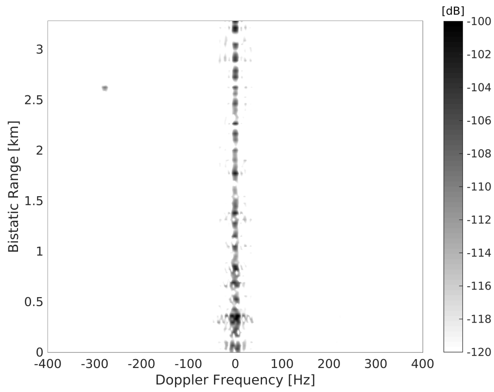

(C) Conventional channel estimation method.

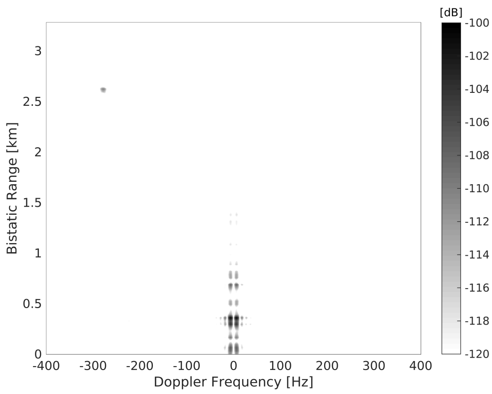

(D) ECA-C method.

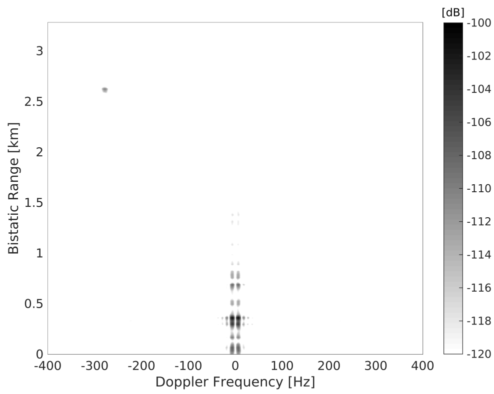

(E) Improved channel estimation method.

FIGURE 5.16: Comparison of the static clutter suppression methods applied on a real-data set of length 0.1 s and a target located at (2.6 km, −280 Hz).

signal noise. The proposed enhancement of the propagation channel leads to an efficient static clutter suppression with lower computation load.

As a result, we suggest to optimally reconstruct the reference signal to enhance the static clutter suppression if the adaptive or the sequential methods are employed. Otherwise, the use of the proposed channel estimate method is the most recommended due to its simple implementation and high performance.

Chapter 6

DVB-T PCL radars with a single-receiver

6.1 Introduction

As stated earlier, the DVB-T signal structure allows the reconstruction of the received reference signal to improve its signal-to-noise ratio. This reconstruction can be performed even for low SNR values thanks to the proposed optimum method in chapter 4. We showed also that the direct-path signal in the surveillance signal forms the most important part of the signal. Hence, one can exploit the DP signal to generate a synthetic reference signal, and thus a second receiver (dedicated to the reference signal) is unnecessary. Such approach is denoted single receiver PCL radar [123–125]. This approach simplifies the radar architecture and reduces its cost.

In the single receiver configuration, the direct-path signal is assumed to be significantly larger than the rest of the multipath components including the signals from other transmitters operating at the same frequency (SFN). This assumption will enable an accurate time and frequency synchronization of the received signal. The synchronized signal is then exploited to extract two signals: reference signal and target signal.

In this chapter, we consider a single receiver DVB-T PCL radar and we use an optimized processing scheme. It involves the optimum reference signal reconstruction, and the improved channel estimation which were presented earlier. As shown in chapter 4, the optimum reconstruction extends the feasibility of the reference signal reconstruction, which can be a required performance for the single receiver PCL radar. In addition, the improved channel estimation enhances symbol equalization and thus the quality of the reconstructed reference signal, what leads to an improved static clutter suppression. Monte-Carlo simulations will be used to assess the feasibility of this approach, and real-data results will be employed to illustrate its efficiency.

Section 6.2 presents the model of the received signal and defines the assumptions about its quality. In section 6.3, the proposed signal processing scheme is detailed. Section 6.4 assesses the performance of the proposed signal processing scheme by using simulation results. In section 6.5, real-data sets are employed to illustrate the efficiency of the proposed processing.

6.2 Signal model

Figure 6.1 illustrates the components of the received signal for a single receiver PCL radar. The received signal is the sum of a direct-path signal, static clutter components resulting from the reflections by the static scatterers in the surveillance area, a possible target echo, and the receiver thermal noise. We consider the following model for the received signal

$$x(n) = \sum_{l=0}^{L-1} h_l s(n-\kappa_l) + \alpha s(n-\kappa) e^{j2\pi f_d n} + v(n) \tag{6.1}$$

where L is the number of the considered static scatterers with reflection coefficients h_l. The target return is characterized by a time-delay of κ, a Doppler-shift of f_d, and a reflection coefficient α. The term $v(n)$ includes the receiver thermal noise and the interference source contributions, which is modeled as a Gaussian noise with zero mean and variance σ_v^2. We assume that the clutter parameters (h_l) and the target echo parameters (α, f_d, and κ) are invariant during the coherent processing interval. The coefficient h_0 refers to the direct-path signal component, hence we define the direct-path-to-noise ratio (DNR) as

$$\mathrm{DNR} = |h_0|^2 \sigma_s^2 / \sigma_v^2, \tag{6.2}$$

where σ_s^2 is the variance of the transmitted signal. Similarly, the target signal-to-noise ratio (SNR) is defined as follows

$$\mathrm{SNR} = |\alpha|^2 \sigma_s^2 / \sigma_v^2. \tag{6.3}$$

6.3 Signal processing scheme

As previously stated, the direct-path signal constitutes the main component of the received signal; it is assumed to be received via the antenna sidelobes. The antenna main lobe is directed towards the surveillance zone. Since the detection requires two signals (a reference signal and a

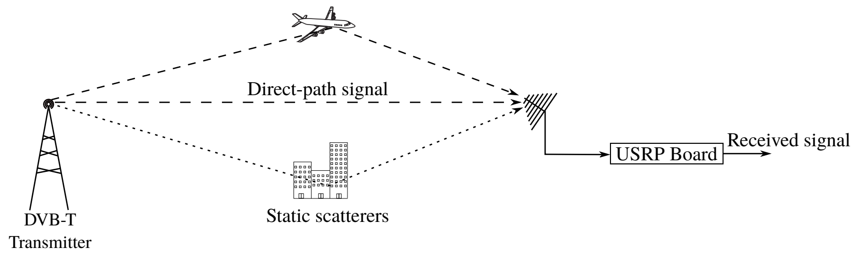

FIGURE 6.1: Received signal model for the single receiver radar.

surveillance signal), the signal processing intends to extract these two signals from the received signal.

Figure 6.2 presents the proposed signal processing scheme. The signal conditioning stage includes time and frequency synchronization operations for the received signal $x(n)$ and the FFT transformation of the synchronized signal. The resulting frequency-domain symbols $\tilde{\mathbf{X}}$ are first exploited to estimate the propagation channel. The equalization of the symbols $\tilde{\mathbf{X}}$ is performed using the channel estimate $\hat{\mathbf{H}}$. The equalized symbols, $\check{\mathbf{X}}$, are detected to provide an estimate of the transmitted symbols. The detected symbols $\tilde{\mathbf{c}}$ are optimally filtered according to the DNR value, which results in $\hat{\mathbf{c}}$. The optimally filtered symbols are modulated to provide a synthetic reference signal $\hat{s}(n)$. Together with the propagation channel estimate ($\hat{\mathbf{H}}$), the optimally filtered symbols ($\hat{\mathbf{c}}$) are employed to obtain an estimation of the static clutter signal. The frequency-domain target return is obtained by subtracting the static-clutter components from the frequency-domain symbols. The reminder of this section details the processing scheme of the received signal.

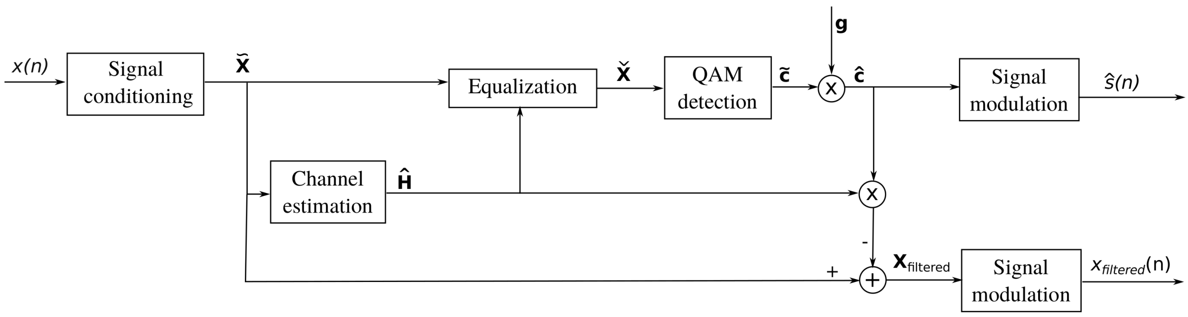

FIGURE 6.2: Processing scheme for reference signal recovery and static clutter suppression for single receiver PCL radar.

6.3.1 Signal conditioning

As presented earlier, the DVB-T signal demodulation is structure based, which requires an accurate synchronization to localize the beginning of each DVB-T symbol. In addition, the compensation of the carrier frequency offset (CFO) is needed to maintain the subcarrier orthogonality. The synchronization process applied for the single receiver PCL radar is identical to that presented in chapter 3. By considering that the direct-path signal as the dominant component of the received signal, the guard interval correlation is employed to define the DVB-T symbol blocks [66]. The CFO estimation is performed in two steps: the first one employs the guard interval correlation to estimate the fractional part of the CFO [66], and the second step uses the pilot subcarriers to estimate the integer part of the CFO [74]. The compensation of the CFO maintains the subcarrier orthogonality and thus reduces the QAM symbol detection error.

The synchronized received signal is divided into blocks of DVB-T symbol size. Next, the guard interval is removed from each DVB-T symbol. Then, the useful parts of the DVB-T symbols are Fourier-transformed, which provides the following result for each subcarrier

$$\tilde{X}(i,k) = H(k)c_{i,k} + X_t(i,k) + V(i,k), \tag{6.4}$$

where X_t is the target contribution and V is the the FFT transformation of $v(n)$.

6.3.2 Propagation channel estimation

In the classical architecture of bistatic PCL radars, the reference antenna is highly directive and it is steered towards the transmitter location. Consequently, the contribution of multipath and other transmitters in the received reference signal can be neglected. In contrast, for the single receiver architecture, the employed antenna is not directed towards the transmitter to avoid the receiver saturation, and the direct-path signal is received by the antenna sidelobes. Therefore, the received signal will involve significant contributions from other transmitters operating in SFN mode and from static scatterers. Hence, an accurate propagation channel is required for the equalization of the frequency-domain symbols $\tilde{X}(i,k)$.

We adopt the channel estimation method proposed in chapter 5. The channel estimate ($\hat{\mathbf{H}}$) is firstly used to equalize the frequency-domain symbols $\tilde{X}(i,k)$ as follows

$$\check{X}(i,k) = \tilde{X}(i,k)/\hat{H}(k), \tag{6.5}$$

where $\check{X}(i,k)$ are the equalized symbol.

6.3.3 Reference signal recovery

The detection of the equalized symbols, $\check{X}(i,k)$, provides an estimation of the transmitted symbols which we note $\tilde{\mathbf{c}}$. An estimate of the direct-path signal can be retrieved by directly modulating the detected QAM symbols $\tilde{\mathbf{c}}$ (conventional reconstruction), or through the optimum reconstruction method presented in chapter 4. Since the direct-path signal is received by the antenna sidelobes, the expected DNR is likely to be low. As a result, the symbol detection error can be significant. Thus, we adopt the optimum reference signal reconstruction to retrieve an estimate of the direct-path signal, which extends the possibility of the reference signal extraction for low DNR levels.

The estimated signal is formed by the optimally weighted symbols $\hat{\mathbf{c}}$ which are calculated following the equation (4.43). The optimum filter weight for the data symbols is calculated according to the DNR value. We note $\hat{s}(n)$ the time-domain estimate of the transmitted signal, which is obtained by modulating the symbols $\hat{\mathbf{c}}$.

6.3.4 Static clutter suppression

The static clutter suppression is performed in the frequency domain by exploiting the estimates of transmitted symbols ($\hat{\mathbf{c}}$) and the propagation channel estimate $\hat{\mathbf{H}}$. As explained in chapter 5, the estimation of the static clutter can be obtained by multiplying the propagation channel estimate $\hat{\mathbf{H}}$ and the filtered symbols $\hat{\mathbf{c}}$. Then, a subtraction of the static clutter estimate from the symbols $\tilde{\mathbf{X}}$ leads to the clutter-free signal. Hence, we can write

$$X_{filtered}(i,k) = \tilde{X}(i,k) - \hat{H}(k)\hat{c}(i,k). \tag{6.6}$$

The time-domain filtered signal $x_{filtered}(n)$ is obtained by modulating the resulting symbols $\mathbf{X_{filtered}}$. Thus, the range-Doppler diagram is obtained by cross-correlating the synthetic reference signal $\hat{s}(n)$ and the filtered signal $x_{filtered}(n)$.

6.4 Performance evaluation: simulation results

In this section, we assess the performances of the proposed signal processing scheme by employing simulated data. In order to do so, three aspects will be evaluated: the static clutter suppression capability, the reference signal extraction efficiency, and the achieved detection probability. In the reminder of this chapter, we refer to the signal processing method that uses the conventional reference reconstruction [27, 51] and the static clutter suppression method proposed in [54] as the conventional method, which will be compared to the proposed signal processing scheme (optimum reference signal reconstruction and improved channel estimation).

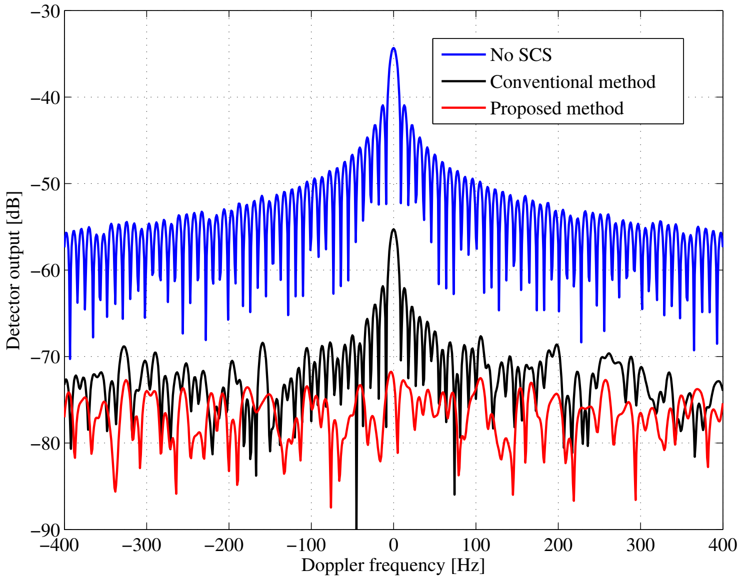

FIGURE 6.3: Cuts of the range-Doppler diagram at zero range for $N = 10^6$ and DNR = 20 dB.

Firstly, we compare the static clutter suppression capability of both methods. To do so, we consider the direct-path attenuation level as a metric [22]. Figure 6.3 presents cuts of the range-Doppler diagram at zero range for DNR = 20 dB and a coherent processing interval of length $N = 10^6$. We remark that the conventional method achieved a direct-path attenuation of about 20 dB, and that the proposed method achieved a full suppression of the direct-path signal. Clearly, the proposed method for static clutter suppression outperforms the conventional one due to the more accurate propagation channel estimation, which will permit the detection of low-magnitude slow-target echoes.

Secondly, we assess the efficiency of the reference signal extraction. Two aspects can be employed for this assessment: the coherent integration gain and the noise-floor level in the resulting range-Doppler diagrams [9]. Figure 6.4 shows a cut of the range-Doppler diagram at the target range for DNR = 20 dB and $N = 10^6$. The considered propagation channel includes many static scatterers and several transmitters in the SFN mode. The target echo is characterized by a Doppler shift of f_d = 200 Hz and a signal-to-noise ratio of SNR = −30 dB. For the noise-floor level, we notice that the proposed method provides a lower level compared to the conventional method. In addition, the proposed method achieves a better coherent integration gain. Actually, even for high DNR levels, the accuracy of the channel estimation affects the equalization of the received symbols $\tilde{\mathbf{X}}$, and thus influences the quality of the generated reference signal. Therefore, the reference signal acquired through the conventional channel estimation

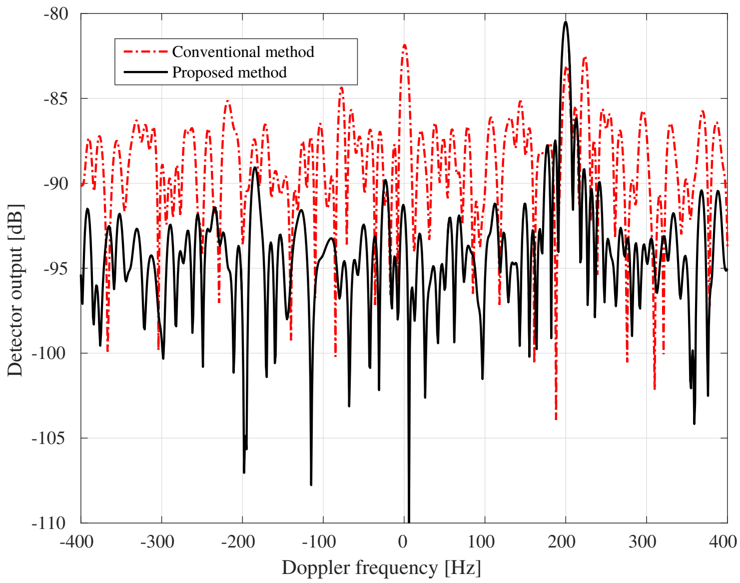

FIGURE 6.4: Cut of the range-Doppler diagram at the target range for $N = 10^6$, DNR = 20 dB, $f_d = 200$ Hz, and SNR $= -30$ dB.

will yield a higher noise-floor level and a deterioration of the coherent integration gain, which degrades the detection probability.

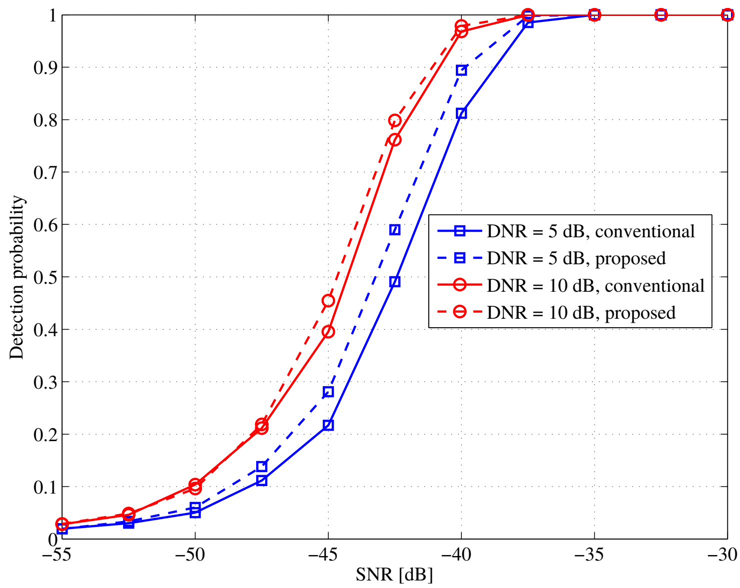

FIGURE 6.5: Monte-Carlo results for the detection probability for two DNR values with $N = 10^5$ and $\mathrm{P_{FA}} = 10^{-3}$.

To obtain a clearer understanding about the performance of the proposed method for signal processing, we calculate the detection probability as a function of DNR and SNR values. Figure 6.5 presents the detection probability values obtained by Monte-Carlo simulations as a function of the target signal-to-noise ratio (SNR) for two DNR values. The proposed method and the conventional one are compared. We set the false-alarm probability at $P_{FA} = 10^{-3}$ and the length of the coherent processing interval at $N = 10^5$. Firstly, we remark that the DNR level influences the detection probability since it controls the quality of the generated reference signal. Thus, a high DNR level yields a more accurate reference signal estimation, which improves the detection probability. Secondly, we remark that the proposed method outperforms the conventional method for both DNR values. However, for DNR = 10 dB, the advantage of the proposed method is reduced.

The superiority of the proposed method results from two factors: the accurate propagation channel estimation and the optimum reference signal reconstruction. The accurate channel estimation permits an accurate demodulation of the direct-path signal, and an efficient static clutter suppression. And the optimum reference signal reconstruction reduces the mismatch between the reconstructed signal and the exact one, which decreases the noise-floor level and thus increases the detection probability.

6.5 Performance evaluation: real-data

6.5.1 Measurement campaign set-up

The measurement campaigns were performed in Brussels at the Royal Military Academy (RMA). We considered the DVB-T transmitter located on the top of the Finance Tower (2.2 km from the receiver) as the illuminator of opportunity. The nearby Zaventem airport (BRU), located at 10 km from the receiver, provides the opportunity of having low-altitude targets during landing and taking off maneuvers. Table 6.1 summarizes the principle parameters of the measurement campaigns.

Carrier frequency	482 MHz
DVB-T mode	8k-mode
Guard interval (GI)	1/4
Transmitter radiated power	10 kW
Antenna gain	11 dBi
Transmitter-receiver distance	2.5 km
Coherent processing interval	0.1 s

Table 6.1: Parameters of the measurement campaigns.

Figure 6.6 presents the set-up employed for the measurement campaigns. It includes a Yagi antenna (MXR0012) originally dedicated to the domestic reception of the DVB-T, a USRP B100 device, and a computer running GNU radio. The recorded data are then processed with Matlab.

The antenna was vertically polarized since the exploited transmitter has a vertical polarization. In addition, the antenna main lobe is directed towards Zaventem airport, which maximizes the target echo magnitude (landing and taking off airplanes) and prevents the receiver saturation since the transmitter is located in the opposite direction.

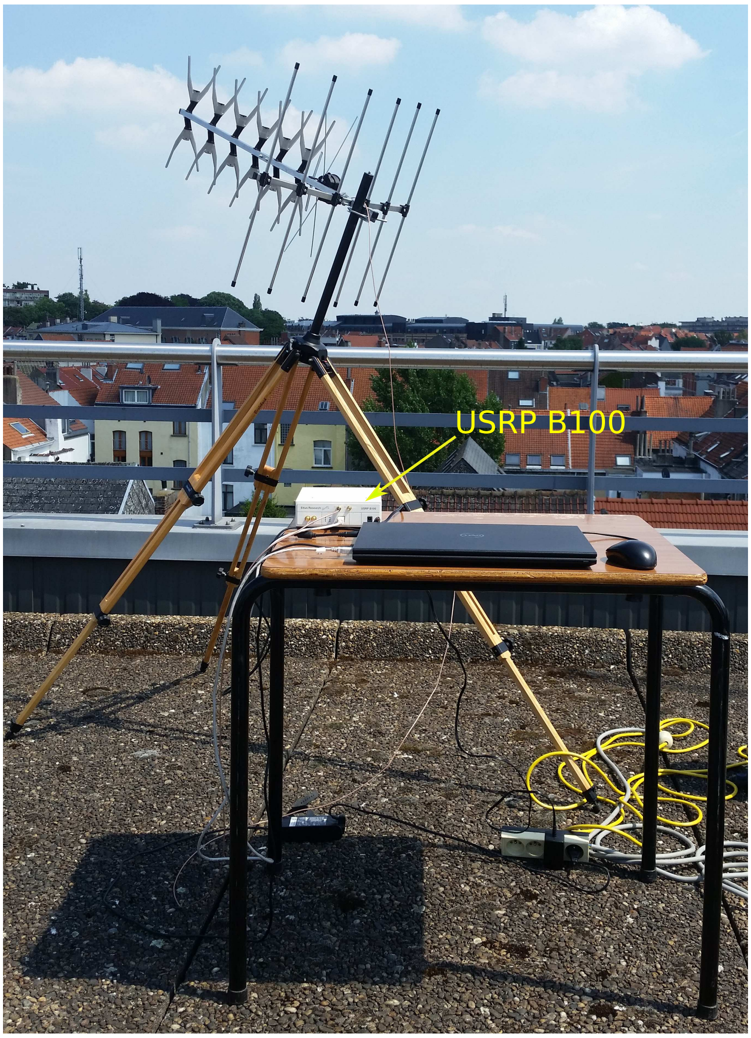

FIGURE 6.6: Measurement campaign set-up with a Yagi antenna and a USRP B100 board.

Figure 6.7 presents a USRP (Universal Software Radio Peripheral) B100 device. A sampling frequency of 8 MHz, and a resolution of 12 bits for the analog-to-digital converter (ADC) have been selected.

The software GNU radio supports the USRP technology, and enables many signal processing tasks for the design of the software defined radio applications. Figure 6.8 shows the employed blocks for storing the received signals. The first block corresponds to the parameters of the USRP device such as the sampling frequency, the bandwidth, and the gain. The second block precises the parameters of the stored data such as the ADC resolution (12 bits) and the saving path.

FIGURE 6.7: USRP B100.

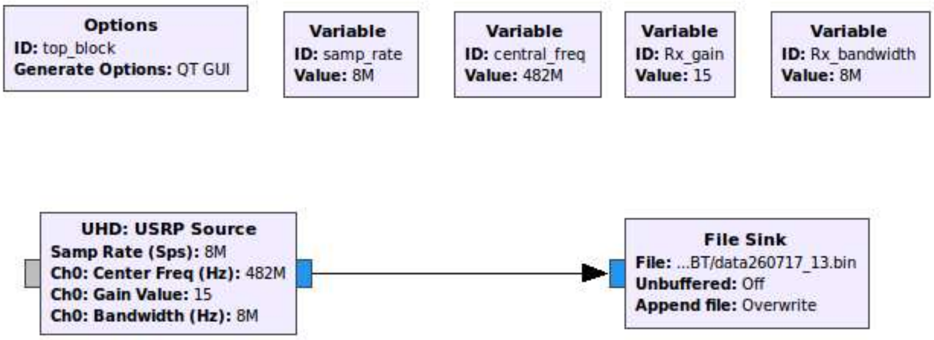

FIGURE 6.8: GnuRadio interface.

6.5.2 Automatic Dependent Surveillance-Broadcast

Automatic dependent surveillance-broadcast (ADS-B) is a surveillance and tracking technology where the aircraft regularly broadcasts its position, speed, heading angle, and other parameters. These information can be received by air traffic control stations and other aircrafts [126]. The most popular ADS-B data link standard is the 1090 MHz Extended Squitter (1090ES) [127]. The 1090ES employs a frequency of 1090 MHz for the transmission which starts with a preamble for synchronization followed by the data block with a pulse position modulation (PPM). The ADS-B technology enhances the air traffic surveillance by providing accurate information about the state of the aircrafts, which facilitates the air traffic management.

Besides air traffic control stations and aircrafts, a wide community is interested on ADS-B signals. The community members receive the ADS-B signals and share them to form a worldwide aircraft tracking databases. The ADS-B signal reception can be performed by inexpensive software-defined radio (SDR) devices and a free software for the signal decoding. Figure 6.9

FIGURE 6.9: RTL2832U dongle for DVB-T/DAB/FM signal reception.

presents an RTL2832U dongle for DVB-T/DAB/FM signal reception. This receiver has been widely used for SDR applications such as ADS-B signal reception and recording.

Hex	Flight	Altitude	Speed	Lat	Lon	Track	Messages	Seen .
4cab74		11775	371	0.000	0.000	59	8	4 sec
44cc94		11275	0	0.000	0.000	0	5	12 sec
44d078	TCW1CE	3025	163	50.876	4.416	183	77	0 sec
484b92	KLM57A	24000	393	50.663	3.677	196	114	19 sec
405a47		34625	575	0.000	0.000	112	29	0 sec
3430cc	VLG8635	35500	409	50.724	4.103	196	916	0 sec
4ca84a	RYR87W	7975	312	50.630	4.077	78	183	41 sec
505cb8	JAF7FM	27075	463	50.631	3.442	23	434	60 sec
4cc3ed	ABD704	32000	596	50.658	4.483	104	1924	0 sec
44f1a6		0	0	0.000	0.000	0	471	3 sec
400795		37000	0	0.000	0.000	0	2173	12 sec
44f142		0	0	0.000	0.000	0	441	0 sec

FIGURE 6.10: Decoding of the received ADS-B data.

Figure 6.10 presents the decoded ADS-B signal. The results involve the flight ID, the aircraft position (altitude, latitude, longitude), and its speed. The recorded data can be presented in the bistatic plane (bistatic range and bistatic Doppler shift) as presented in figure 6.11. To retrieve the bistatic coordinates, the transmitter and receiver positions are required. Having the exact position of the aircraft provides a ground truth information, which can be compared to the detected track to assess the radar performances or to execute a calibration if needed [6, 128–131].

6.5.3 Comparison results

Figures 6.12 and 6.13 present the sum of range-Doppler diagrams obtained from a recorded data set of 10 s duration. The received signal is divided into frames of 0.1 s duration, and the processing proposed in section 6.3 is applied on each frame. The resulting range-Doppler

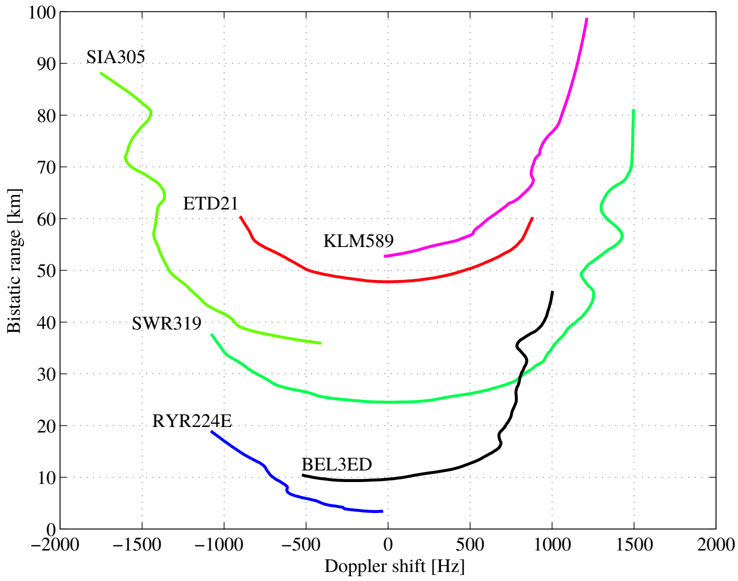

FIGURE 6.11: Recorded air traffic with ADS-B receiver presented in the bistatic plane.

diagrams are summed (in amplitude) to provide the full track of the airplane. The employed data involve echoes from an airplane during the taking off maneuver. Its bistatic range varies from 2 km to 4 km, and its Doppler shift evolves from 0 Hz to −350 Hz. The estimated level of the direct-path signal is about DNR = 18 dB; it follows that the optimum weight $(1 - \mathrm{P_e})$ tends to 1. Thus, the improvement due to the optimum reconstruction are insignificant for this data set. Therefore, the obtained results will emphasis only the impact of the propagation channel accuracy.

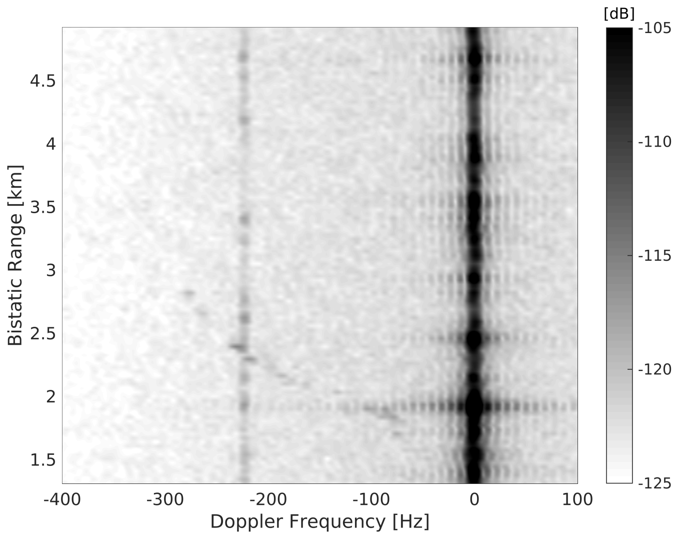

FIGURE 6.12: Real-data results for the conventional method applied in the single receiver architecture.

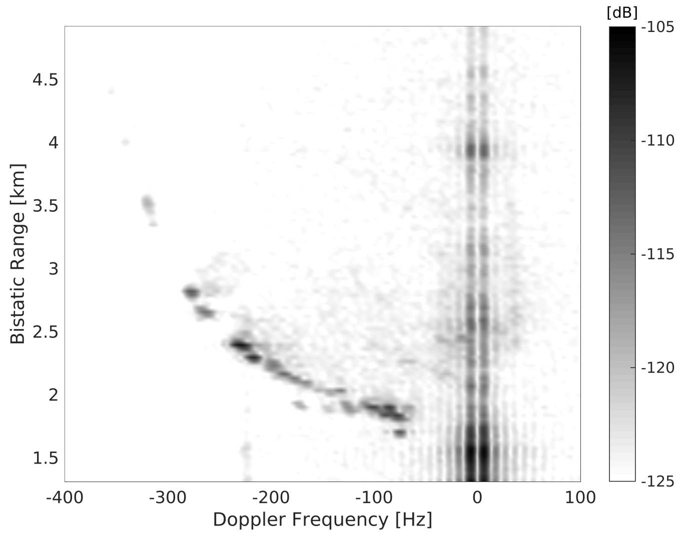

Figure 6.13: Real-data results for the proposed method applied in the single receiver architecture.

Figures 6.12 presents the results for the conventional method. We notice that the airplane track is not clear, the noise-floor level is relatively high, and the static clutter suppression is inefficient. The conventional channel estimation method provides a channel estimate affected by the interpolation errors, which from one side affects the QAM detection accuracy and thus the reference signal reconstruction, and from the other side fails to suppress the static clutter. The inaccuracy of reference signal estimation leads to a mismatch with the exact signal, which degrades the coherent processing gain and increases the noise-floor level.

For the results of the proposed method (figure 6.13), the airplane track is clear with a lower noise-floor level and a more efficient static clutter suppression than the conventional method. This illustrates the impact of the proposed channel estimation method that provides an accurate channel estimate, which allows a precise coded symbol detection and hence, an accurate reference signal estimation and an efficient static clutter suppression. In figure 6.12, the clutter around -220 Hz corresponds to ambiguities caused by the pilot signal patterns, which are suppressed by the static clutter removal in figure 6.13.

6.5.4 Performance results

6.5.4.1 Exploiting one DVB-T transmitter

Many measurement campaigns have been performed employing the set-up in figure 6.6. We exploited an approximate DVB-T transmitter located on top of the Finance Tower in Brussels (D = 2.2 km). The receiver was at the Royal Military Academy, and since the Brussels airport

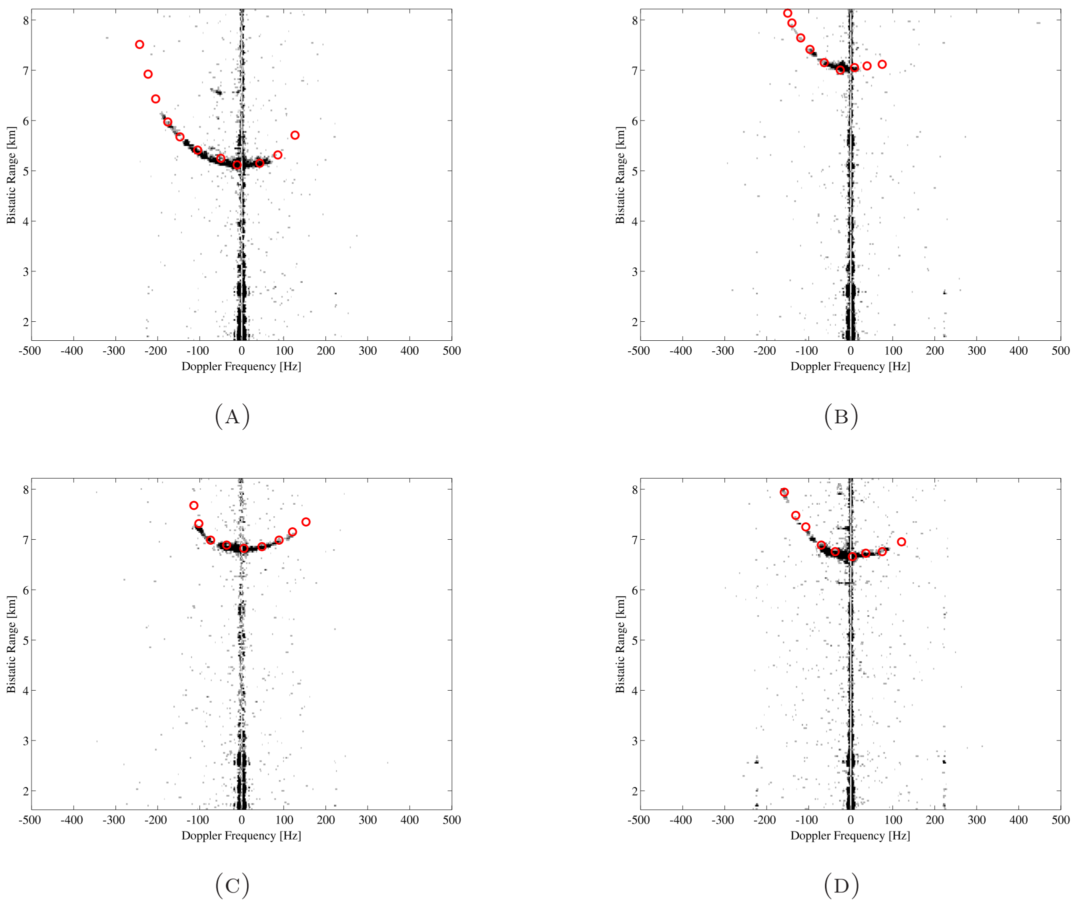

FIGURE 6.14: Range-Doppler diagrams for real-data sets with ADS-B validation (red circles).

is nearby, we could detect airplanes during the taking off maneuver. In parallel with DVB-T signal recording for radar detection, we recorded ADS-B data to form a ground truth for the results.

Figure 6.14 presents four airplane tracks. The tracks are obtained by summing the detection results along many data sets of length $T_{\mathrm{CPI}} = 0.1\ s$. In addition, the figures involve ADS-B data transformed to the bistatic plane. Firstly, we notice that the results by the radar detection match with those obtained via ADS-B data, which proves that the detected echoes correspond to the airplanes. Secondly, we remark that the static clutter is almost mitigated, which allowed the detection of the airplanes. Finally, we notice that all the detected tracks have the same path pattern which is due to the fixed orientation of the antenna.

6.5.4.2 Exploiting two DVB-T transmitters

Using the same set-up as in figure 6.6, we were able to detect airplanes exploiting two DVB-T transmitters: the transmitter at the Finance Tower (T_{x1}) and the one at Veltem (T_{x2}). The second transmitter is located at D = 16 km. Figure 6.15 presents two tracks for the same airplane seen by the two transmitters. ADS-B tracks are added to validate the detected tracks. The airplane echo illuminated by T_{x1} is at a bistatic range of $R_{b1} = 6$ km, and the resulting bistatic range from T_{x2} is $R_{b2} = 19$ km. The clutter at the bistatic range $R_b = 14$ km is due to the residual direct-path signal of T_{x2}.

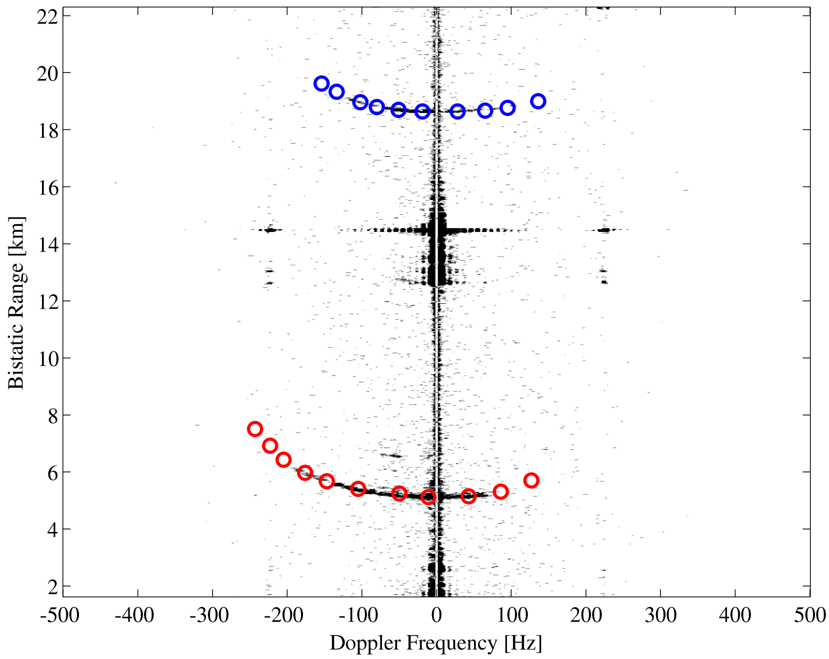

FIGURE 6.15: Detected airplane track according to two DVB-T transmitters with ADS-B validation: Finance Tower transmitter (red circles) and Veltem transmitter (blue circles).

As explained in chapter 2, the measured bistatic range defines an isorange contour. Figure 6.16 presents two isorange contours plotted considering the two bistatic ranges R_{b1} and R_{b2}. The intersections of the two isorange contours provide candidates for the exact coordinates of the airplane. In this figure, the exact position was known thanks to ADS-B data, otherwise, a third transmitter would be necessary to precisely locate the target. These results can be exploited for a study about multistatic PCL radars based on DVB-T signals.

6.6 Conclusion

In this chapter, we studied the feasibility of the single receiver based PCL radar employing DVB-T signals as an illumination source. This approach is made feasible due to the structure of the DVB-T signal. In the processing scheme, we have included the optimum reconstruction method from chapter 4, and the improved channel estimation from chapter 5; the results were

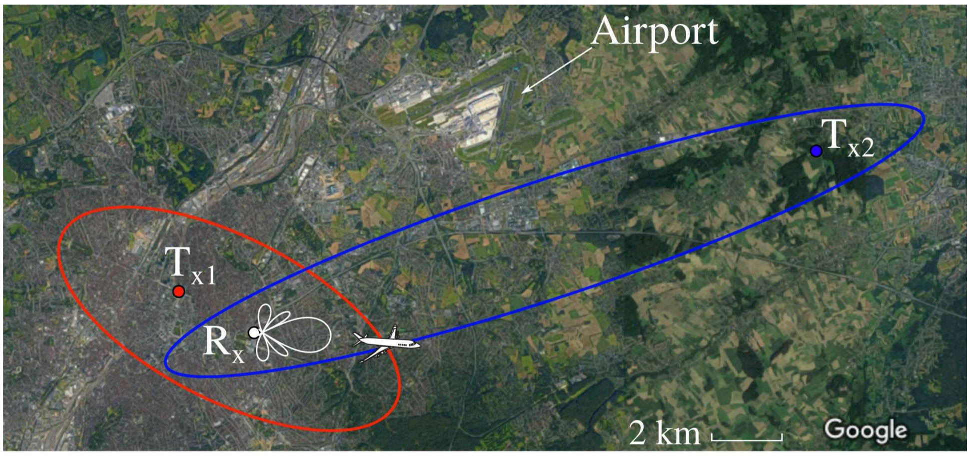

FIGURE 6.16: Two bistatic isorange contours based on two bistatic measurements with T_{x1} at the Finance Tower, T_{x2} at Veltem, and the receiver R_x at the RMA.

satisfactory. The improved channel estimation improves both the reference signal quality and the static clutter suppression.

This approach can significantly reduce the radar cost by involving a single receiver. An application example of the single receiver architecture can be a multiband PCL radar, where many transmitters of opportunity (with different frequencies) are employed to perform an accurate target localization. In this case, instead of employing two receivers per transmitter of opportunity, one receiver per transmitter (or per SFN) is sufficient.

Chapter 7

Conclusions and future work

7.1 Conclusions

The aim of this thesis has been the analysis and the improvement of the DVB-T PCL radar performance for a noisy reference signal and a surveillance signal involving static clutter. We assessed the impact of the reference signal noise on the detection probability, and we presented solutions to enhance its quality. In addition, we presented the effect of the static clutter and its removal techniques. And we verified the feasibility of a single receiver PCL radar based on DVB-T signals.

The noise in the reference signal increases the noise-floor level of the detection filter output, which degrades the detection probability. The possibility of demodulating the DVB-T signals is exploited to reconstruct the received reference signal. We assessed the conventional reconstruction method by analyzing the test statistics and calculating a closed-from expression for the detection probability. For an SNR that enables an accurate detection of the QAM symbols, the conventional reconstruction significantly improves the detection probability. However, for low SNR values, the QAM symbols are detected with an important error.

The reconstructed signal based on wrongly estimated symbols exhibits a mismatch with the exact one, which reduces the coherent processing gain and increases the noise-floor level of the detector. For low SNR values, we proposed to use a locally generated pilot signal for the detection. This method outperforms the conventional reconstruction when the symbol detection error is important. To reduce the reconstruction mismatch, we designed an optimum filter that minimizes the mean square error between the reconstructed signal and the exact one. The optimum reconstruction outperforms the conventional one, and it extends the feasibility of the signal reconstruction for low SNR values.

The presence of the static clutter in the surveillance signal reduces the detector dynamic range and masks low-Doppler echoes; thus, a static clutter suppression is required. We provided a review of the existing methods of static clutter suppression, and we evaluated their sensitivity to reference signal noise. In addition, we improved the efficiency of the filtering employing the propagation channel estimate. The resulting method is easy to implement, provides satisfactory results, and is less sensitive to the reference signal noise.

The feasibility of a single receiver PCL radar is verified. Both the proposed methods are included in the processing scheme, which noticeably increases the performances of this architecture. And by using real-data results, we illustrated the efficiency of the proposed methods compared to the conventional ones.

This thesis provides a deep understanding about the possibilities of exploiting the DVB-T signal structure to improve the resulting performances for PCL radars. This known structure has allowed the possibility of increasing the reference signal quality, and has permitted to efficiently suppress the static clutter from the surveillance signal.

7.2 Future work

7.2.1 Improving the proposed static clutter suppression method

The proposed method for the static clutter suppression operates in the frequency domain, and only the LS channel estimate has been employed. An improvement of the suppression can be retrieved by employing MMSE and SVD methods. The channel correlation matrix can be estimated using the channel estimate at pilot subcarriers obtained by the proposed method, which will improve MMSE and SVD methods. Another improvement can be achieved by designing a multistage version of the proposed method, which can suppress not only the zero-Doppler clutter but also low-Doppler clutter and strong target echoes.

7.2.2 Multistatic PCL radar

As previously stated, using one transmitter-receiver pair provides the bistatic range of the target, which defines an isorange contour. This result is insufficient to precisely locate the target. Thus, a multistatic architecture is required to obtain the target coordinates. The intersection of many isorange contours (obtained by exploiting different transmitter-receiver pairs) yields the target coordinates.

In chapter 6, we showed that it is possible to exploit two transmitters with a single receiver architecture. A similar set-up can be used to exploit two other transmitters operating in SFN mode with a frequency $f_T = 754$ Hz. The first one is located also at the Finance Tower and the second one at Wavre with D = 18 km. Consequently, Four transmitters will be exploited and thus the target coordinates can be determined.

7.2.3 Exploiting other illumination sources

As mentioned in chapter 1, many broadcasting sources can be exploited as illuminators of opportunity. Using several illumination sources will improve the PCL system performances by exploiting the advantages of each source. The DVB-T signals can be exploited for medium-range surveillance applications since the radiated power does not allow the detection of distant targets. However, FM signals can achieve a long-range detection due to the high radiated power. Therefore, a PCL radar that uses simultaneously DVB-T and FM signals can take advantage of the range-resolution of the DVB-T signals and the long coverage due to the FM signals.

Bibliography

[1] H. D. Griffiths and C. J. Baker, "Passive coherent location radar systems. Part 1: Performance prediction," *IEE Proceedings - Radar, Sonar and Navigation*, vol. 152, no. 3, p. 153, 2005.

[2] M. I. M. I. Skolnik, *Introduction to radar systems.* McGraw Hill, 2001.

[3] C. J. Baker, H. D. Griffiths, and I. Papoutsis, "Passive coherent location radar systems. Part 2: Waveform properties," *IEE Proceedings - Radar, Sonar and Navigation*, vol. 152, no. 3, p. 160, 2005.

[4] P. Howland, D. Maksimiuk, and G. Reitsma, "FM radio based bistatic radar," *IEE Proceedings - Radar, Sonar and Navigation*, vol. 152, no. 3, p. 107, 2005.

[5] C. Bongioanni, F. Colone, and P. Lombardo, "Performance analysis of a multi-frequency FM based Passive Bistatic Radar," in *2008 IEEE Radar Conference*, pp. 1–6, IEEE, may 2008.

[6] M. Malanowski, K. Kulpa, J. Kulpa, P. Samczynski, and J. Misiurewicz, "Analysis of detection range of FM-based passive radar," vol. 8, no. 2, pp. 153–159, 2014.

[7] M. Kubica, V. Kubica, X. Neyt, J. Raout, S. Roques, and M. Acheroy, "Optimum target detection using illuminators of opportunity," in *Radar, 2006 IEEE Conference on*, pp. 8 pp.–, 2006.

[8] X. Neyt, J. Raout, M. Kubica, V. Kubica, S. Roques, M. Acheroy, and J. G. Verly, "Feasibility of STAP for passive GSM-based radar," in *Radar, 2006 IEEE Conference on*, pp. 6 pp.–, 2006.

[9] D. W. O'Hagan, H. Kuschel, J. Heckenbach, M. Ummenhofer, and J. Schell, "Signal reconstruction as an effective means of detecting targets in a DAB-based PBR," in *11-th International Radar Symposium*, pp. 1–4, jun 2010.

[10] M. Daun, U. Nickel, and W. Koch, "Tracking in multistatic passive radar systems using DAB/DVB-T illumination," vol. 92, pp. 1365–1386, jun 2012.

[11] C. R. Berger, B. Demissie, J. Heckenbach, P. Willett, and S. Zhou, "Signal Processing for Passive Radar Using OFDM Waveforms," *Selected Topics in Signal Processing, IEEE Journal of*, vol. 4, no. 1, pp. 226–238, 2010.

[12] J. E. Palmer, H. A. Harms, S. J. Searle, and L. M. Davis, "DVB-T Passive Radar Signal Processing," *IEEE Transactions on Signal Processing*, vol. 61, pp. 2116–2126, apr 2013.

[13] H. D. Griffiths and C. J. Baker, "Measurement and analysis of ambiguity functions of passive radar transmissions," No. January, pp. 321–325, Institute of Electrical and Electronics Engineers Inc., 2005.

[14] J. Liu, H. Li, and B. Himed, "On the performance of the cross-correlation detector for passive radar applications." 2015.

[15] J. Baniak, G. Baker, A. Cunningham, and L. Martin, "Silent Sentry passive surveillance," *Aviation Week & Space Technology magazine*, 1999.

[16] S. Herman and P. Moulin, "A particle filtering approach to FM-band passive radar tracking and automatic target recognition," in *Proceedings, IEEE Aerospace Conference*, vol. 4, pp. 4–1789–4–1808, IEEE, 2002.

[17] H. Kuschel, "VHF/UHF radar. Part 1: Characteristics," *Electronics & Communication Engineering Journal*, vol. 14, pp. 61–72, apr 2002.

[18] G. Cui, J. Liu, H. Li, and B. Himed, "Target detection for passive radar with noisy reference channel," in *2014 IEEE Radar Conference*, pp. 144–148, 2014.

[19] G. Cui, J. Liu, H. Li, and B. Himed, "Signal detection with noisy reference for passive sensing," *Signal Processing*, vol. 108, pp. 389–399, 2015.

[20] M. K. Bączyk, K. Kulpa, P. Samczyński, and M. Malanowski, "The impact of reference channel SNR on targets detection by passive radars using DVB-T signals," in *2015 IEEE Radar Conference (RadarCon)*, pp. 708–712, 2015.

[21] R. Cardinali, F. Colone, P. Lombardo, O. Crognale, A. Cosmi, and A. Lauri, "Multipath cancellation on reference antenna for passive radar which exploits FM transmission," in *IET International Conference on Radar Systems 2007*, pp. 192–192, IEE, 2007.

[22] F. Colone, D. W. O'Hagan, P. Lombardo, and C. J. Baker, "A Multistage Processing Algorithm for Disturbance Removal and Target Detection in Passive Bistatic Radar," *IEEE Transactions on Aerospace and Electronic Systems*, vol. 45, pp. 698–722, apr 2009.

[23] R. Tao, H. Z. Wu, and T. Shan, "Direct-path suppression by spatial filtering in digital television terrestrial broadcasting-based passive radar," *IET Radar, Sonar Navigation*, vol. 4, no. 6, pp. 791–805, 2010.

[24] M. Radmard, F. Behnia, and M. Bastani, "Cross ambiguity function analysis of the '8k-mode' DVB-T for passive radar application," pp. 242–246, 2010.

[25] H. A. Harms, L. M. Davis, and J. Palmer, "Understanding the signal structure in DVB-T signals for passive radar detection," pp. 532–537, 2010.

[26] M. K. Baczyk and M. Malanowski, "Decoding and reconstruction of reference DVB-T signal in passive radar systems," in *Radar Symposium (IRS), 2010 11th International*, pp. 1–4, 2010.

[27] S. Searle, S. Howard, and J. Palmer, "Remodulation of DVB-T signals for use in Passive Bistatic Radar," in *Signals, Systems and Computers (ASILOMAR), 2010 Conference Record of the Forty Fourth Asilomar Conference on*, pp. 1112–1116, nov 2010.

[28] N. J. Willis, *Bistatic radar.* SciTech Pub, 2005.

[29] M. Cherniakov and D. V. Nezlin, *Bistatic radar : principles and practice.* John Wiley, 2007.

[30] N. J. Willis and H. H. Griffiths, *Advances in bistatic radar.* SciTech Pub, 2007.

[31] M. I. M. I. Skolnik, *Radar handbook.* McGraw-Hill, 2008.

[32] M. I. Skolnik, "An Analysis of Bistatic Radar," *IRE Transactions on Aeronautical and Navigational Electronics*, vol. ANE-8, pp. 19–27, mar 1961.

[33] D. K. Barton and S. A. S. A. Leonov, *Radar technology encyclopedia.* Artech House, 1997.

[34] E. Hanle, "Survey of bistatic and multistatic radar," *IEE Proceedings F Communications, Radar and Signal Processing*, vol. 133, no. 7, p. 587, 1986.

[35] H. Griffiths, "From a different perspective: principles, practice and potential of bistatic radar," in *2003 Proceedings of the International Conference on Radar (IEEE Cat. No.03EX695)*, pp. 1–7, IEEE, 2003.

[36] M. Jackson, "The geometry of bistatic radar systems," *IEE Proceedings F Communications, Radar and Signal Processing*, vol. 133, no. 7, p. 604, 1986.

[37] J. M. Christiansen and K. E. Olsen, "Range and Doppler walk in DVB-T based Passive Bistatic Radar," in *2010 IEEE Radar Conference*, pp. 620–626, IEEE, 2010.

[38] M. Cherniakov and A. Moccia, *Bistatic radar : emerging technology.* John Wiley & Sons, 2008.

[39] T. Tsao, M. Slamani, P. Varshney, D. Weiner, H. Schwarzlander, and S. Borek, "Ambiguity function for a bistatic radar," *IEEE Transactions on Aerospace and Electronic Systems*, vol. 33, pp. 1041–1051, jul 1997.

[40] P. M. Woodward, *Probability and information theory with applications to radar,.* Pergamon Press, 1964.

[41] D. Petri, C. Moscardini, M. Martorella, M. Conti, A. Capria, and F. Berizzi, "Performance analysis of the batches algorithm for Range-Doppler map formation in passive bistatic radar," vol. 2012, 2012.

[42] S. Stein, "Algorithms for ambiguity function processing," *IEEE Transactions on Acoustics, Speech, and Signal Processing*, vol. 29, pp. 588–599, jun 1981.

[43] H. D. Griffiths and N. R. W. Long, "Television-based bistatic radar," *Communications, Radar and Signal Processing, IEE Proceedings F*, vol. 133, no. 7, pp. 649–657, 1986.

[44] P. F. Howland, "Target tracking using television-based bistatic radar," *IEE Proceedings - Radar, Sonar and Navigation*, vol. 146, no. 3, p. 166, 1999.

[45] D. K. P. Tan, H. Sun, Y. Lu, M. Lesturgie, and H. L. Chan, "Passive radar using Global System for Mobile communication signal: Theory, implementation and measurements," vol. 152, pp. 116–123, jun 2005.

[46] I. Suberviola, I. Mayordomo, and J. Mendizabal, "Experimental results of air target detection with a GPS forward-scattering radar," vol. 9, no. 1, pp. 47–51, 2012.

[47] F. Liu, M. Antoniou, Z. Zeng, and M. Cherniakov, "Coherent Change Detection Using Passive GNSS-Based BSAR: Experimental Proof of Concept," *IEEE Transactions on Geoscience and Remote Sensing*, vol. 51, pp. 4544–4555, aug 2013.

[48] H. Guo, K. Woodbridge, and C. J. Baker, "Evaluation of WiFi beacon transmissions for wireless based passive radar," 2008.

[49] K. Chetty, G. E. Smith, and K. Woodbridge, "Through-the-Wall Sensing of Personnel Using Passive Bistatic WiFi Radar at Standoff Distances," *IEEE Transactions on Geoscience and Remote Sensing*, vol. 50, pp. 1218–1226, apr 2012.

[50] D. Pastina, F. Colone, T. Martelli, and P. Falcone, "Parasitic Exploitation of Wi-Fi Signals for Indoor Radar Surveillance," *IEEE Transactions on Vehicular Technology*, vol. 64, no. 4, pp. 1401–1415, 2015.

[51] M. Baczyk and M. Malanowski, "Reconstruction of the reference signal in DVB-T-based passive radar," *International Journal of Electronics and Telecommunications*, vol. 57, no. 1, pp. 43–48, 2011.

[52] O. Mahfoudia, F. Horlin, and X. Neyt, "Optimum reference signal reconstruction for DVB-T based passive radars," in *2017 IEEE Radar Conference (RadarConf)*, 2017.

[53] X. Wan, F. Cheng, Z. Gong, Z. Zhao, and Q. Shao, "Multipath clutter rejection for digital radio mondiale-based HF passive bistatic radar with OFDM waveform," *IET Radar, Sonar & Navigation*, vol. 6, pp. 867–872, dec 2012.

[54] G. Chabriel, J. Barrere, G. Gassier, and F. Briolle, "Passive Covert Radars using CP-OFDM signals. A new efficient method to extract targets echoes," in *2014 International Radar Conference*, pp. 1–6, IEEE, oct 2014.

[55] O. Mahfoudia, F. Horlin, and X. Neyt, "On the static clutter suppression for DVB-T based passive radars," in *32nd URSI General Assembly and Scientific Symposium*, (Montreal, Canada), 2017.

[56] R. van. Nee and R. Prasad, *OFDM wireless multimedia communications*. Artech House, 2000.

[57] J. R. Barry, E. A. Lee, D. G. Messerschmitt, and E. A. Lee, *Digital communication*. Springer, 2004.

[58] H. Schulze, C. Luders, and John Wiley & Sons., *Theory and applications of OFDM and CDMA : wideband wireless communications*. Wiley, 2005.

[59] Won Gi Jeon, Kyung Hi Chang, and Yong Soo Cho, "An equalization technique for orthogonal frequency-division multiplexing systems in time-variant multipath channels," *IEEE Transactions on Communications*, vol. 47, no. 1, pp. 27–32, 1999.

[60] S. Coleri, M. Ergen, A. Puri, and A. Bahai, "Channel estimation techniques based on pilot arrangement in OFDM systems," *IEEE Transactions on Broadcasting*, vol. 48, pp. 223–229, sep 2002.

[61] K. Fazel and S. Kaiser, *Multi-carrier and spread spectrum systems*. J. Wiley, 2003.

[62] P. Robertson and S. Kaiser, "The effects of Doppler spreads in OFDM(A) mobile radio systems," in *Gateway to 21st Century Communications Village. VTC 1999-Fall. IEEE VTS 50th Vehicular Technology Conference (Cat. No.99CH36324)*, pp. 329–333 vol.1, IEEE, 1999.

[63] EBU/ETSI JTC, "Digital Video Broadcasting (DVB);Framing structure, channel coding and modulation for digital terrestrial television," tech. rep., Stadard, 2004.

[64] Y. S. Cho, *MIMO-OFDM wireless communications with MATLAB*. IEEE Press, 2010.

[65] W. Fischer and W. Fischer, *Digital video and audio broadcasting technology : a practical engineering guide*. Springer, 2008.

[66] J. van de Beek, M. Sandell, and P. Borjesson, "ML estimation of time and frequency offset in OFDM systems," *IEEE Transactions on Signal Processing*, vol. 45, pp. 1800–1805, jul 1997.

[67] Dong-Kyu Kim, Sang-Hyun Do, Hyun-Kyu Lee, and Hyung-Jin Choi, "Performance evaluation of the frequency detectors for orthogonal frequency division multiplexing," *IEEE Transactions on Consumer Electronics*, vol. 43, no. 3, pp. 776–783, 1997.

[68] S. Fechtel, "OFDM carrier and sampling frequency synchronization and its performance on stationary and mobile channels," *IEEE Transactions on Consumer Electronics*, vol. 46, no. 3, pp. 438–441, 2000.

[69] M. Speth, S. Fechtel, G. Fock, and H. Meyr, "Optimum receiver design for OFDM-based broadband transmission .II. A case study," *IEEE Transactions on Communications*, vol. 49, pp. 571–578, apr 2001.

[70] Shiou-Hong Chen, Way-Hong He, Hou-Shin Chen, and Yumin Lee, "Mode detection, synchronization, and channel estimation for DVB-T OFDM receiver," in *GLOBECOM '03. IEEE Global Telecommunications Conference (IEEE Cat. No.03CH37489)*, vol. 5, pp. 2416–2420, IEEE, 2003.

[71] Peng Liu, Bing-bing Li, Zhao-yang Lu, and Feng-kui Gong, "A novel symbol synchronization scheme for OFDM," in *Proceedings. 2005 International Conference on Communications, Circuits and Systems, 2005.*, vol. 1, pp. 247–251, IEEE, 2005.

[72] Li Zou, "Detection of the guard interval length in OFDM systems," in *CCNC 2006. 2006 3rd IEEE Consumer Communications and Networking Conference, 2006.*, vol. 2, pp. 1048–1051, IEEE, 2006.

[73] A. Metref, D. Le Guennec, and J. Palicot, "Optimized Decision-Directed Carrier Recovery Loop for 16-QAM Constellations," in *IEEE GLOBECOM 2007-2007 IEEE Global Telecommunications Conference*, pp. 3112–3117, IEEE, nov 2007.

[74] Young-Hwan You, JoonBeom Kim, and Hyoung-Kyu Song, "Pilot-Assisted Fine Frequency Synchronization for OFDM-Based DVB Receivers," *IEEE Transactions on Broadcasting*, vol. 55, pp. 674–678, sep 2009.

[75] J.-J. van de Beek, O. Edfors, M. Sandell, S. Wilson, and P. Borjesson, "On channel estimation in OFDM systems," in *1995 IEEE 45th Vehicular Technology Conference. Countdown to the Wireless Twenty-First Century*, vol. 2, pp. 815–819, IEEE, 1995.

[76] M. H. Hsieh and C. H. Wei, "Channel estimation for OFDM systems based on comb-type pilot arrangement in frequency selective fading channels," vol. 44, no. 1, pp. 217–225, 1998.

[77] O. Edfors, M. Sandell, J. J. D. Van Beek, S. K. Wilson, and P. O. Börjesson, "OFDM channel estimation by singular value decomposition," vol. 46, no. 7, pp. 931–939, 1998.

[78] Y. Li, "Pilot-symbol-aided channel estimation for OFDM in wireless systems," vol. 49, pp. 1207–1215, jun 2000.

[79] M. Morelli and U. Mengali, "A comparison of pilot-aided channel estimation methods for OFDM systems," vol. 49, pp. 3065–3073, dec 2001.

[80] S. Biracree, R. Casas, and A. Youtz, "Time domain phase noise correction for OFDM signals," in *Conference Record of the Thirty-Sixth Asilomar Conference on Signals, Systems and Computers, 2002.*, vol. 2, pp. 1837–1841, IEEE, 2002.

[81] C. Heegard and S. B. Wicker, *Turbo Coding.* Springer US, 1999.

[82] H.-S. Chen, W. Gao, and D. G. Daut, "Spectrum Sensing for OFDM Systems Employing Pilot Tones and Application to DVB-T OFDM," in *2008 IEEE International Conference on Communications*, pp. 3421–3426, IEEE, 2008.

[83] D. Danev, E. Axell, and E. G. Larsson, "Spectrum sensing methods for detection of DVB-T signals in AWGN and fading channels," in *21st Annual IEEE International Symposium on Personal, Indoor and Mobile Radio Communications*, pp. 2721–2726, IEEE, sep 2010.

[84] A. Y. Gafer, S. Elsadig, and J. Varun, "Front-end signal to noise ratio estimation for DVBT fixed reception in flat-fading channel," in *Intelligent and Advanced Systems (ICIAS), 2012 4th International Conference on*, vol. 1, pp. 296–300, 2012.

[85] R. Saini and M. Cherniakov, "DTV signal ambiguity function analysis for radar application," *IEE Proceedings - Radar, Sonar and Navigation*, vol. 152, no. 3, p. 133, 2005.

[86] H. Ochiai and H. Imai, "On the distribution of the peak-to-average power ratio in OFDM signals," *IEEE Transactions on Communications*, vol. 49, no. 2, pp. 282–289, 2001.

[87] S. Shepherd, J. Orriss, and S. Barton, "Asymptotic limits in peak envelope power reduction by redundant coding in orthogonal frequency-division multiplex modulation," *IEEE Transactions on Communications*, vol. 46, no. 1, pp. 5–10, 1998.

[88] S. Wei, D. L. Goeckel, and P. A. Kelly, "Convergence of the Complex Envelope of Bandlimited OFDM Signals," *IEEE Transactions on Information Theory*, vol. 56, pp. 4893–4904, oct 2010.

[89] Z. Gao, R. Tao, Y. Ma, and T. Shao, "DVB-T Signal Cross-Ambiguity Functions Improvement for Passive Radar," in *2006 CIE International Conference on Radar*, pp. 1–4, IEEE, oct 2006.

[90] D. Langellotti, C. Bongioanni, F. Colone, and P. Lombardo, "Impact of synchronization on the ambiguity function shape for PBR based on DVB-T signals," pp. 60–63, 2010.

[91] R. Tao, Z. Gao, and Y. Wang, "Side Peaks Interference Suppression in DVB-T Based Passive Radar," *IEEE Transactions on Aerospace and Electronic Systems*, vol. 48, pp. 3610–3619, oct 2012.

[92] F. Colone, D. Langellotti, and P. Lombardo, "DVB-T signal ambiguity function control for passive radars," vol. 50, no. 1, pp. 329–347, 2014.

[93] G. Turin, "An introduction to matched filters," *IEEE Transactions on Information Theory*, vol. 6, pp. 311–329, jun 1960.

[94] F. Colone, R. Cardinali, P. Lombardo, O. Crognale, A. Cosmi, A. Lauri, and T. Bucciarelli, "Spacetime constant modulus algorithm for multipath removal on the reference signal exploited by passive bistatic radar," *IET Radar, Sonar & Navigation*, vol. 3, no. 3, p. 253, 2009.

[95] L. Jichuan, Z. Yaodong, Z. Yongke, and L. Xiaode, "Direct path wave purification for passive radar with normalized least mean square algorithm," in *2013 IEEE International Conference on Signal Processing, Communication and Computing (ICSPCC 2013)*, pp. 1–4, IEEE, aug 2013.

[96] J. Liu, H. Li, and B. Himed, "Two Target Detection Algorithms for Passive Multistatic Radar," *IEEE Transactions on Signal Processing*, vol. 62, pp. 5930–5939, nov 2014.

[97] J. Liu, H. Li, and B. Himed, "Analysis of cross-correlation detector for passive radar applications," in *Radar Conference (RadarCon), 2015 IEEE*, pp. 772–776, 2015.

[98] J. Palmer, S. Palumbo, T.-T. Cao, and S. Howard, "A New Illuminator of Opportunity Bistatic Radar Research Project at DSTO," tech. rep., EWRD/DSTO, 2009.

[99] K. E. Olsen and K. Woodbridge, "Performance of a multiband passive bistatic radar processing scheme Part I," *IEEE Aerospace and Electronic Systems Magazine*, vol. 27, pp. 16–25, oct 2012.

[100] A. Nuttall, "Some integrals involving the Q function," *IEEE Transactions on Information Theory*, vol. 21, pp. 95–96, jan 1975.

[101] Wan Xianrong, W. Junfang, Hong Sheng, and Tang Hui, "Reconstruction of reference signal for DTMB-based passive radar systems," in *Proceedings of 2011 IEEE CIE International Conference on Radar*, pp. 165–168, IEEE, oct 2011.

[102] J. A. Rice, *Mathematical statistics and data analysis.* Thomson/Brooks/Cole, 2007.

[103] S. Haykin, *Adaptive Filter Theory (3rd Ed.).* Upper Saddle River, NJ, USA: Prentice-Hall, Inc., 1996.

[104] R. Saini, M. Cherniakov, and V. Lenive, "Direct path interference suppression in bistatic system: DTV based radar," in *2003 Proceedings of the International Conference on Radar (IEEE Cat. No.03EX695)*, pp. 309–314, IEEE, 2003.

[105] E. Cristofani, V. Kubica, and X. Neyt, "A multibeam opportunistic SAR system," in *2011 IEEE RadarCon (RADAR)*, pp. 778–783, IEEE, may 2011.

[106] J. D. Sahr and F. D. Lind, "The Manastash Ridge radar: A passive bistatic radar for upper atmospheric radio science," *Radio Science*, vol. 32, pp. 2345–2358, nov 1997.

[107] K. Wang, R. Tao, Y. Ma, and T. Shan, "Adaptive Multipath Cancellation Algorithm in Passive Radar," in *2006 CIE International Conference on Radar*, pp. 1–4, IEEE, oct 2006.

[108] K. Kulpa and Z. Czekała, "Masking effect and its removal in PCL radar," *IEE Proceedings - Radar, Sonar and Navigation*, vol. 152, no. 3, p. 174, 2005.

[109] J. E. Palmer and S. J. Searle, "Evaluation of adaptive filter algorithms for clutter cancellation in Passive Bistatic Radar," in *2012 IEEE Radar Conference*, pp. 0493–0498, IEEE, may 2012.

[110] K. Kulpa, "The CLEAN type algorithms for radar signal processing," in *2008 Microwaves, Radar and Remote Sensing Symposium*, pp. 152–157, IEEE, sep 2008.

[111] H. A. Harms, J. E. Palmer, S. J. Searle, and L. M. Davis, "Impact of quantization on passive radar target detection," in *IET International Conference on Radar Systems (Radar 2012)*, pp. 1–6, oct 2012.

[112] J. Palmer, D. Cristallini, and H. Kuschel, "Opportunities and current drivers for passive radar research," in *2015 IEEE Radar Conference*, pp. 145–150, IEEE, oct 2015.

[113] F. Colone, R. Cardinali, and P. Lombardo, "Cancellation of Clutter and Multipath in Passive Radar using a Sequential Approach," in *2006 IEEE Conference on Radar*, pp. 393–399, IEEE, 2006.

[114] B. Widrow and S. D. Stearns, *Adaptive signal processing.* Prentice-Hall, 1985.

[115] Z. Jiabing, T. Liang, and H. Yi, "A Direct Path Interference Cancellation Approach to Passive Radar Based on FM Radio transmitter," in *2006 IEEE International Conference on Electro/Information Technology*, pp. 55–59, IEEE, may 2006.

[116] W. Miao, S. Tao, and Z. Zhihai, "An Adaptive Filter with Discrete Distribution Structure in DTV Based Passive Radar," in *2011 First International Conference on Instrumentation, Measurement, Computer, Communication and Control*, pp. 755–758, IEEE, oct 2011.

[117] M. Meller and S. Tujaka, "Processing of Noise Radar Waveforms using Block Least Mean Squares Algorithm," *IEEE Transactions on Aerospace and Electronic Systems*, vol. 48, pp. 749–761, jan 2012.

[118] M. Xiang, X. Lu, Y. Zhao, and Y. Zhao, "Block NLMS cancellation algorithm and its real-time implementation for passive radar," in *IET International Radar Conference 2013*, pp. 0431–0431, Institution of Engineering and Technology, 2013.

[119] M. Moddares-Hashemi, S. Sadri, and M. Masjedi, "Theoretical approach for target detection and interference cancellation in passive radars," *IET Radar, Sonar & Navigation*, vol. 7, pp. 205–216, mar 2013.

[120] C. Schwark and D. Cristallini, "Advanced multipath clutter cancellation in OFDM-based passive radar systems," in *2016 IEEE Radar Conference (RadarConf)*, pp. 1–4, IEEE, may 2016.

[121] J. Chen, X. Zhang, J. Li, and H. Gu, "Ground clutter suppression using noise radar with dual-frequency transmitter," in *2012 IEEE International Conference on Information Science and Technology*, pp. 873–877, IEEE, mar 2012.

[122] A. Guner, M. Temple, and R. Claypoole, "Direct-path filtering of DAB waveform from PCL receiver target channel," *Electronics Letters*, vol. 39, no. 1, p. 118, 2003.

[123] O. Mahfoudia and X. Neyt, "A DVB-T based passive radar using one USRP board," in *URSI Benelux Forum*, (Louvain-la-Neuve, Belgium), 2014.

[124] W. C. Barott and J. Engle, "Single-antenna ATSC passive radar observations with remodulation and keystone formatting," in *2014 IEEE Radar Conference*, pp. 0159–0163, IEEE, may 2014.

[125] S. Searle, L. Davis, and J. Palmer, "Signal processing considerations for passive radar with a single receiver," in *2015 IEEE International Conference on Acoustics, Speech and Signal Processing (ICASSP)*, pp. 5560–5564, IEEE, apr 2015.

[126] W. W. Chung and R. Staab, “A 1090 extended squitter Automatic Dependent Surveillance - Broadcast (ADS-B) reception model for air-traffic-management simulations,” vol. 2, pp. 757–767, 2006.

[127] M. Strohmeier, V. Lenders, and I. Martinovic, “On the Security of the Automatic Dependent Surveillance-Broadcast Protocol,” *IEEE Communications Surveys & Tutorials*, vol. 17, no. 2, pp. 1066–1087, 2015.

[128] A. Schroeder and M. Edrich, “CASSIDIAN multiband mobile passive radar system,” pp. 286–291, 2011.

[129] F. Belfiori, S. Monni, W. Van Rossum, and P. Hoogeboom, “Antenna array characterisation and signal processing for an FM radio-based passive coherent location radar system,” vol. 6, pp. 687–696, oct 2012.

[130] M. Malanowski, K. Kulpa, P. Samczynski, J. Misiurewicz, J. Kulpa, P. Roszkowski, P. Dzwonkowski, D. Gromek, L. Maslikowski, M. Misiurewicz, and L. Podkalicki, “Experimental results of the PaRaDe passive radar field trials,” in *2012 13th International Radar Symposium*, pp. 65–68, IEEE, may 2012.

[131] V. Winkler, M. Edrich, and A. Schroeder, “Design and performance evaluation of a FM /DAB / DVB-T multi-illuminator passive radar system,” in *IET International Conference on Radar Systems (Radar 2012)*, pp. 11–11, Institution of Engineering and Technology, 2012.